Experimental work related to tsunami research, conducted in 2D small scale and 3D large scale facilities

Erika Kristina Lindstrøm

Thesis submitted for the degree of Ph.D.

Department of Mathematics
University of Oslo

September 2014

Series of dissertations submitted to the
Faculty of Mathematics and Natural Sciences, University of Oslo
No. 1579

ISSN 1501-7710

Cover: Hanne Baadsgaard Utigard.
Printed in Norway: AIT Oslo AS.

Produced in co-operation with Akademika Publishing.
The thesis is produced by Akademika Publishing merely in connection with the thesis defence. Kindly direct all inquiries regarding the thesis to the copyright holder or the unit which grants the doctorate.

”You’ve got to know when to hold ’em
Know when to fold ’em
Know when to walk away
And know when to run
You never count your money
When you’re sittin’ at the table
There’ll be time enough for countin’
When the dealin’s done”
Kenny Rogers

Preface

This thesis is submitted in the partial fulfillment of the requirements for the degree of Doctor of Philosophy at the University of Oslo. It represents work that has been carried out in the period 2011-2014, under the supervision of Professors Geir K. Pedersen and Atle Jensen. Most of the work presented here was carried out at the University of Oslo, part of the work was also conducted at the Coast and Harbor Laboratory, SINTEF, Trondheim. Financial support for the work was provided by the Norwegian Council Grant NFR 205184/F20.

The thesis consists of two papers and one report in addition to the introduction. The introduction motivates and describe the methods I have used in my work, while the different parts are introduced chronologically according to when the experiments were performed. The common feature among the different parts that constitute this thesis is that it is related to tsunami research, and are based on experimental work.

Oslo, September 2014
Erika K. Lindstrøm

Acknowledgments

First of all, I would like to thank my main supervisor Professor and Cannon Commander Geir K. Pedersen. I would lie if I say that it has been a pleasure all the time and I am quite sure that it counts for both of us (like the time I was infected with lice without knowing it and we shared the same helmet in Trondheim). Anyway, Professor Pedersen has an impressive knowledge within fluid mechanics (and mushrooms, mammals, history, literature, baking, fruit, wasps, beer...) and he has patiently guided me through out my work. In addition to wisdom, he has a great sense of humor which has made my work much easier to handle. Next, I would like to thank my second supervisor Professor Atle Jensen, who has been involved in my experimental work and given me guidance whenever I needed. He had the ability to get me recharged and back on track when I got fed up with work, and I am really thankful for that. He also did a great act as "the Bad guy" when kind words and friendliness was not enough, brilliant work. In addition, Atle introduced me to the wonderful game of table football. I once said that I would not leave Blindern until I won a game against Atle. Well, I need to start believe in miracles, he is still the unbeaten master of the game. Professor Pedersen and Professor Jensen have been a killer combination and I could not have asked for better supervisors. I have also had the pleasure of getting free beer due to poorly placed bets, and as all of us know, those beers are the best. I have also had the pleasure to work with Head Engineer Olav Gundersen in the hydrodynamic laboratory and I am grateful for his contribution. He also helped me practicing my table football skills, without him Anis would probably never have had a mustache.

I have had a great time at Blindern, not only because I love science, but also due to my great colleagues. I would like to thank each and every one of you for fruitful discussions, laughter, cake, beer, apple party, gingerbread house constructing and table football. Specials thanks go to Jostein Kolaas and Anis Awal Ayati, who I have been working with throughout the years both in courses and laboratory work. The first time I met Jostein he was giggling while I was messing up a derivation on the black board. I firstly got a bit offended but decided to find out what was going on with this guy. He turned out to be one of the friendliest people I have ever met, and in addition has great sense of humor. Anis is one of the youngest old men I know. He possess the wisdom of life and always keep calm whatever is going on around him (like pipes breaking, flooding the lab during a presentation, Anis just kept talking while me and Atle tried to save computers and turn off the water). We have had a lot of deep conversations about life and he has truly earned the title *Doctor philosophiae*.

I also need to express my gratitude to my friends and family who has been supported me during my years at Blindern, even during my periods acting like an anti-social outcast. A special thanks go to my three close friends Trine Jelstad Olsen, Svein Vesterby and Farah Rashid. The first time I met Trine, I got a bit pissed off because she was simply too perfect, luckily, that

was not true. Trine is a great friend in all means and truly has a passion for life. She has been supporting me and cheering me on no matter what, and when necessary, told me to *Veta Hut*. Svein Vesterby has meant the world to me during my years at Blindern, and I have really enjoyed our fancy lunches at Frida. Farah and her wonderful girls have shown me that absolutely anything is possible as long as you work hard.

I would like to thank my mother Ritha and father Jan Erik for teaching me that giving up is not an option. My father passed away 9 years ago and I am very sorry that he could not be a part of this journey. I also would like to thank my grandmother Hildur, who I miss every day.

Finally, and most importantly I would like to thank my family. I could not have done this without my husband Joakim Berglund, who has been unconditionally loving and supportive during my years at Blindern. You are my hero and best friend, without you there would be no Dr. E. K. Lindstrøm. My wonderful children Maja and Noah who everyday reminded me what is really important in life, and the sound of their laughter always gets me into a good mood, I will never be able to fully describe how much you mean to me.

Contents

Introduction

Tsunamis are classified as long waves in shallow water, traveling with a speed dependent on the water depth. They are caused by the displacement of a large volume of water due to an impulsive disturbance, such as earthquakes, submarine and subaerial slides, volcanic eruptions and asteroid impacts. Tsunamis generated by earthquakes may have wavelengths of several hundreds of kilometers, small deep-water amplitudes and travel with velocities typically ranging from 500 to 1000 km/h (e.g. Geist *et al.* (2006)). When the waves reach the shore, the velocity decreases, which leads to an amplification in elevation with possible devastating consequences. Tsunamis generated by landslides has not been given as much attention and is less known. Slide generated waves affects typically smaller regions (Okal & Synolakis, 2004). But, the initial wave heights may be huge with runup heights up to several hundreds of meters (Fritz *et al.*, 2009).

Tsunami hazards have become more significant due to the increased population in coastal zones. The Indian Ocean tsunami in 2004 and the Great East Japan tsunami in 2011 are two disasters which caused devastating destruction. In order to prevent casualties and destruction, appropriate knowledge about generation, propagation and inundation of tsunamis are vital. Due to the complexity of the wave evolution, from generation to runup, a number of different approaches are necessary including numerical modeling, experiments in small and large scale, field surveys and analytic theory. Numerical models are traditionally based on long wave equations, including dispersion and nonlinearity when necessary. The developed numerical models are often validated by analytic theory, experiments and/or field observations. Experiments are performed in a controlled environment and a number of different aspects of the flow may be measured, on the other hand, laboratory investigations may include scale effects. Field observations of the inundation are generally based on either recognition of watermarks on land and vegetation or through personal reports from eyewitnesses and collected information from a real event is very valuable. However, one should be aware of the limitations of experiments or field observations. In this study it is crucial to have particulars about the limitations of the applied models and keep in mind that sometimes good agreement may be coincidental.

Tsunami society, a historical perspective

There exist an extensive amount of literature concerning tsunami research. In this section a brief review of some of this literature is presented.

Due to the complexity of generation and evolution in combination with a lack of instrumental recordings, analytic and numerical work for prediction of propagation and runup was previously somewhat limited. One example of early work related to tsunami research is Hall

& Watts (1953) who studied a solitary wave approaching an inclined beach, where the experiments represented waves propagating over a flat ocean and then climbing up a uniformly sloping continental shelf. Wiegel (1955) did experiments on slide generated waves, where the slide was represented as a wedge shaped box. Carrier & Greenspan (1958) derived a non linear solution based on monochromatic waves approaching from infinity, with runup on an inclined beach. In 1966 Peregrine (1966) calculated the evolution of a undular bore propagating over constant depth, continuing with deriving different approximations of depth averaged equations in 1967 (Peregrine, 1967). During the 80s, numerical models for calculating runup developed rapidly. Gopalakrishnan & Tung (1980) studied run-up of non-breaking waves and applied numerical models where the Galerkin finite element method were used to produce a quasi 2-D model. Synolakis (1987) reported experiments on breaking and non-breaking solitary waves running up a beach compared with theory. He obtained a celebrated asymptotic solution for the runup height. The real break through for tsunami science was during the 90s, when large scale experimental data became available together with a range of field surveys. In September 1992, the Nicaraguan tsunami was the first major tsunami in 9 years, followed by the Flores Island tsunami in December 1992, which resulted in a number of detailed studies also in three dimensions (Synolakis & Bernard, 2006).

Two major disasters caused by earthquakes in subduction zones are the 2004 Indian Ocean tsunami and the 2011 Great East Japan tsunami. The 2004 tsunami caused over 220 000 casualties and is the most devastating tsunami in recorded history (Lay *et al.*, 2005). A number of field surveys were done with the objective to improve and further develop numerical models for prediction of inundation (Synolakis & Kong, 2006). The 2011 tsunami caused more than 15 000 deaths with local inundation up to $5\,\mathrm{km}$ (Romano *et al.*, 2012). A large data set for this tsunami is available, including altimeters, pressure gauges, inundation heights and tide gauges data. Hooper *et al.* (2013) applied this data to model the seafloor motion while Suppasri *et al.* (2013) evaluated the damage level on buildings caused by the tsunami. In the awareness of possible devastating natural distastes caused by earthquake generated tsunamis, numerous works on tsunami hazards has been reported (Geist & Parsons, 2006; Løvholt *et al.*, 2012, 2014).

Due to the two major distastes in 2004 and 2011 a lot of attention has been given to earthquake generated tsunamis. Tsunamis that are generated by landslides constitutes a great threat but affects smaller regions. In 1958 a rock-slide was triggered by an earthquake in Lituya Bay, the generated wave over-topped the facing hillside with a runup height of 524 m. This event has been investigated both experimental and numerically with good agreement to the real case (Mader, 1999; Fritz *et al.*, 2001, 2009). A more recent slide generated tsunami is the Papua New Guinea tsunami in 1998 which flooded three villages and caused over 2200 deaths (Tappin *et al.*, 2008). A study of submarine landslide generated tsunamis were conducted by Harbitz *et al.* (2014*a*), who summed up historical global events and discussed the assessment of present slide tsunami hazard in relation to earlier events.

Tsunami research at the Department for Mathematics and Norwegian Geotechnical Institute, Oslo

The University of Oslo and The Norwegian Geotechnical Institute have a lasting and close collaboration on tsunami research, including joint projects and participation in a center of excellence (ICG). Currently there is a joint tsunami research group in Oslo with a history of more than 30 years. Its activity has included theory, numerical modeling, case studies as well as industry and academic projects.

An important topic of tsunami related research is validation of numerical models, which are crucial in order to predict generation and inundation of tsunamis. Validation are often based on relatively small scale experiments which may include scale effects. These scale effects may not be captured properly in the models, with the risk of a validation less reliable. Great attention has been given to studies concerning runup on beaches. Pedersen & Gjevik (1983) studied runup of long waves where they applied numerical models based on a set of Boussinesq equations. They compared their results with experiments and introduced a formula for maximum runup height, dependent on the amplitude of the wave and inclination of the beach. Pedersen and Gjevik suggested that the scale effects decreased with increasing water depth and beach angle. Jensen *et al.* (2003) revisited the runup of solitary waves experimentally, with new measuring techniques and main focus on velocity fields in the flow. They compared their experimental data with a Boussinesq model and discussed scale dependency. The experimental data provided by Jensen *et al.* (2003) were revisited by Wood *et al.* (2002) who employed a Navier Stokes model in order to capture the properties of the flow. The Navier Stokes solver were able to capture properties of the flow even for the largest generated wave, where the Boussinesq solver failed. Sælevik *et al.* (2013) increased the complexity of the runup by applying a beach which had a change in inclination from 10 degrees to 4 degrees at a vertex point located at 0.4 depths above equilibrium water level in addition to a straight beach. Runup on composite beach yielded thinner swash tongues above the vertex point compared to the straight beach. While working with this, Sælevik *et al.* (2013) found that deviation from inviscid theory were more pronounced for the thinner swash tongues and suggested that the discrepancies between theory and experiments was the result of scale effects. The works mentioned above all discuss the appearance of scale effects, which were not captured in the applied models.

Another aspect of tsunami research at the University of Oslo is waves generated by earthquakes or land slides. Storegga slides were huge prehistoric submarine landslides on the Norwegian continental slope. Deposits of inundation have been found in Norway, Scotland and the Shetland Islands. Harbitz (1992) compared the Storegga slide deposits with numerical computations and reported good agreement. Harbitz *et al.* (1993) did simulations on landslide generated waves, a numerical model based on the hydrodynamic shallow water equations were applied. They discussed their results in relation to a historic event in a Norwegian fjord, the Tafjord catastrophe in 1934 where 40 people perished. Glimsdal *et al.* (2013) investigated the effect of dispersion in tsunami modeling, and evaluated both historical and potential tsunami events, earthquake and slide generated. At La Palma, Canary Island, a flank collapse of the Cumbre Vieja volcano during a future eruption is a possible scenario. Ward & Day (2001) did numerical simulations of this future threat and found that the waves would have devastating consequences not only for the closest locations but also for the east coast of USA. The La Palma case were

revisited by Løvholt *et al.* (2008), were they combined multimaterial model for the wave generation and Boussinesq model for the far field propagation. They concluded that the hydrostatic models fail to describe the far field due to the complexity of the wave propagation including dispersion, refraction and interference in the direction of propagation. Later on Løvholt *et al.* (2013) considered Boussinesq models in fjords, and found instabilities for highly nonlinear waves in steep slope geometries. They suggested coupling of Navier-Stokes or Eulerian based models for the near field to a Boussinesq model for the far field. Example of such coupling is given in Løvholt *et al.* (2008), where they applied one-way coupling. Suggestions from Løvholt *et al.* (2013) is that two-way coupling should be applied for future models.

An unstable slope is detected in Åkneset located in Storfjorden, Western Norway, the slope is shown in figure 1. This slope has been surveyed and extensively monitored for the last decade (Norem *et al.*, 2007). A slide with a volume up to 54 million cubic meters will be released some time in the future (Harbitz *et al.*, 2014*b*). In relation to this future threat, a close cooperation between the University of Oslo (UiO), Norwegian Geotechnical Institute (NGI) and the Coast and Harbor Research Laboratory (CHL) started in order to increase understanding and develop improved computational tools for tsunamis generated by rock slide. Sælevik *et al.* (2009) did a two dimensional experimental investigation of different scenarios for the Åkneset case. The two dimensional case revealed waves corresponding to $70 - 100\,\mathrm{m}$ in full scale, but due to the three dimensional fjord geometry and distribution of wave energy, these figures cannot be applied to the real Åkneset case. In 2008 a 1:500 scale three dimensional model of the inner part of Storfjorden was built at CHL. First set of experiments were conducted in 2008, were the slide represented the worst case scenario. The measurements were restricted to surface elevation measurements at 12 locations in the fjord model, particle velocity measurements at three locations and runup measured by by two level sensors located in the two populated villages Hellesylt and Geiranger. Experimental setup of the 2008 experiments are presented in NGI (2011), together with experimental results and comparison with numerical models. Harbitz *et al.* (2014*b*) employed the experimental results as input and validation of numerical models in his work on rockslide tsunamis in complex fjords.

Experiments of waves in small and large scales

As discussed in previous sections, tsunami research is comprehensive work. The focus of this thesis is experimental studies, concerning both detailed evaluations of runup of solitary waves on a sloping beach in small scale and blockslide generated waves in a complex fjord model in large scale.

Experiments performed in a two dimensional wavetank, small scale

Small scale experiments were conducted at the Hydrodynamic laboratory, University of Oslo, which provides facilities for physical, coastal and ocean research. The facilities includes two pipelines, 5 and $10\,\mathrm{cm}$ in diameter and two water wave tanks with dimensions $25\,\mathrm{m} \times 1\,\mathrm{m} \times 0.5\,\mathrm{m}$ and $7.3\,\mathrm{m} \times 1\,\mathrm{m} \times 0.25\,\mathrm{m}$ in length, height and depth. The wave tanks are made of glass which make them suitable for optical measurements.

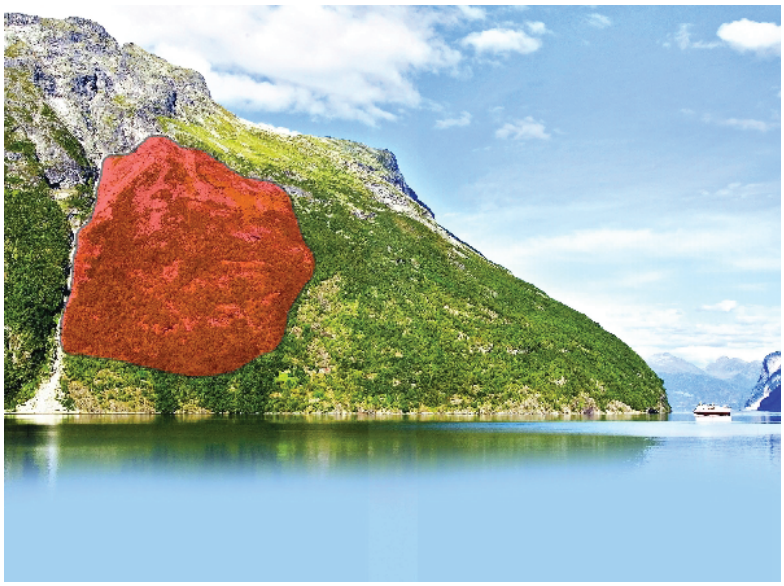

Figure 1: The unstable slope located in Åkneset. Image source: ÅTB

In this work, the larger wave tank was employed. At one end of the large tank a hydraulic piston type wave paddle is installed for wave generation. The movement of the wave paddle is controlled via a computer where input files in voltage for wave generation are stored. For the purpose of investigating runup, a beach was installed in the wave tank. The beach had an angle of 10 degrees and was made of PETG (Polyethylene Terephthalate Glycol-modified), this particular material was chosen with great care to ensure the beach would not absorb any water and that the transition between the beach and tank bottom was smooth.

Motivation of the runup study was to further investigate scale effects during runup with particular focus on viscous effects, inspired by the work of Sælevik *et al.* (2013). Solitary waves with amplitudes ranging from one-tenth of the equilibrium water depth to half the depth was generated, detailed observations of different aspects of the flow during inundation was performed. Two inviscid numerical models were employed for comparison, Boussinesq model and boundary integral (BIM) full potential model. For boundary layers, nonlinear boundary layer theory were employed where the outer flow was extracted from the Boussinesq or BIM model. Surface elevations on constant depth, before the wave reached the beach, displayed excellent agreement with theory. The first part of the laboratory work was devoted to track the shoreline position during runup. The smallest incident wave displayed significant deviation form theory in the early stage of the runup. The experimental inundation lag behind the theoretical one, before it nearly catch up and then fell behind again. The same behavior were detected for the larger waves, but not as pronounced. In order to reveal more details, contact angle dynamics were investigated and surface tension was the main suspect for the early stage discrepancies. The largest discrepancy of the shoreline position were detected in the later stage of the runup, with reduced inundation lengths for the experiments compared to theory. Viscous effects were believed to be the cause of the reduced runup heights, and therefore measurements of boundary

layers were performed. Due to practical reasons, only three locations at the beach was employed in order to reveal details about the boundary layer, two close to the equilibrium shoreline position and the third $0.8\,\mathrm{m}$ further up along the beach. Boundary layers were detected in the flow, showing good agreement with theory for the lower location at the beach. At the upper location irregularities were observed in the boundary layer flow for the same time as the theoretical profiles displayed an inflection point. These irregularities were recognized as small undulations in the front of the runup tongue which evolved to eddies. The flow started its withdrawal in the boundary layer, and estimates of integrated mass flow reduction caused by the boundary layers were quantitatively reconcilable with the difference in runup height between models and experiments. This study is presented in part I of this thesis.

Occurrence of irregularities in the boundary layer motivated new investigations, and comprehensive theoretical and numerical work on stability of boundary layers under solitary waves started within the department by Verschaeve & Pedersen (2013). Due to the complexity of the problem, solitary waves propagating on constant depth were addressed and findings implied that the boundary layer always was unstable in some regions behind the crest, where the first occurrence of disturbances in the boundary layer flow are Tollmien Schlichting waves. These waves are the initial part of the process of transition in the boundary layer and are two dimensional disturbances which are periodic in time and space. The findings of Verschaeve & Pedersen (2013) were in contradiction to earlier work which suggested that the stability were dependent on a critical Reynolds number (Vittori & Blondeaux, 2008; Sumer *et al.*, 2010; Vittori & Blondeaux, 2011; Celalettin *et al.*, 2013). A new experimental setup were designed for a master thesis (Denis, 2014), considering instabilities in the boundary layer under a solitary wave propagating on constant depth. The idea was to look for irregularities in the boundary layer, firstly without perturbation and secondly with a controlled perturbation in order to increase the strength of the disturbances. Due to a strict time limit, experiments including perturbations never took place. Instead, data from the experiments without perturbations were carefully checked for irregularities but no signs of instabilities were detected even for the largest waves. This indicates that perturbations are necessary in order to get the strength of the disturbances needed to detect Tollmien Schlichting waves. Since irregularities were detected in the work on runup (Pedersen *et al.*, 2013), experimental data were revisited in order to reveal more details about the fluctuations. With increased knowledge about occurrence of Tollmien Schlichting waves a new filtering procedure were employed at the same data for which fluctuations were observed. Intermittent structures of roughly sinusoidal shape waves were detected and compared with numerical simulations based on the Orr-Sommerfelt equations. The dominant length of the experimental undulations turned out to be close to the length of the Tollmien Schlichting waves extracted from simulations and the time of appearance of instabilities were in very good agreement. It should be noted that experimental data was limited and further experiments are needed, designed for the particular goal of investigating Tollmien Schlichting waves. Findings of irregularities in boundary layers during runup implies that numerical models where boundary layer theory is employed may not be sufficient to properly resolve the details of solitary waves running up a beach. The study of detected irregularities in the boundary layer during runup is presented in part II of this thesis.

Experiments performed in a three dimensional fjord model, large scale

Two out of three years of my PhD studies have been devoted to the unstable slope at Åkneset. For the experiments conducted at the Coast and Harbor Research Laboratory a 1:500 scale model covering the inner part of Storfjorden, Norway, was constructed (SINTEF, 2008). The fjord model is shown in figure 2. The model geometry was based on the real fjord bathymetry, provided by the Norwegian Geological Survey. The material used was plaster concrete and filling material, which was covered with a membrane to avoid leakage and reduce roughness. In order to be able to perform optical measurements, the concrete bottom was replaced by a glass bottom of circular shape with a diameter of $\sim 0.1\,\mathrm{m}$ at chosen locations. The model was strengthened in the impact area due to the heavy loading of the slide during impact. In order to ensure a smooth and repeatable slide motion, the model was modified as a plane of 38^o at the slide site. The model had a total size of $36 \times 40\,\mathrm{m}$ with a maximum depth of $0.64\,\mathrm{m}$ and maximum fjord width of $4\,\mathrm{m}$. The unstable slope was represented by a block slide model. This decision was based on deposits from earlier incidents in Storfjorden, displaying that the slide movement is terminated by the facing slope of the fjord and laterally confined (Blikra *et al.*, 2005), while granular slide deposits display wide fans. Recommended front angle of the slide was 30 degrees (not more than 45 degrees and not less than 15 degrees), relative to the slide plane (NGI, 2014). More details about the construction are given in Lindstrøm *et al.* (2014).

The experimental work from 2008 (NGI, 2011; Harbitz *et al.*, 2014*b*) was based on the worst case scenario with slide volume corresponding to 54 million m^3. A disadvantage with this particular slide was that it consisted of 12 blocks, where 8 were placed at the slide plane and 4 were placed on top of the bottom blocks, in addition, the front of the slide was perpendicular to the slide plane. This resulted in a remarkably violent impact. The experimental work from 2008 was used as background material when a new experimental setup was planned in 2011. Comprehensive work were conducted in improving the slide, to make the slide movement repeatable and increase the ability to measure its position and velocity. Both acoustic and resistance gauges were applied to measure the surface elevation in the fjord, these wave gauges were installed at 8 bridges at different locations in the fjord model, giving a total of 49 positions. The acoustic gauges were also employed to measure the flow depth onshore in the two villages Hellesylt and Geiranger located at the fjord ends at 18 positions. Inundations at Hellesylt and Geiranger were recorded with a high speed video camera, giving the full history of the shoreline position during inundation. A high speed camera was also employed to measure the maximum runup height at the facing slope of the slide region. Surface velocities were measured in Hellesylt to achieve information of the flow direction. Particle velocities as well as velocity fields were measured at chosen locations in the fjord. This extensive experimental investigation provides a large data set for validation of numerical models. It is valuable in the sense that the fjord geometry is complex and different aspects of the flow is measured. A part of this data set is presented in part III of this thesis, where the characteristics of the generated wave field and inundation are highlighted. Results from velocity measurements are not included in this part, but presented in section *Velocity measurements in large scale facilities* which is a part of the introduction.

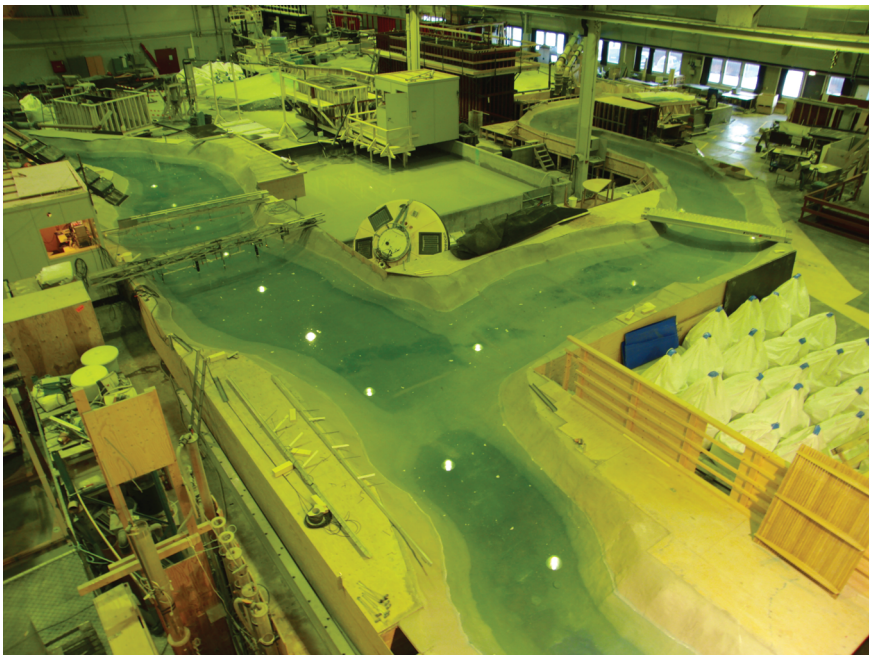

Figure 2: Picture of the fjord model, the slide is located in the upper left

Laboratory techniques

Experiments has been carried out at the hydrodynamic wave laboratory at the University of Oslo and at the Coast and Harbor Research Laboratory/SINTEF in Trondheim. During my work, a number of measuring techniques have been employed to investigate different aspects of the flow. Including surface elevation, inundation, velocity fields, particle velocities and surface velocities. Most of the techniques are applied in both large and small scale, adjusted for the environment.

Surface elevation measuring techniques

Surface elevation may be measured with both intrusive an non-intrusive instruments. Resistance wave gauges are intrusive and measure the resistance of the water between two parallel wires. Calibration is performed by collecting data while the gauges are exposed to a known elevation or depression. The collected data is then used to convert the signal from voltage to meter. One disadvantage is that the gauges are sensitive to drifting and this calibration procedure needs to be done quite frequently. Advantages is that they are robust, low-cost and are able to measure steep waves. One must be aware of capillary effects that may interfere with the gauges, which decreases the accuracy.

Ultra sonic wave gauges, or acoustic wave gauges, are non-intrusive. The probe emits pulses of ultrasonic energy, which travel through the air at the speed of sound. The energy reflects off the target and travels back to the sensor. Calibration procedure for these gauges are straightforward and only needs to be done once. The advantages are that these gauges are able to measure

very small amplitudes, they may be placed in shallow water and on shore. Disadvantages are that they are not able to measure waves steeper than 10 degrees. In 2012 a new set of acoustic gauges were bought, which experienced more noise in the signal than the old ones. In order to to accurate measurements a large amount of work was put in to develop a filter suitable for this particular noise, described in Appendix A.

Velocity measuring techniques

As for surface elevation measurements, particle velocities may be measured with both intrusive and non-intrusive techniques. Particle Image Velocimetry (PIV) are non-intrusive while acoustic doppler velocimeter gauges (ADV) are intrusive. Surface velocities were measured with large scale PTV, which is close related to PIV and non-intrusive.

PIV is an optical measuring technique which measure the velocity field in the flow. In this study, traditional two-dimensional PIV measurements have been applied. Three dimensional PIV systems are recently introduced into the market but these are not yet employed at the University of Oslo. A PIV system require recording device, optics, light source and seeding particles. The light source is formed into a light sheet which illuminates the seeding particles. The seeding particles are neutrally buoyant and follow the fluid movement without interfering with the flow. The image, or field of view, is divided into sub-windows and velocity vectors are found for each sub-window by pattern matching within two subsequent images. Each sub-window must contain a suitable number of particles in order to achieve an adequate result. The result is a two-dimensional velocity field for the chosen field of view, with spatial resolution dependent of the number of sub-windows and temporal resolution dependent of the flow characteristics as well as the capacity of the recording device. More details about PIV, including the mathematical background is to be found in Raffel *et al.* (2007) and Sveen & Cowen (2004).

The PIV method described above is not suitable for three dimensional flow due to plane loss of particles. The recording time is also limited by the local storage in the recording device, due to the large amount required for storage of images. Hence, if one wish to measure three dimensional flows for a longer time period, ADV is a more suitable device. ADV measure three velocity components at one single point. The concept is that a short acoustic pulse is emitted from the gauge, the echo of the transmitted pulse is recorded and processed in order to find the doppler shift. Once the doppler shift is found, the velocity components are calculated where the scaling is adjusted with the speed of sound in water. The collected data is then transmitted to a computer. ADV measurements often suffer from a large amount of noise, this may be reduced by adding particles in the water. A picture of ADV gauges are shown in figure 3, where also resistance wave gauges and acoustic wave gauges are placed at the same bridge.

Surface velocities are measured with Large Scale PTV (LSPTV). PTV is closely related to PIV and require similar hardware, PTV require five subsequent images for tracking velocities while PIV require two subsequent images and which make PTV more demanding when it comes to time resolution. The main difference between PTV and PIV is that PTV traces each particle in a Lagrangian way instead of pattern matching of sub-windows. In LSPTV the focus is to reveal details about two dimensional large coherent structures in the surface. The measurements are carried out at the surface which means that no light sheet is needed and instead of neutrally buoyant particles the flow is seeded with floating particles. More details are to be found in

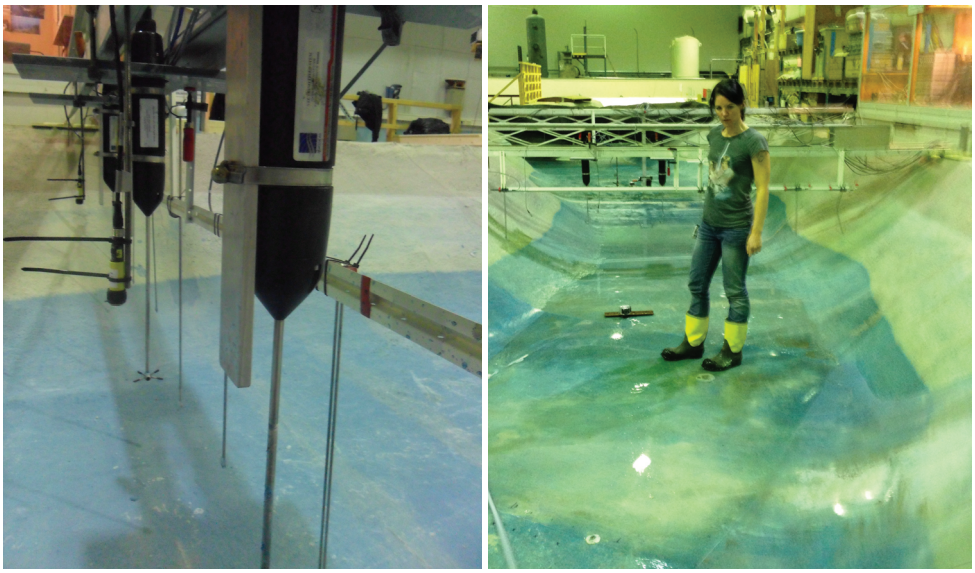

Figure 3: Picture of ADV, acoustic and wave resistance gauges. Left: Closeup of the gauges. Right: The bridge on which the gauges are installed, me and Luke Skywalker.

Weitbrecht *et al.* (2002). This kind of investigation require that the horizontal structures is of much larger length scale than the vertical, which is the biggest limitation of this measuring technique. Anyhow, this kind of investigation gives qualitative information about the flow.

Tracing of the moving shoreline during inundation

For shoreline tracing a high speed camera is used as a recording device, which is attached above the wavetank or model. The camera are placed perpendicular to the area to be investigated in order to avoid distortion due to unfavorable angles and shadow effects. In addition, it is an advantage to increase the contrast between the water and dry land to facilitate the processing. This method has the advantage that it gives the entire inundation of the flow until the maximum runup height is reached. It is very demanding to trace the shoreline after the maximum height of the leading wave is reached due to reflections in the wetted areas. A picture of the setup from small scale measurements are shown in figure 4.

Velocity measurements in large scale facilities

A part of the project was to measure velocities in the three dimensional fjord model. These measurements reveal important information of the generated wave field which is not captured in surface elevation measurements. Three dimensional velocities in one single point, two dimensional velocity fields and surface velocities were measured in the fjord model. Particle velocity measurements were conducted in the same region, bridge R, while surface velocities were measured in Hellesylt. These two locations are shown in figure 5. Acoustic doppler velocimetry (ADV) were employed for the single point measurements, this method is well suited

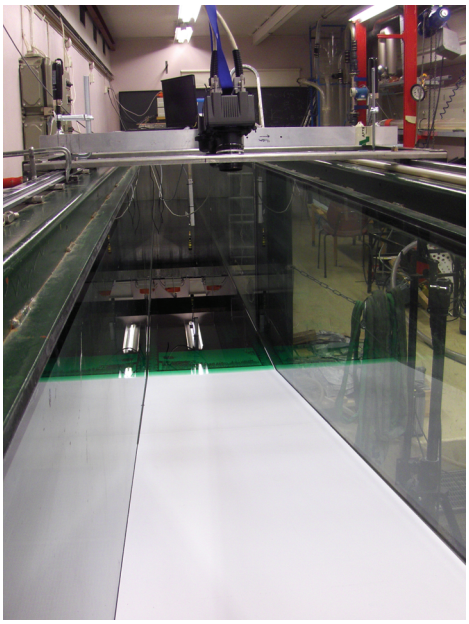

Figure 4: Image taken at the Hydrodynamic Laboratory, UiO. The high speed camera recording the shoreline position during runup is placed above the beach, a white PVC-film is attached to the beach and the water is colored green to increase contrast between water and beach.

for large scale experiments as long as the water is seeded with particles to increase the signal to noise ratio of the measurements. For the velocity fields particle image velocimetry (PIV) was used as method. Since PIV is an optical method, a concrete model is not optimal. Therefor, the model was built with the possibility to shoot laser from underneath the model at chosen positions. Specially designed equipment were necessary for the PIV investigation. Surface velocities were estimated by the method of large scale particle tracking velocimetry (LSPTV). This method require coherent structures that are much larger in the horizontal direction than the vertical in order to achieve results that are trustful.

PIV measurements were conducted in November 2012 while ADV, surface elevation and LSPTV were conducted in January 2013. Repeatability of the generated wave field was established in early 2012 (Lindstrøm *et al.*, 2014), and results are discussed in relation to each other. All measurements were synchronized with the slide release.

Experimental setup and instrumentation

A submerged PIV system was required in order perform measurements. The concrete bottom of the model was replaced by glass bottom of circular shape with a diameter of approximately $0.1\,\mathrm{m}$ at chosen locations during construction of the model. PIV measurements at two of these positions were performed and results from one of them are presented here. The laser head were located on the floor outside of the model, with a laser arm constructed for the purpose to reach the position where the glass bottom was located from underneath the model with great precision.

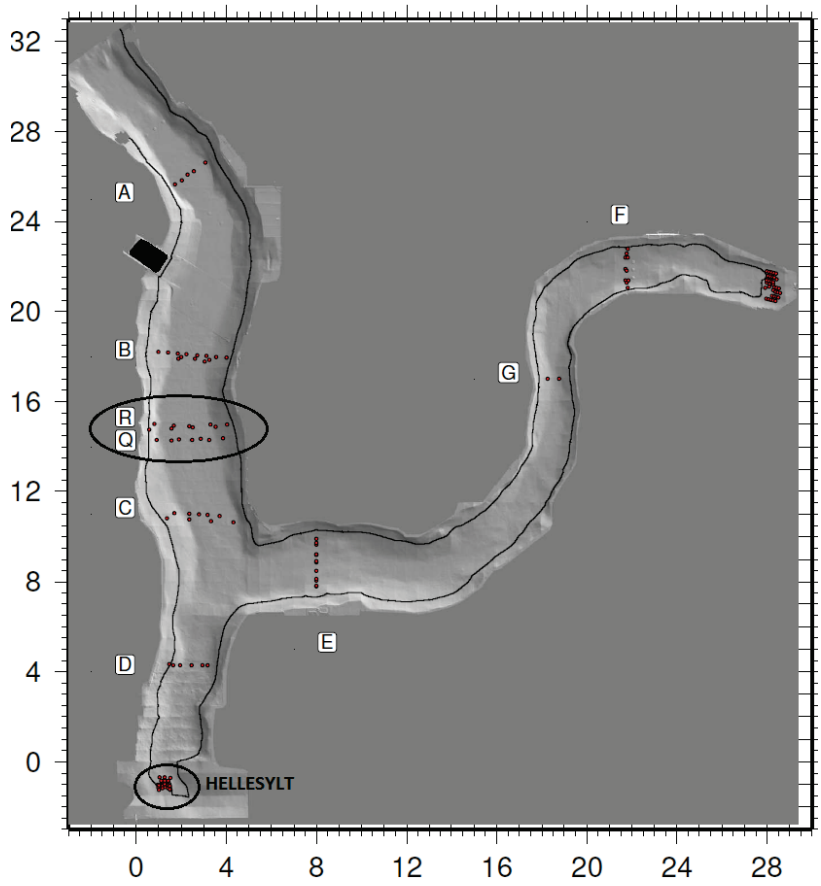

Figure 5: Image of the fjord scan. All coordinates for the measuring devices are illustrated by red dots while the slide is marked with black in the upper left. PIV, ADV and UL were located at bridge R while LSPTV were used in Hellesylt.

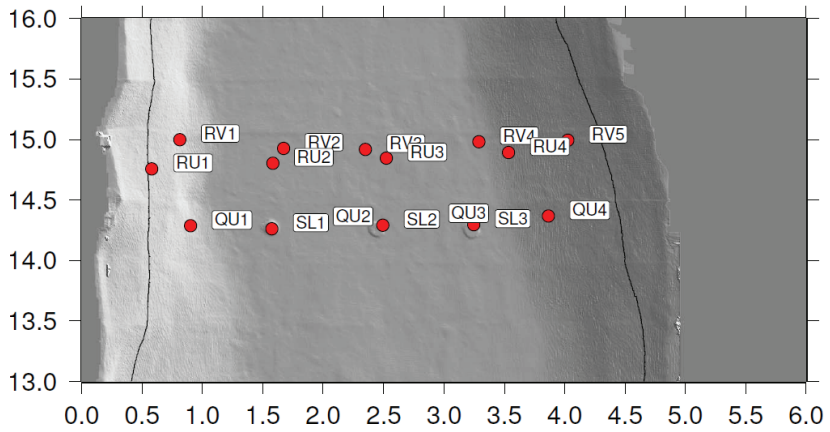

Figure 6: RVN corresponds to positions for doppler gauges, RUM corresponds to positions of ultra sonic wave gauges and SLL illustrates where the optics for PIV measurements were placed. $N = 1:5$, $M = 1:4$ and $L = 1:3$.

Optics which created the laser sheet were submerged and installed at bridge Q, located at the same position as the applied glass bottom. Locations of the optics are shown in figure 6, named SL1 and SL2. A water proof perspex box were built for the submerged high speed camera (Photron APX). The high speed camera had a pixel resolution of 1024×1024 with chosen time resolution of 99 frames per second. The field of view (FOV) had a size of $0.14\,\mathrm{m} \times 0.14\,\mathrm{m}$. $50\mu m$ polyamid spheres were used as tracer particles. The seeding was demanding due to the large size of the model which resulted in particle spreading. Digiflow (Dalziel, 2012) was used for processing with interrogation areas of 128×128 pixels and 50% overlap, the relatively large interrogation windows were required in order to have a suitable number of particles within each window. An image taken during one PIV experiment is shown in figure 7 while figure 8 shows the glass bottom of circular shape together with one of the ADV gauges.

In total five positions were employed for ADV gauges (vectrino). The gauges were uniformly distributed across bridge R with varying depth. ADV gauges measure all three velocity components in one single point. Here we define u as the velocity component along the direction of the wave propagation, w as vertical component and v as the transverse component. The gauges were named RV1-RV5, where the integer counts the relative position with increasing x. The position of the gauges are shown in figure 5 and 6, coordinates and depths for the gauges are given in table 1. Seeding particles ($50\mu m$ polyamid spheres) were added into the water to reduce noise level in the measurements and the sample rate was $200\,\mathrm{Hz}$.

For the LSPTV a high speed camera (Photron APX) were located $5.9\,\mathrm{m}$ above the model. Pixel resolution of the camera was 1024×1024 and a frame rate of 1000 frames per second was used. The resulting field of view had a size of $1.2\,\mathrm{m} \times 1.2\,\mathrm{m}$. Figure 9 shows the position of the high speed camera. The water surface was seeded with polypropylene particles with diameters of $2 - 4\,\mathrm{mm}$ and density of $0.90\,\mathrm{kg/m^3}$. To avoid agglomeration effects the particles were coated with a thin layer of lacquer. Choice of particles and coating were based on the work by Weitbrecht *et al.* (2002), who evaluated different types of particles for the use of large scale PIV

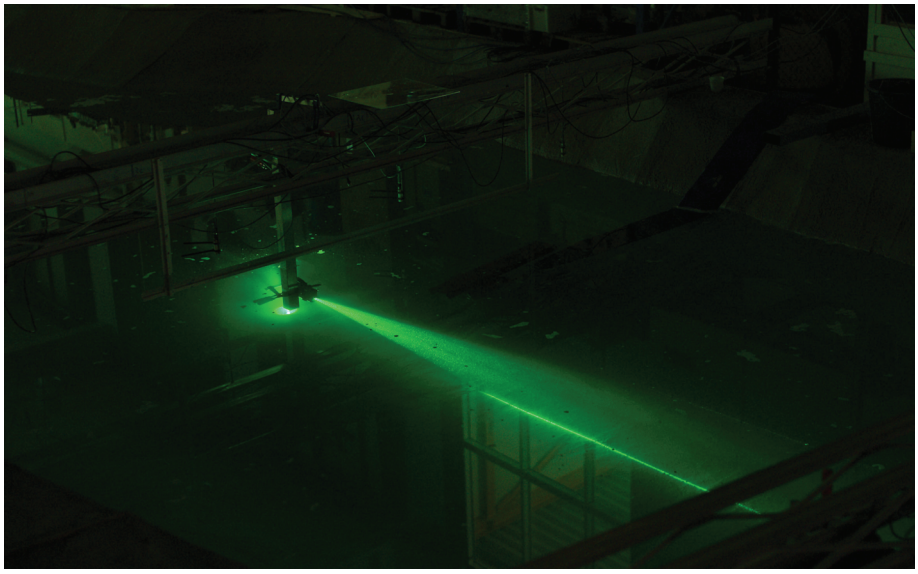

Figure 7: An image taken during the PIV experiments, showing the submerged optics and light sheet.

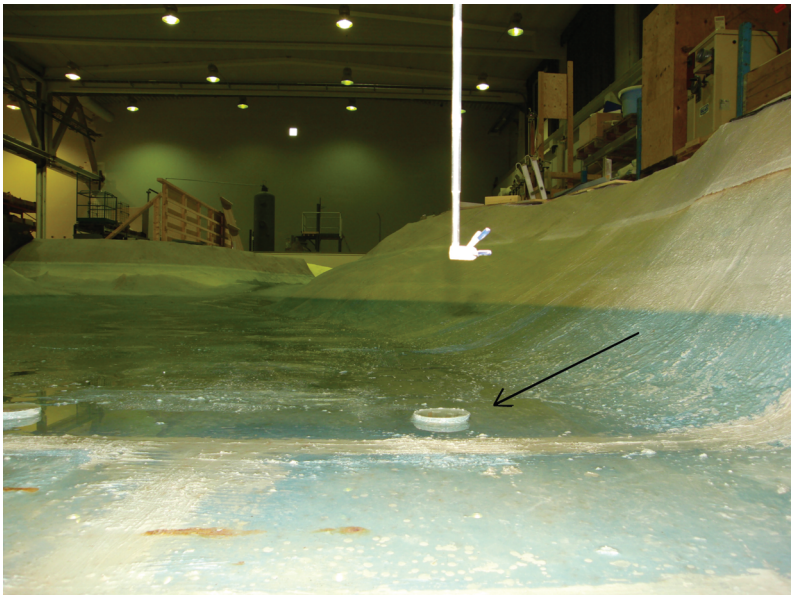

Figure 8: The bottom of the tank, the black arrow shows the position of the circular glass bottom where the laser beam exits from underneath the model. The picture also shows one of the ADV gauges.

Gauge	$x\ [m]$	$y\ [m]$	$z\ [m]$	$u_{max}\ [m/s]$	$t_{max}\ [s]$
RV1	0.81	15.00	-0.15	0.11	4.15
RV2	1.67	14.93	-0.30	0.10	3.96
RV3	2.35	14.92	-0.30	0.10	3.97
RV4	3.29	14.98	-0.45	0.10	3.95
RV5	4.03	14.99	-0.15	0.16	4.17

Table 1: Positions of the ADV gauges, where $z = 0$ is the equilibrium water level. u_{max} is the maximum horizontal velocity measured for the leading wave and t_{max} is the corresponding time

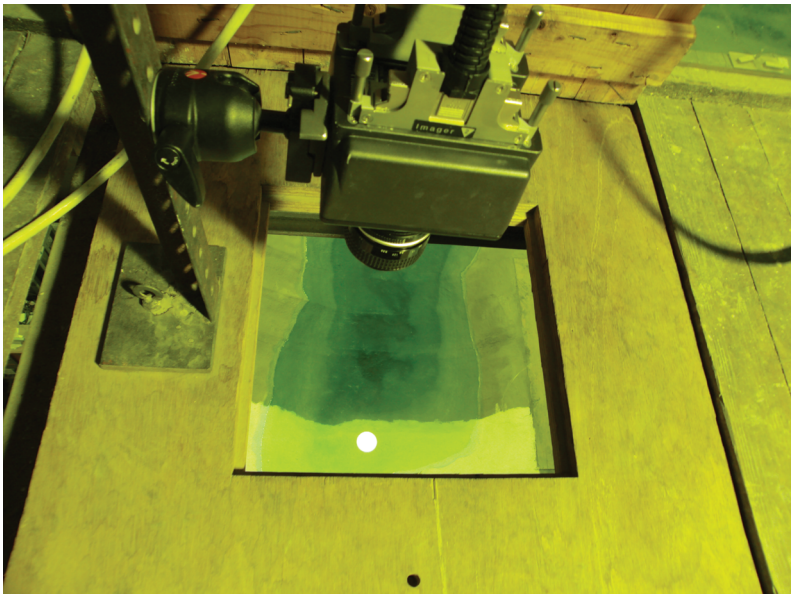

Figure 9: Picture of the high speed velocity camera placed $5.9\,\mathrm{m}$ above the fjord model during LSPTV measurements

and concluded that coated polypropylene gave the best results. The processing was performed using DigiFlow (Dalziel (2012)). In figure 9 the seeded water are shown together with velocity streaks extracted from the images during runup.

Results

Velocity fields

One ultrasonic wave gauge was placed above the field of view applied the PIV investigation. Surface elevation from this gauge is shown in figure 11 together with velocity profiles from the PIV data. PIV data and surface elevation are extracted at $x = 1.58\,\mathrm{m}$, $y = 14.80\,\mathrm{m}$. Good agreement of surface elevation and velocities are shown for the same time-frames. PIV measurements reveal maximum velocity at the same time as the leading wave display its maximum amplitude. Minimum velocity occurs at the same time as the first depression of the wave. Re-

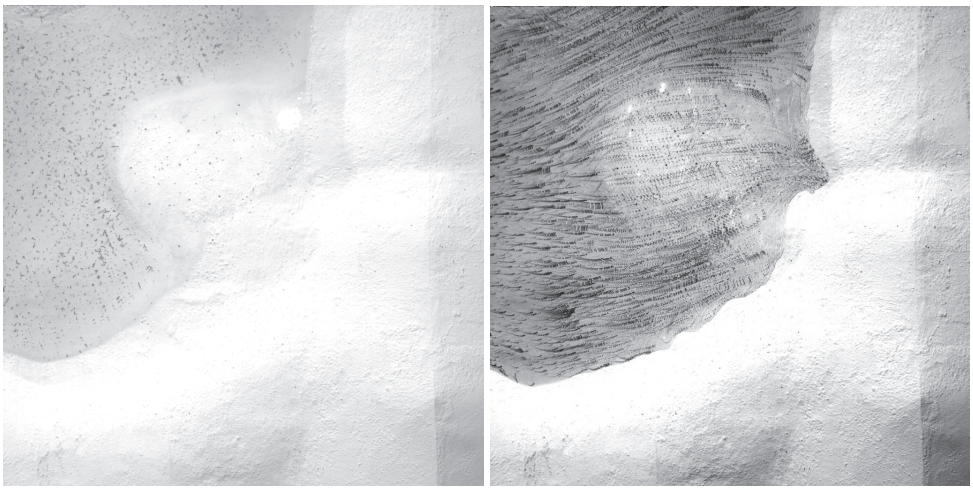

Figure 10: Left: Image of Hellesylt with seeding particles. Right: Velocity streaks extracted from PTV.

peatability of the PIV measurements display a maximum deviation of 3.6%, based on three different runs.

Single point measurements

Particle velocities for RV1-RV5 are shown in figure 12 to 14. For the leading wave the velocity component along the direction of the wave propagation, u, is much larger than the vertical velocity component, w, and the transverse component, v for all gauges. Maximum horizontal velocity of the leading wave for all gauges are given in table 1 together with the corresponding time. The largest horizontal velocity for the leading wave is measured at RV5 which is located close to the opposite fjord side of the slide region at $z = -0.15\,\mathrm{m}$, while RV1-RV4 display almost the same maximum horizontal velocity for the leading wave. Transverse variation are visible in the following wave train which is characterized by oscillations where all three components are comparable in magnitude. Surface elevations are not measured at the exact same positions as the ADV, but confirm the transverse variation and are shown in figure 15. No smoothing of the data is done. Repeatability is visualized in figure 12 for RV1, and considered to be satisfactory, at least for the first part of the wave train.

Surface velocities

Surface velocities were measured to reveal large coherent structures of in the surface. Earlier, flow depth and shoreline positions were measured in Hellesylt but due to the complex geometry and flow pattern more details were wished for. In order to extract exact surface velocities, three dimensional effects of the flow needs to be included in the processing. This is far from straight forward and considered to be future work. Anyway, directions of the flow and magnitude of velocities are revealed even for the two dimensional case, and in figure 16 an example is shown, where the flow changes its direction during inundation, where the shoreline position

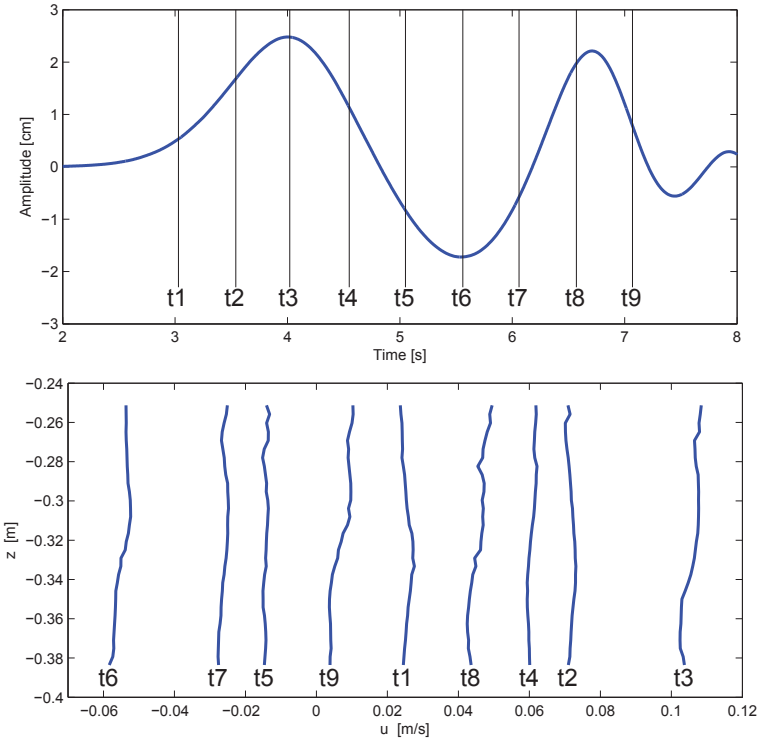

Figure 11: Upper: Surface elevation collected by an ultrasonic wave gauge located above the field of view applied in the PIV measurements. Lower: Velocity profiles $u - y$ measured with PIV.

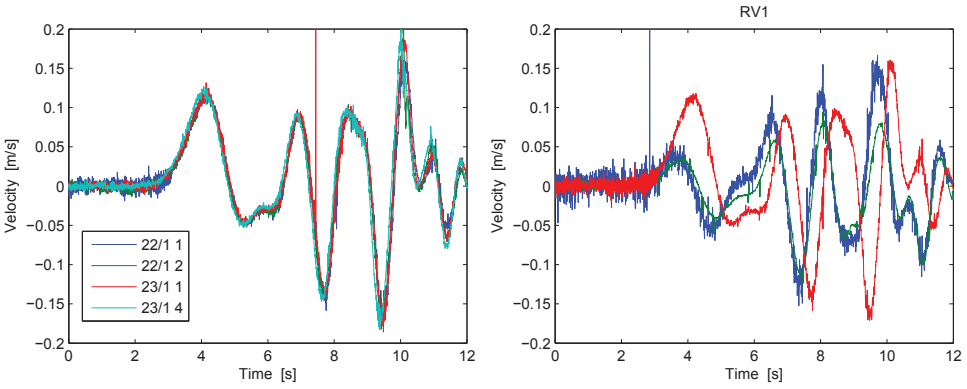

Figure 12: Left: Repeatability of the measurements, 4 runs are shown for RV1. Right: Measured velocities RV1 ($z = -0.15$), u-red, w-blue and v-green.

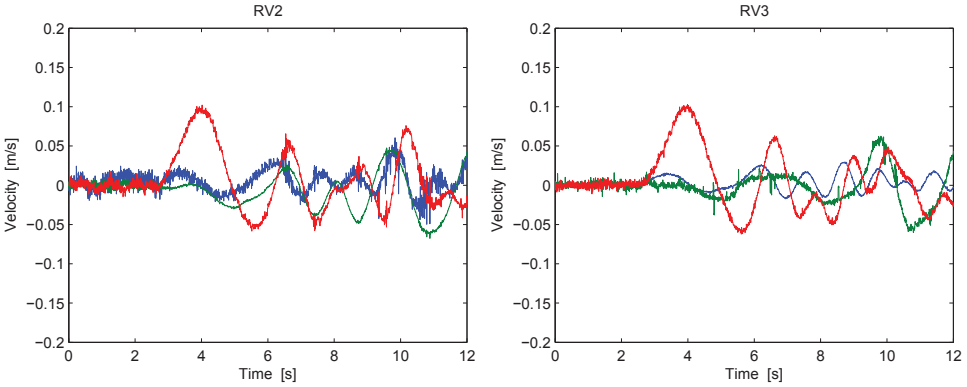

Figure 13: Measured velocities, u-red, w-blue and v-green. Left: RV4 ($z = -0.30$). Right: RV5 ($z = -0.30$).

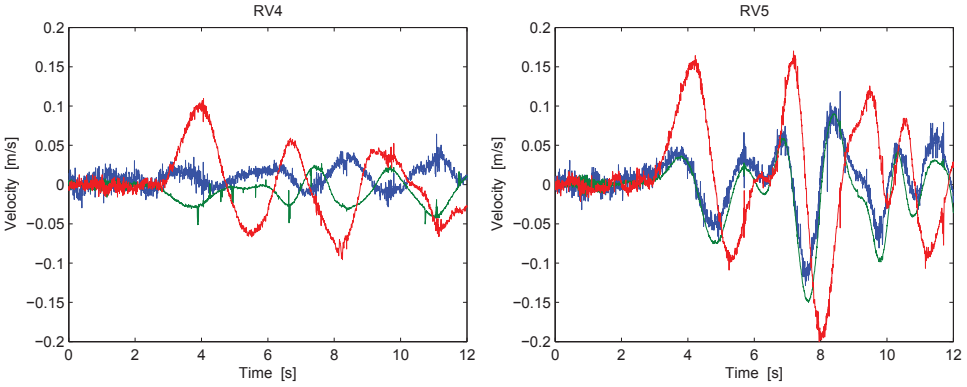

Figure 14: Measured velocities, u-red, w-blue and v-green. Left: RV4 ($z = -0.45$). Right: RV5 ($z = -0.15$).

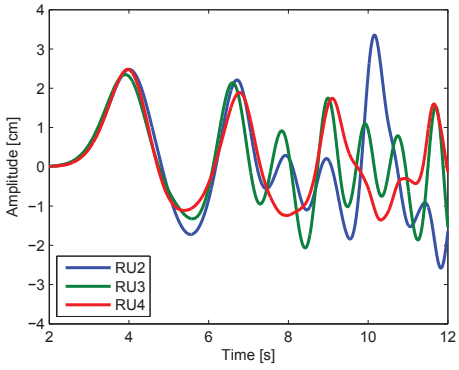

Figure 15: Surface elevation collected by an ultrasonic wave gauge located above the field of view applied in the PIV measurements

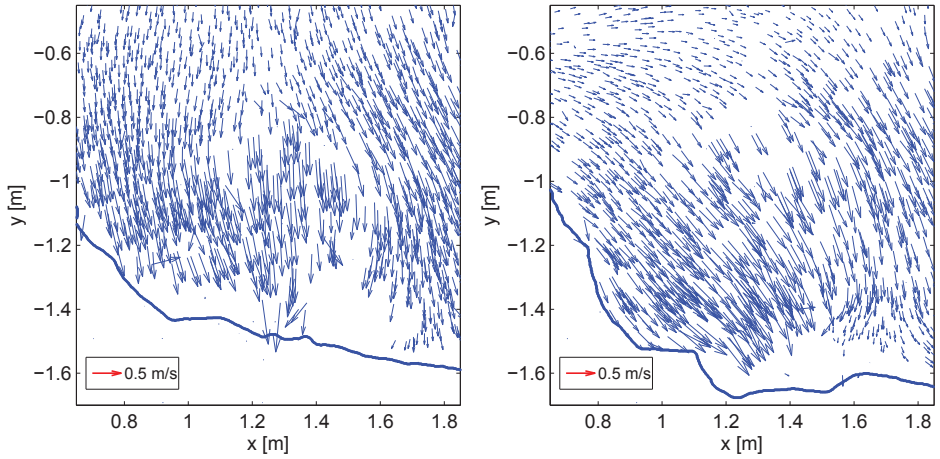

Figure 16: Surface velocities in Hellesylt, lack of vectors in the front is caused by poor seeding. Left: $t = 13.3\,\mathrm{s}$. Right: $t = 14.0\,\mathrm{s}$

is represented by a blue line and extracted from earlier measurements (Lindstrøm *et al.*, 2014)

References

BANNER-ENGINEERING 2013
URL: *http://info.bannerengineering.com/cs/groups/public/documents/literature/110738.pdf*.

BLIKRA, L. H., LONGVA, O., HARBITZ, C. B. & LØVHOLT, F. 2005 Quantification of rock-avalanche and tsunami hazard in storfjorden, western norway. *Landslides and Avalanches ICFL Norway* pp. 57–64.

CARRIER, G. F. & GREENSPAN, H. P. 1958 Water waves of finite amplitude on a sloping beach. *Journal of Fluid Mechanics* **17**, 97–110.

CELALETTIN, E. O., HSU, T.-J. & BALACHANDAR, S. 2013 Direct numerical simulations of instabilities and boundary layer turbulence under a solitary wave. *Journal of Fluid Mechanics* **731**, 545–578.

DALZIEL, S. B. 2012 Digiflow user guide.
URL: *http://www.dalzielresearch.com/digiflow*.

DENIS, H. I. 2014 Experimental investigation of the boundary layer under a solitary wave. Master's thesis, Univeristy of Oslo.

FRITZ, H., HAGER, W. H. & MINOR, H. E. 2001 Lituya bay case: rockslide impact and wave run-up. *Science of Tsunami Hazards* **19**, 1–67.

FRITZ, H. M., MOHAMMED, F. & YOO, J. 2009 Lityua bay landslide impact generated mega-tsunami 50th anniversary. *Pure and Applied Geophysics* **166**, 153–175.

GEIST, E. & PARSONS, T. 2006 Probalistic analysis of tsunami hazards. *Natural Hazards* **37** (3), 277–314.

GEIST, E. L., TITOV, V. V. & SYNOLAKIS, C. E. 2006 Tsunami: Wave of change. *Scientific American* **294**, 56–63.

GLIMSDAL, S., PEDERSEN, G. K., HARBITZ, C. B. & LØVHOLT, F. 2013 Dispersion of tsunamis: does it really matter. *Natural Hazards and Earth System Sciences* **13**, 1507–1526.

GOPALAKRISHNAN, T. C. & TUNG, C. C. 1980 Run-up of non-breaking waves - a finite element approach. *Coastal Engineering* **4**, 3–22.

HALL, J. V. & WATTS, J. W. 1953 Laboratory investigation of the vertical rise of solitary waves on impermeable slopes. *Tech. Memo. 33* .

HARBITZ, C. 1992 Model simulations of tsunamis generated by the storegga slides. *Marine Geology* **105**, 1–21.

HARBITZ, C., LØVHOLT, F. & BUNGUM, H. 2014*a* Submarine landslide tsunamis: how extreme and how likely? *Natural Hazards* **72** (3), 1341–1374.

HARBITZ, C. B., GLIMSDAL, S., LØVHOLT, F., KVELDSVIK, V., PEDERSEN, G. K. & JENSEN, A. 2014*b* Rockslide tsunamis in complex fjords: From an unstable rock slope at åkerneset to tsunami risk in western norway. *Coastal Engineering* **88**, 101–122.

HARBITZ, C. B., PEDERSEN, G. K. & GJEVIK, B. 1993 Numerical simulations of large water waves due to landslides. *Journal of Hydraulic Engineering* **119**, 1325–1342.

HOOPER, A., PIETRZAK, J., SIMONS, W., CUI, H., RIVA, R., NAEIJE, M., VAN SCHELTINGA, A. T., SCHRAMA, E., STELLING, G. & SOCQUET, A. 2013 Importance of horizontal seafloor motion on tsunami height for the 2011 mw=9.0 tohoku-oki earthquake. *Earth and Planetary Science Letters* **361**, 469 – 479.

JENSEN, A., PEDERSEN, G. & WOOD, D. J. 2003 An experimental study of wave run-up at a steep beach. *Journal of fluid mechanics* **486**, 166–188.

LAY, T., KANAMORI, H., AMMON, C. J., NETTLES, M., WARD, S. N., ASTER, R. C., BECK, S. L., BILEK, S. L., BRUDZINSKI, M. R., BUTLER, R., DESHON, H. R., EKSTRØM, G., SATAKE, K. & SIPKIN, S. 2005 The great sumatra-andaman earthquake of 26 december 2004. *Science* **308** (5725), 1127–1133.

LINDSTRØM, E. K., PEDERSEN, G. K., JENSEN, A. & GLIMSDAL, S. 2014 Experiments on slide generated waves in a 1:500 scale fjord model. *Coastal Engineering* **92**, 12–23.

LØVHOLT, F., GLIMSDAL, S., HARBITZ, C. B., HORSPOOL, N., SMEBYE, H., DE BONO, A. & NADIM, F. 2014 Global tsunami hazard and exposure due to large co-seismic slip. *International Journal of Disaster Risk Reduction*
URL: *http://www.sciencedirect.com/science/article/pii/S2212420914000326*.

LØVHOLT, F., GLIMSDAL, S., HARBITZ, C. B., ZAMORA, N., NADIM, F., PEDUZZI, P., DAO, H. & SMEBYE, H. 2012 Tsunami hazard and exposure on the global scale. *Earth-Science Reviews* **110**, 58 – 73.

LØVHOLT, F., LYNETT, P. & PEDERSEN, G. 2013 Simulating run-up on steep slopes with operational boussinesq models; capabilities, spurious effects and instabilities. *Nonlinear Processes in Geophysics* **20**, 379–395.

LØVHOLT, F., PEDERSEN, G. & GISLER, G. 2008 Oceanic propagation of a potential tsunami from the la palma island. *Journal of Geophysical Research* **113**, C09026.

MADER, C. L. 1999 Modelling the 1958 lituya bay mega-tsunami. *Science of Tsunami Hazards* **17**, 57–67.

NGI 2011 Numerical simulations of tsunamis from potential and historical rock slides in storfjorden; hazard and comparison with 3d laboratory experiments. *Tech. Rep.* 20051018-1-R. Norwegian Geotechnical Institute.

NGI 2014 Evolution if the flow characteristics of the potential åkerneset rockslide, western norway - contributions to design of laboratory experiments on wave generation. *Tech. Rep.* 20061333-01-R. Norwegian Geotechnical Institute.

NOREM, H., HARBITZ, C. B. & GLIMSDAL, S. 2007 Evolution of the flow characteristics of the potential åkneset rock slide, western norway - contributions to the design of laboratory experiments on wave generation. *Tech. Rep.*.

OKAL, E. A. & SYNOLAKIS, C. E. 2004 Source discriminants for near-field tsunamis. *Geophysical Journal International* **158** (3), 899–912.

PEDERSEN, G. & GJEVIK, B. 1983 Run-up of solitary waves. *Journal of fluid mechanics* **135**, 283–299.

PEDERSEN, G., LINDSTRØM, E., BERTELSEN, A. F., JENSEN, A., LASKOVSKI, D. & SÆLEVIK, G. 2013 Runup and boundary layers on sloping beaches. *Physics of fluids* **25**, 012102.

PEREGRINE, D. H. 1966 Calculations of the development of an undular bore. *Journal of Fluid Mechanics* **25**, 321–330.

PEREGRINE, D. H. 1967 Long waves on a beach. *Journal of Fluid Mechanics* **27**, 815–827.

RAFFEL, M., WILLERT, C., WERELEY, S. & KOMPENHANS, J. 2007 *Particle Image Velocimetry: A Practical Guide*. Springer.

ROMANO, F., PIATANESI, A., PIATANESI, A., LORITO, S., D'AGOSTINO, N., HIRATA, K., ATZORI, S., YAMAZAKI, Y. & COCCO, M. 2012 Clues from joint inversion of tsunami and geodetic data of the 2011 tohoku-oki earthquake. *Scientific Reports* **2**.

SÆLEVIK, G., JENSEN, A. & PEDERSEN, G. 2009 Experimental investigation of impact generated tsunami; related to a potential rock slide, western norway. *Coastal Engineering* **56**, 897–906.

SÆLEVIK, G., JENSEN, A. & PEDERSEN, G. 2013 Runup of solitary waves on a straight and a composite beach. *Coastal Engineering* **77**, 40–48.

SINTEF 2008 Notat - rasmodell (in norwegian). *Tech. Rep.*. SINTEF.

SUMER, B. M., JENSEN, P. M., SØRENSEN, L. B., FREDSØE, J., LIU, P. L.-F. & CARSTENSEN, S. 2010 Coherent structures in wave boundary layers. part 2. solitary motion. *Journal of fluid mechanics* **646**, 207–231.

SUPPASRI, A., MAS, E., CHARVET, I., GUNASEKERA, R., IMAI, K., FUKUTANI, Y., ABE, Y. & IMAMURA, F. 2013 Building damage characteristics based on surveyed data and fragility curves of the 2011 great east japan tsunami. *Natural Hazards* **66** (2), 319–341.

SVEEN, K. J. & COWEN, E. A. 2004 Quantitative imaging techniques and their application to wavy flows. *Advances in Coastal and Ocean Engineering* pp. 1–49.

SYNOLAKIS, C. E. 1987 The run-up of solitary waves. *Journal of Fluid Mechanics* **185**, 523–545.

SYNOLAKIS, C. E. & BERNARD, E. N. 2006 Tsunami science before and beyond boxing day 2004. *Philosohical Transactions: Mathematical, Physical and Engineering Sciences* **364**, 2231–2265.

SYNOLAKIS, C. E. & KONG, L. 2006 Runup measurements of the december 2004 indian ocean tsunami. *Earthquake Spectra* **22**, 67–91.

TAPPIN, D. R., WATTS, P. & GRILLI, S. T. 2008 The papua new guinea tsunami of 17 july 1998: anatomy of a catastrophic event. *Natural Hazards and Earth System Science* **8** (2), 243–266.

VERSCHAEVE, J. C. G. & PEDERSEN, G. K. 2013 Linear stability of boundary layers under solitary waves.
URL: *http://arxiv-web3.library.cornell.edu/abs/1309.7227*.

VITTORI, G. & BLONDEAUX, P. 2008 Turbulent boundary layer under a solitary wave. *Journal of Fluid Mechanics* **615**, 433–443.

VITTORI, G. & BLONDEAUX, P. 2011 Characteristics of the boundary layer at the bottom of a solitary wave. *Coastal Engineering* **58**, 206–213.

WARD, S. N. & DAY, S. 2001 Potential collapse and tsunami at la palma, canary islands. *Geophysical Research Letters* **28**, 3397–3400.

WEITBRECHT, V., KUHN, G. & JIRKA, G. H. 2002 Large scale piv-measurements at the surface of shallow water flows. *Flow Measurements and Instrumentation* **13**, 237–245.

WIEGEL, R. L. 1955 Laboratory studies of gravity waves generated by the movement of a submerged body. *Trans. AGU* **36**, 759–774.

WOOD, D. J., PEDERSEN, G. K. & JENSEN, A. 2002 Modelling of run up of steep non-breaking waves. *Ocean Engineering* **30**, 625–644.

Parts

Part I **Pedersen, Geir & Jensen, Atle & Lindstrøm, Erika & Bertelsen, Arnold F. & Laskovski, Daniela & Sælevik, Gunnstein** 2013
Runup and boundary layers on sloping beaches
Physics of fluids **25**, 012102.

Part II **Lindstrøm, Erika K. & Joris C. G. Verschaeve & Pedersen, Geir K.** 2014
A note on instabilities in the boundary layer during runup of solitary waves on a plane slope
Report, Department of Mathematics, UiO **No. 01**

Part III **Lindstrøm, Erika K. & Pedersen, Geir K. & Jensen, Atle & Glimsdal, Sylfest** 2014
Experiments on slide generated waves in a 1:500 scale model
Coastal Engineering **92**, 12-23.

Part I

Runup and boundary layers on sloping beaches

PHYSICS OF FLUIDS **25**, 012102 (2013)

Runup and boundary layers on sloping beaches

G. K. Pedersen,[1,a)] E. Lindstrøm,[1] A. F. Bertelsen,[1] A. Jensen,[1]
D. Laskovski,[1] and G. Sælevik[2]
[1]*Department of Mathematics, University of Oslo, Po. Box 1053, 0316 Oslo, Norway*
[2]*Drilltronics Rig Systems AS, Po. Box 361, Forus 4067, Stavanger, Norway*

(Received 11 January 2012; accepted 6 November 2012; published online 8 January 2013)

The present study is devoted to discrepancies between experimental and theoretical runup heights on an inclined plane, which have occasionally been reported in the literature. In a new study on solitary wave-runup on moderately steep slopes, in a wave tank with 20 cm water depth, detailed observations are made for the shoreline motion and velocity profiles during runup. The waves are not breaking during runup, but they do break during the subsequent draw-down. Both capillary effects and viscous boundary layers are detected. In the investigated cases the onshore flow is close to the transitional regime between laminar and turbulent boundary layers. The flow behaviour depends on the amplitude of the incident wave and the location on the beach. Stable laminar flow, fluctuations (Tollmien-Schlichting waves), and formation of vortices are all observed. Comparison with numerical simulations showed that the experimental runup heights were markedly smaller than predictions from inviscid theory. The observed and computed runup heights are discussed in the context of preexisting theory and experiments. Similar deviations are apparent there, but have often been overlooked or given improper physical explanations. Guided by the absence of turbulence and irregular flow features in parts of the experiments we apply laminar boundary layer theory to the inundation flow. Outer flows from potential flow models are inserted in a nonlinear, numerical boundary layer model. Even though the boundary layer model is invalid near the moving the shoreline, the computed velocity profiles are found to compare well with experiments elsewhere, until instabilities are observed in the measurements. Analytical, linear boundary layer solutions are also derived both for an idealized swash zone motion and a polynomial representation of the time dependence of the outer flow. Due to lacking experimental or theoretical descriptions of the contact point dynamics no two-way coupling of the boundary layer model and the inviscid runup models is attempted. Instead, the effect of the boundary layer on the maximum runup is estimated through integrated losses of onshore volume transport and found to be consistent with the differences between inviscid theory and experiments. © *2013 American Institute of Physics*. [http://dx.doi.org/10.1063/1.4773327]

I. INTRODUCTION

Experiments are crucial for assessment of runup on sloping beaches and flooding from tsunamis, storm surges, and swells in two ways. First, the measurements are scaled and used directly as indications of runup in real cases. Second, the experiments are used for benchmarking theoretical models of wave runup and impact on sloping beaches.[1,2] In both cases it is important to be aware of scaling effects. Generally, wave tank experiments are performed with maximum depths ranging from 10 cm to 50 cm, say. For depths of this order we expect only moderate effects of viscosity and surface tension.[3,4] However, when sloping beaches are included, very thin swash tongues are generated during runup and these may be more strongly influenced by viscosity, turbulence, and

a)Electronic mail: geirkp@math.uio.no.

capillary effects. Then, the runup may display a stronger scale dependency than propagation in finite depth. Yet, these issues are not much investigated, neither in the laboratory nor in theory. In this article we focus on the nature of the boundary layers on laboratory beaches and the performance of models in a laboratory context.

Experimental investigations on runup on beaches have mostly been concerned with solitary waves on inclined planes. Solitary waves are easy to generate and to control in a wave tank. In addition, the waves are easy to classify and reproduce since they are described by a single parameter, the amplitude most conveniently. Unfortunately, as models for oceanic waves solitary waves have shortcomings.[5] Still, solitary waves are established as a reference wave class for experimental investigations.

Some early experimental investigations on runup are reviewed by Meyer and Taylor.[6] A data-set that is much referred is the one by Hall and Watts.[7] Even though the observational techniques are partly primitive and the accuracy limited, this data-set is rendered attractive because of the wide span in the parameters and the availability of the digital results. Newer investigations tend to come with more limited selections of parameters and are generally performed with, for instance, a single, or a few slope angles. In addition, the studies are often focused on particular physical aspects. Synolakis[8] reported experiments on breaking and non-breaking solitary waves incident on 1 in 19.85 slope and compared with theory. Svendsen and Grilli[9] studied runup on selected, mostly steep, slopes, and compared with theory. The authors also made allegations to significant runup reduction due to bottom drag, but without analysis. Li and Raichlen[10,11] published measurements for runup on 1 in 2.08 and 1 in 15 slopes. Jensen *et al.*[12,13] investigated breaking on moderately steep slopes. Runup has also been measured in simple three-dimensional geometries, such as on a circular island.[14] More recently runup and flow field characteristics were measured on a broken slope and compared to those obtained on a single inclined plane in a wave tank with 20 cm as equilibrium depth.[15] An important observation was that experimental runup heights were markedly lower than theoretical predictions. Herein, this topic will be revisited in a set of experiments which is more carefully designed to reveal details in the runup.

Swash zone dynamics have been observed in the fields as well as the laboratory, often with emphasis on turbulent velocity profiles and sedimentation effects. Recent examples on application of PIV (Particle Image Velocimetry) to such flows are O'Donoghue *et al.*,[16] who investigate breaking bores on 1 in 10 slope, and Sou *et al.*[17] who study periodic waves on 1 in 20 slope. More references are given in these articles.

Carrier and Greenspan[18] presented the first nonlinear runup analysis. Their solution was based on a hodograph transformation of the shallow water equations for plane waves on an inclined plane and publications based on this methodology have continued to appear to this day. Numerical runup models have displayed a somewhat slow and encumbered evolution since the start around 1970. Today, runup models are incorporated in operational tsunami models[19–21] as well as freely available software for coastal engineering applications with Boussinesq type models.[22,23] Most runup models are confined to shallow water theory, with or without a scheme for capturing bores, while there are others that include dispersive effects, approximately or fully.[24] Apart from bore capturing facilities, viscous effects are mostly incorporated in such models as a manning friction term with an empirical coefficient. For simplified, and preferably two-dimensional, geometries also models based on full potential theory[25] or the Navier–Stokes equations with some technique to trace the free surface (SPH, VOF, levelset, multi-material) have been applied.[26–32]

Due to artificial viscosity and low order representations of surfaces, the accuracy of runup predictions from Navier–Stokes type models is limited and no attempt to resolve the boundary on the beach, let alone capillary effects and contact point dynamics, as part of an integrated wave runup study has been reported. Anyhow, for large scale simulations, we still have to rely on the long wave, depth integrated, models that are mentioned above. Herein, we employ well controlled models[33] without viscous or empirical drag terms, and which will be explained subsequently.

There is a large literature on boundary layer theory for stationary and oscillatory outer flow. A recent experimental investigation on the latter is found in Carstensen *et al.*[34] Less progress is reported for transient boundary layers, such as will appear during solitary wave runup. Linear boundary layers, due to solitary waves, along the bottom and side walls of a wave tank was analyzed

by Keulegan[35] who obtained a simple formula for the damping rate. Later experiments on solitary waves in constant depth point to other factors as being more important for the amplitude decay.[3,4] Separation has been observed in simulations by Diamessis and Redekopp[36] and experiments by Carr and Davies[37] on internal solitary waves. Liu *et al.*[38] measured the bottom boundary layers in a wave tank of depth 10 cm for surface solitary waves of heights ranging from 0.1 to 0.5 times the depth. They found that the boundary layers were laminar, without separation, even in the retardation phase. The boundary layer was analyzed by entering the coordinate system moving with the wave celerity, where the flow is stationary and good agreement between theory and experiments was reported. Vittori and Blondeaux[39] subjected the evolution of boundary layer under solitary waves to DNS (Direct Numerical Simulation) computations and observed transition to non-laminar flow in the boundary layer during the retardation phase. In Sumer *et al.*,[40] a companion paper to Carstensen *et al.*,[34] a solitary wave is represented as a flow pulse in a duct. Transition to turbulence in the boundary layers were observed with an intermediate regime where vortex tubes appeared in the retardation phase.

In its full extent laboratory scale runup, including breaking/no-breaking waves, viscous boundary layers, capillary effects, contact point dynamics at the shoreline, significance of bottom roughness, is a topic which is far from fully explored. In the present article we aim at raising some important questions and taking a step toward a better understanding of some sub-topics, in particular related to model performance and viscous boundary layers in the swash zone. To this end our new runup measurements, some subsequent results and previous investigations from the literature are discussed together with theoretical predictions from potential flow analysis. For non-breaking waves it is found that potential theory systematically over-predicts maximum runup heights in comparison to small scale laboratory experiments. Such experiments may be influenced by surface tension and viscosity. Both effects are qualitatively observed in our experiments, but we focus on the viscous boundary layers on the beach. To our knowledge no detailed study of this kind has been presented in the literature. Both analytical and numerical boundary layer solutions are employed. These are applied to idealized type swash flows and outer flows obtained from the potential flow models. The feedback from the boundary layer solutions to the outer flow is not modelled in detail, but integrated effects from the boundary layers are related to the observed differences in runup heights between experiments and theory.

II. METHODS AND BACKGROUND

A. Experiments

Two sets of experiments on runup on sloping beaches have recently been performed in the Hydrodynamics Laboratory at the University of Oslo. Below we will describe the latter set, while a description of the first is found in Sælevik.[15]

The experiments were performed in a wave tank of width 0.5 m and height 1 m. Both the walls and bottom are made of glass, making the tank suitable for optical measurements. In the present experiment, a plane beach, of inclination $\theta = 10^\circ$, was installed such that the undisturbed shoreline was located 7.1 m from the wave paddle, corresponding to 35.5 equilibrium depths of $0.2\,\text{m} \pm 0.001\,\text{m}$. The beach was made of PETG (Polyethylene Terephthalate Glycol-modified). This is preferable to Plexiglas which may absorb water and deform accordingly. The roughness, k, of smooth plates made plastic materials is typically 7×10^{-6} m or smaller.[41,42] This is several order of magnitudes smaller than the boundary layer thickness in our experiments ($\sim$1 mm) and will hence not influence a laminar flow. For a turbulent boundary layer the wall may be regarded as smooth as long as the roughness is within the viscous sublayer, corresponding to[43] $Re_k = ku^*/\nu \leq 4$, where the friction velocity is defined as $u^* = \sqrt{\tau/\rho}$. In our experiments and computations we may recognize $\tau = 2\,\text{N/m}^2$ as a typical wall stress, yielding $Re_k \sim 0.3$. Hence, also turbulent flow would be little affected by roughness for our model configuration. But again, herein we only report results for laminar and transition flows.

The incident waves, of solitary shape, are generated by a piston type wave paddle as explained in Jensen *et al.*[12] A schematic view of the wave tank is shown in Figure 1.

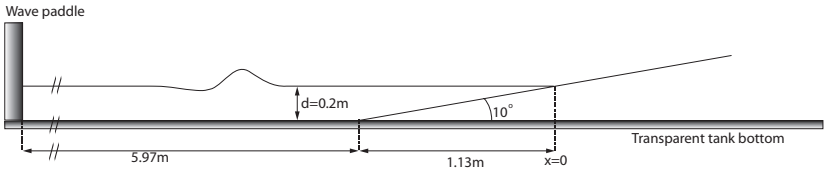

FIG. 1. Schematic side view of the wave tank.

The incident waves were measured by a non-intrusive acoustic wave gauge (Banner U-Gage S18U, sampling rate 200 Hz) at $x/d = -10.225$. The amplitudes were intended to range from one-tenth of the depth to half the depth. However, the vertical wave paddle cannot represent the velocity profile exactly and the generated waves are not perfect solitary waves, even though they are close. During propagation the shapes adjust toward that of a solitary wave, but the amplitude is meanwhile slightly reduced due to friction effects (see Miles[4] and Shuto[3]) during the propagation along the uniform part of the wave tank. The combined effects yield the modified values $A/d = 0.0977, 0.195, 0.292, 0.388, 0.481$. In accordance with the criterion (3) of Sec. II B we do not observe any sign of breaking during runup for the lowest four amplitudes, while there might be small intermittent irregularities at the shoreline for the largest amplitude. Errors in the parameters of the experimental setup will affect, among other things, the propagation time from wave gauge to the shoreline. If we assume errors in depth, gauge position, inclination angle and constant of gravity to be less than 1 mm, 2 mm, 0.1°, and 0.01 m/s^2, respectively, each will give an error in propagation time that will be 0.001–0.005s, say. This is relevant to the comparison between computed and observed flow in Sec. IV A.

A high speed camera (Photron APX 1024 × 1024 pixels) was recording the runup from above and the shoreline motion was digitized by an edge detection technique. The sampling rate was between 250 Hz and 1000 Hz, increasing with the amplitude of the incident wave. The physical images were quadratic, with sizes from 28 cm × 28 cm to 18 cm × 18 cm and the extracted edges from a sequence of images were used to piece together a total time history for the shoreline position. For the lowest amplitude two images were employed, while six windows were needed for $A/d = 0.292$. In these particular experiments the water was colored blue and the beach coated by a white PVC film. The maximum runup height displayed a repeatability within 1.5% error in subsequent experimental runs and had a transverse variation of 1% or less. The latter may be linked to small deviations of the beach from a perfect plane (up to 1.4 mm upward in the center, close to the equilibrium shoreline). For the largest incident wave ($A/d = 0.481$) we observe an opposing depression of the beach up to 1 mm due to the loading during inundation. These geometrical variations will probably not affect the flow properties much in the laminar regime, but may modify the transitional regime in boundary layers significantly. Using the pendant drop technique we found that adding the blue dye, in the concentrations used, did not influence the surface tension significantly (reduced from 71.84 mN/m to 71.69 mN/m). The contact point dynamics depends on the chemical properties of the water and the beach. For assessment of the properties of the PVC coated beach and dyed water versus the PETG beach and tap water the sessile drop test were performed, where the contact angles of a still drop on a plane of the beach material in question. The contact angles were 65.2° and 73.1°, respectively, indicating that the effect of surface tension through the contact point is slightly reduced for the PVC coated beach.

A PIV system was used to measure velocity fields. The PIV imaging device consisted of a Photron SA5 high speed camera, with a 1024 × 1024 pixels resolution at 2000–5000 frames per second. The illumination was provided by a Quantronix Darwin Duo pulsed laser giving 15 mJ per pulse at 3000 Hz, and light sheet optics. Fifty micrometer polyamid spheres were used as tracer particles. The cameras were aligned parallel to beach and FOVs (fields of views in the sense of physical regions captured in the images) of sizes 2.3 cm × 2.3 cm and 3.3 cm × 3.3 cm were centered at distances 7.5 cm and 81 cm from the equilibrium shoreline, respectively (see Figure 2, lower panel). The distance from the side walls was 5 cm. In addition, measurements were made in a 5.6 cm × 5.6 cm field of view 8 cm from the beach in the middle of the tank (25 cm from the

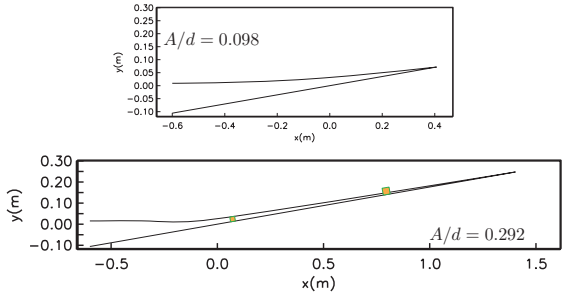

FIG. 2. Simulated (BIM) swash layers at the time of maximum runup, depicted with true aspect ratio. In the lower panel the two fields of view (FOV) for PIV measurements are shown.

side walls). However, these measurements were of lower quality and no quantitative data from this field of view is shown herein, even though qualitative features are discussed in Sec. IV A. The processing was performed using DigiFlow.[44] In a boundary layer the longitudinal velocity is much larger than the transverse one. We also need high transverse resolution in the measured velocity field to capture the gradient. Hence, we employ elongated interrogation areas of size 32×8 pixels, with 50% overlap, at the beach. Also Liu *et al.*[38] employed elongated interrogation areas in their study of boundary layers at a horizontal bottom. A general discussion on the shape of the interrogation area in relation to the characteristics of the flow is found in Ref. 45. The storage of the camera system has a capacity of 10 918 images, which allows for recording sequences of 2 s–5.5 s for the frame rates employed.

The camera was located outside the tank, while the laser was creating a light sheet from underneath the tank, thus avoiding reflections from the moving wave surface before entering the fluid.

Both the data from the wave gauges and the HSV (High Speed Video) recordings were synchronized with the start of the paddle motion. Thus, times referred to herein are measured from the paddle start, unless otherwise is specified in the text.

B. Runup theory

From the geometry, the fluid properties and the incident wave characteristics we infer that the maximum runup height, R, on the sloping beach is governed by the parameters A, d, θ, g, ν (kinematic viscosity coefficient), ℓ (distance from reference position of incident wave to the toe of the beach), σ (surface tension as force per length), and ρ the density of the water. In addition, the runup is influenced by bottom roughness, contact line dynamics at the moving shoreline (dependent on chemical properties of beach, air, and water) and smaller, but observable, effects such as a tiny deformation of the beach due to the wave load.

If we ignore effects of viscosity, surface tension, and geometrical imperfection R will be independent also of ℓ since the solitary wave has permanent form. Then dimension analysis readily shows that R/A is a function of θ and A/d, only. Synolakis[8] combined a linear treatment of an incident solitary wave with a nonlinear shallow water theory, subjected to the hodograph transformation, on the beach. Assuming short waves relative to the beach length he then obtained the celebrated asymptotic solution for the runup height R

$$\frac{R}{A} \to 2.831(\cot\theta)^{\frac{1}{2}} \left(\frac{A}{d}\right)^{\frac{1}{4}} \quad \text{for} \quad \left(\frac{A}{d}\right)^{\frac{1}{2}} \cot\theta \to \infty. \tag{1}$$

The reference also reported a criterion for breaking during runup,

$$\frac{A}{d} \geq 0.818(\tan\theta)^{\frac{10}{9}}. \tag{2}$$

For high, and thereby short, incident solitary waves dispersion during shoaling is important and (2) becomes inadequate. Based on simulations with a boundary integral technique and curve fitting Grilli *et al.*[25] reported

$$\frac{A}{d} \geq C(\tan\theta)^2, \tag{3}$$

as a criterion for breaking during runup. They recognized one breaking regime ($C = 16.9$) where very steep fronts were formed and propagated some way up-beach and another ($C = 25.7$) where clear overturning occurred. We employ the stricter (smaller C) criterion only. For large θ this criterion is much more relaxed than (2). For $\theta = 10^\circ$ (2) and (3) yield $A/d \geq 0.52$ and $A/d \geq 0.12$, respectively. For smaller θ the difference is less pronounced. Our experiments are consistent with (3) and do not display any sign of breaking for amplitudes up to 0.388 and no certain signs for $A/d = 0.481$.

On steep beaches, the formula (1) overestimates R for large amplitudes, while it underestimates R for small amplitudes.[24] Hence, we employ two dispersive, but inviscid, numerical models for wave propagation and runup on sloping beaches. Both models are carefully tested, see for instance the benchmark simulations in Pedersen.[33] The first model is based on Boussinesq equations that are fully nonlinear, but are used only with standard dispersion properties.[12,33] We also employ a boundary integral model (BIM) for full potential theory.[46] It is related to the higher order technique of Cooker *et al.*[47] and Dold.[48] However, while these references employ high order polynomials for interpolation along the contour we use cubic splines. This makes inclusion of boundary conditions simpler and does allow for the inclusion of a moving shoreline in particular. At the shoreline we assume analyticity which in principle excludes cases with contact angles larger than 90°. Boundary integral methods are generally not well suited for the computation of very thin swash tongues that evolve during runup/withdrawal of higher waves. The proximity of the surface and the bottom parts of the contour requires a smaller time step relative to the grid spacing and a more accurate numerical integration than in deeper water. Hence, series of runs are performed with nonuniform adaptation of both spatial and temporal resolution as well as different order (up to 14th) Gaussian integration. Generally, a value for maximum runup is thus only accepted if a systematic refinement sequence of at least three resolutions produces coincident runup heights within 0.1%. The resolutions varied in time and space, but for $A/d \sim 0.3$ the finest grid increments were typically $0.025\,d$. There is one exception to this rule, namely the runup height for $A/d = 0.39$ given later in Table II. For this case the contact angle at the shoreline just surpasses $\frac{\pi}{2}$ meaning that the acceleration at the shoreline becomes intermittently infinite in the inviscid description. In addition, the swash zone becomes extremely thin. For this case we observe marked non-monotonous behaviour of R/A with resolution and variation within 2%.

For both models an incident wave is specified as a solitary wave that is an exact solution[12,49] of the equations solved in that particular model. Accordingly, both surface elevations and velocities are employed as initial conditions. In the simulations we adapt the amplitude and phase of the incident wave to the time series of the deep water acoustic gauge at $x = x_m = -2.045$ m. We average three experiments and use regression analysis (cubic polynomials, 29 points) to extract the time (t_m) and wave height (A) at the maximum elevation. At t_m no appreciable reflection has reached the deep water gauge position and A may be used as the height of the incident solitary wave in the numerical models. A definition sketch of the tank and wave gauge and a comparison between the measured time series and the computed ones are presented in Figure 3. The time t_m is more sensitive to experimental errors than A. To check the accuracy the mean square deviation between the measured and the theoretical surface has been computed, assuming a crest peak at $t_s = t_m + \Delta t_m$. The t_s with the minimum mean square deviation is then an alternative time for the passage of the crest at $x = x_m$. For $A/d = 0.0977$ we find $|\Delta t_m| < 0.005$ s, while it is generally smaller for higher amplitudes. Hence, the time t_m, without the correction Δt_m, is used to synchronize the solutions with the experiments. The initial peak is located at $x = x_0$, which is at least one half-wavelength $\lambda(\epsilon) = -d\ln(\frac{1}{4}\epsilon)/\sqrt{3A/d}$ from the start of the bottom slope. The parameter ϵ, which is set to 5×10^{-4} in our simulations, corresponds to the ratio of the surface elevation to A at a distance λ from the wave peak. The distance from the initial peak to toe of the beach is used again for the distance between the peak and the offshore boundary, which is simply a vertical wall. This yields a total computational domain somewhat longer than λ

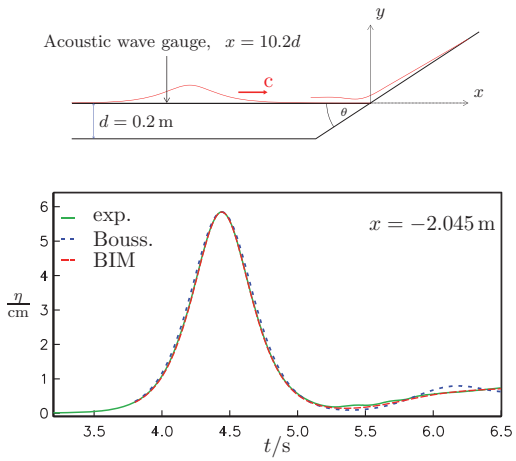

FIG. 3. Upper panel: Definition sketch of wave tank and deep water acoustic gauge. The vertical scale is exaggerated in the sketch. Lower panel: Elevation time series from experiments (exp.), Boussinesq model (Bouss.) and full potential theory (BIM). The model times series start at a finite elevation because the initial conditions in the model are partly situated in front of the gauge location.

plus the length of the beach. Since the incident waves are perfect solutions of the equations, and the resolutions are fine, the initial conditions will yield no noticeable waves in the offshore direction and no sponge layer or radiation condition is needed.

Simulated swash zones, at the time of maximum runup, are shown in Figure 2. We observe that the higher amplitude represented, $A/d = 0.292$, yields a much smaller flow depth in the swash zone than the smaller amplitude $A/d = 0.098$. The contact angles at the shoreline (angle between free surface and inclined plane), at maximum runup, are $\psi = 0.68^\circ$ and $\psi = 3.4^\circ$, respectively, for the two cases shown.

The boundary integral method will be most used, since it is the more general of the two. The Boussinesq model will be used in Sec. III. While it is interesting to see how well the Boussinesq model may perform, its main purpose is to give evidence for the validity of the implementation of the BIM model.

C. Boundary layer equations

A viscous boundary layer on the beach is apparent in videos and PIV measurements from our experiments. In this boundary layer we introduce a (s, z)-coordinate system with the s-axis defined positive upwards along the beach and the z-axis orthogonal to the beach (see Figure 12). We put $s = 0$ at the equilibrium shoreline on the beach. The s component of the velocity outside the boundary layer, $U(s, z, t)$, is supposed known, either from observations or numerical simulations. According to our experiments, as well as the potential flow simulations, the z variation of U is very weak in the swash flow. Moreover, according to Table I the Reynold numbers in the swash is of order 10^5, or

TABLE I. Reynold numbers for solitary waves with $d = 0.2\,\mathrm{m}$ and $\theta = 10^\circ$.

A/d	0.1	0.2	0.3	0.4	0.5
Re_c (constant depth)	2.0×10^4	5.8×10^4	1.1×10^5	1.6×10^5	2.3×10^5
Re_R (runup)	3.8×10^5	1.4×10^6	3.0×10^6	5.1×10^6	7.7×10^6

larger. Hence, the flow may be governed by the boundary layer equations. For time dependent flow with an external pressure gradient the momentum equation may thus be written

$$\frac{\partial u}{\partial t} + u\frac{\partial u}{\partial s} + w\frac{\partial u}{\partial z} = \left[\frac{\partial U}{\partial t} + U\frac{\partial U}{\partial s}\right]_{z=0} + \nu\frac{\partial^2 u}{\partial z^2}, \tag{4}$$

where u and w are the velocity components s and z directions, respectively, and the terms within the bracket correspond to the pressure gradient which is assumed equal to that of the outer flow. The continuity equation is

$$\frac{\partial u}{\partial s} + \frac{\partial w}{\partial z} = 0. \tag{5}$$

The boundary conditions are

$$u(s, 0, t) = w(s, 0, t) = 0 \tag{6}$$

and u must match U at the outer edge of the boundary layer.

In numerical solutions of the boundary value problem, as stated above, the outer velocity U is extracted (as a function of s and t) from the Boussinesq, or the potential flow model. This U is then imposed on the Eqs. (4) through (6) through the forcing term. The momentum equation (4) is discretized by the Crank-Nicholson method for the linear part and a combination of upstream differences and a backward time step for the nonlinear terms. Exact reproduction of the outer flow in the momentum equation is obtained through the design of the forcing term. The grid is uniform in s, but non-uniform in z, with finer resolution close to the beach. Grid rows are included or excluded from the computational domain according to the moving shoreline. The technique is validated through comparison with simple analytic solutions and grid-refinement studies. More details are found in Lindstrøm.[46] In the vicinity of the moving shoreline the boundary layer description becomes invalid for two reasons. First there is a singularity in the solution itself for $t = t_s$, where t_s is the arrival time of the shoreline at position s, similar to the singularity in the Blasius solution at the front of the plate. Second, there are special flow features close to the moving shoreline due to contact line dynamics.

Linearization and detailed solution of the boundary value problem (4) through (6) are discussed in the Appendix. Closed form solutions are there presented for outer flows specified as polynomials of time.

D. Stability of boundary layer flow

Boundary layers at a flat plate in a uniform current (Blasius profiles) become unstable when the Reynolds number $Re_B = UL/\nu \approx 5 \times 10^4$, where U is the constant free-stream velocity and L is the distance from leading edge.[50] When Re_B is increased to around 3×10^6 the flow becomes fully turbulent. Other stationary boundary layers become more readily unstable when the outer flow is retarded (unfavourable pressure gradient) and may be stable at higher Reynolds numbers for accelerated flow (favourable pressure gradient).

For the transient flow of a solitary wave on constant depth, or running up a beach, it is convenient to identify L as the total particle displacement in the outer flow, whereas the maximum velocity is used for U. This leads to

$$\text{Constant depth } U = \frac{A}{d}\sqrt{gd},\ L = \frac{4}{\sqrt{3}}A\frac{A}{d},\ Re_c = \frac{4}{\sqrt{3}}\left(\frac{A}{d}\right)^{\frac{3}{2}}\frac{\sqrt{gd}d}{\nu},$$

$$\text{Runup} \qquad U = \sqrt{gR},\quad L = \frac{R}{\sin\theta},\quad Re_R = \left(\frac{R}{A}\right)^{\frac{3}{2}}\frac{(\frac{A}{d})^{\frac{3}{2}}}{\sin\theta}\frac{\sqrt{gd}d}{\nu},$$

where R is given by Synolakis' formula (1). The velocity scale for the runup is linked to the free fall velocity from R in the gravity field. This provides a good estimate for the maximum velocity which is attained in the early stages of runup. In their investigation of boundary layers under solitary waves at constant depth Sumer *et al.*[40] employed a L which is half the particle displacement. In terms of the above definitions they found that generation of vortex tubes in the retardation

TABLE II. Maximum runup height to amplitude (R/A). Exp., BIM, and Bouss. correspond to the experiments and the two models, respectively.

	R/A for $\theta = 10^\circ$			
A/d	Expt.	BIM	Bouss.	(1)
0.098	3.10±0.03	3.69	3.67	3.92
0.195	3.37±0.03	4.04	4.00	4.61[a]
0.292	3.46±0.02	4.25	4.19	5.07[a]
0.388	3.52±0.03	4.44[b]	4.44[b]	5.43[a]
0.481	3.55±0.04	...	...	...

[a]Values belong to combinations of models and amplitudes that formally yield wave breaking, but which are included for completeness.

[b]For the highest amplitude the BIM model experiences a maximum contact angle larger than $\frac{1}{2}\pi$, indicating that the formal validity the solution is debatable and that the agreement with the Boussinesq result is partly coincidental.

phase of the outer flow first occurred at $Re_c \gtrsim 4 \times 10^5$. As the Reynolds number was increased the instability occurred earlier in the flow evolution, then pressure spikes were observed and for $Re_c \gtrsim 10^6$ the reference claims that transition to turbulence takes place. In their numerical work Vittori and Blondeaux[39] employed a different definition of the Reynolds number. However, according to the discussion in Sumer *et al.*[40] the numerical results do agree with the experiments in this reference when the numbers are converted.

Assuming a wave tank of depth $d = 0.2$ m, as is employed in our experiments, and $\theta = 10^\circ$, we obtain the values of Table I. First we observe that the boundary layers at constant depth are within the laminar regime as identified by Sumer *et al.*[40] The measurements of Liu *et al.*[38] were performed with $d = 0.1$ m, which reduce Re_c, relative to values in the table, and bring them further into the laminar regime. The outer flow in the runup is similar to that of constant depth propagation, with an initial phase of acceleration, followed by retardation, even though the acceleration phase is relatively shorter and the retardation phase longer for the runup. A comparison with the critical numbers of Sumer *et al.*[40] then indicates that the lowest amplitude, $A/d = 0.1$, may give a laminar flow, while the higher is in the transition regime. This is consistent with our observations. For $A/d = 0.0977$ no sign of irregular flow is observed, while for $A/d = 0.292$ the flow was disturbed at the upper field of view (FOV) (see Figure 2). It must be noted that only the lowest FOV was employed for $A/d = 0.0977$ and $A/d = 0.195$ due to their short inundation length and that mild undulations may be hard to detect due to limitations on the resolution and sparse particle seeding. More details are given in Sec. IV A.

III. MEASURED AND COMPUTED RUNUP HEIGHTS

As seen from Table II the maximum runup heights from the dispersive models are very similar, while the shallow water formula (1) yields higher runup due to the excess steepening of the incident wave during shoaling.[24] On the other hand, the measured runup heights are significantly smaller than the theoretical ones. The relative deviation increases with the amplitude of the incident wave.

The two models employed are well tested and it is highly unlikely that they over-predict runup by the same amount in unison due to errors. In Figure 4 we have compared our measurements to those of Hall and Watts[7] for the same slope angle (10°). There is quite some scatter in the data from Hall and Watts, but our data fit in rather well. Hall and Watts employed depths (d) from 0.15 m to 0.68 m. Unfortunately, the scatter is too strong to reveal any systematic dependence on d. In Figure 5 we have compared Boussinesq and BIM simulations to experimental data from Langsholt[51] for $\theta = 12^\circ$. According to (3) all waves in the figure are non-breaking. We observe similar theoretical over-predictions as in Table II. Moreover, even though there is some scatter also in the data from Langsholt there is an apparent tendency that R/d for a given A/d increases with the depth d. This suggests that viscous or capillary effects are significant in this kind of laboratory experiments.

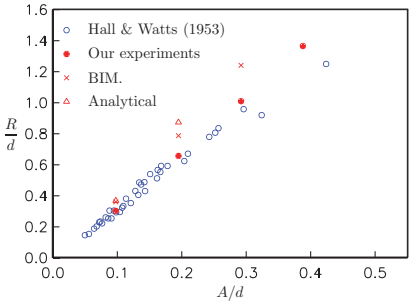

FIG. 4. Runup data for $\theta = 10^\circ$.

Applying their boundary integral model for $\theta = 15^\circ$ Svendsen and Grilli[9] over-predicted the runup height by roughly 10% in comparison to the Hall and Watts.[7] For $\theta = 45^\circ, 70^\circ$ they obtained, on the other hand, good agreement with experiments.

Among other things Li and Raichlen[11] reported experiments on solitary wave runup on a beach with inclination $\theta = 3.8^\circ$. With this gentler inclination most of the waves are breaking in finite depth, which sets this data-set apart from those discussed above. Still a tendency for increasing *R*/*d* with *d*, for the same *A*/*d* is noteworthy. As an exception Jensen *et al.*[12] did find close agreement between experimental and theoretical runup for *A*/*d* close to 0.1 and $\theta = 10.54^\circ$. For higher amplitudes they observed a mild reduction of *R*/*A* with increasing *A*/*d*. However, there is a bias in the data for maximum runup in this reference (but not in the velocity data) that is linked to the material properties of the beach that led to a slight water absorption followed by deformation.

Comparison with the experiments of Hall and Watts[7] indicates that the experimental runup heights in Table II are reasonably accurate, at least. Thus, we must seek the cause for the deviation between theory and experiments among physical effects that are significant in the experiments, but absent in the theories. In the literature this issue has been addressed on a few occasions outlined below.

Pedersen and Gjevik[52] found that theory overestimates experimental runup,[7,51] even though the difference was strongly diminished when θ became larger than 20°, say. The authors attributed this behaviour to the presence of boundary layers, which they presumed to be turbulent.

In his key work on solitary wave runup Synolakis[8] emphasized that the increase in *R*/*d* with *A*/*d* is significantly smaller for breaking than for non-breaking waves. This then led him to suggest that the discrepancy reported in Pedersen and Gjevik[52] was due to unrecognized wave breaking in the experiments. However, in view of the experiments, the criterion (3) and our simulations this possibility can be ruled out because breaking during runup does not occur for amplitudes in the range investigated.

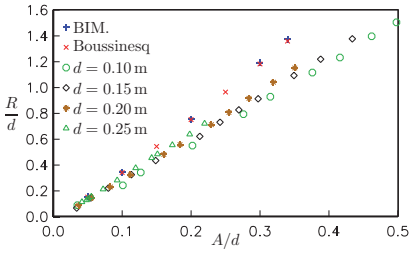

FIG. 5. Runup data for $\theta = 12^\circ$ from Langsholt.[51]

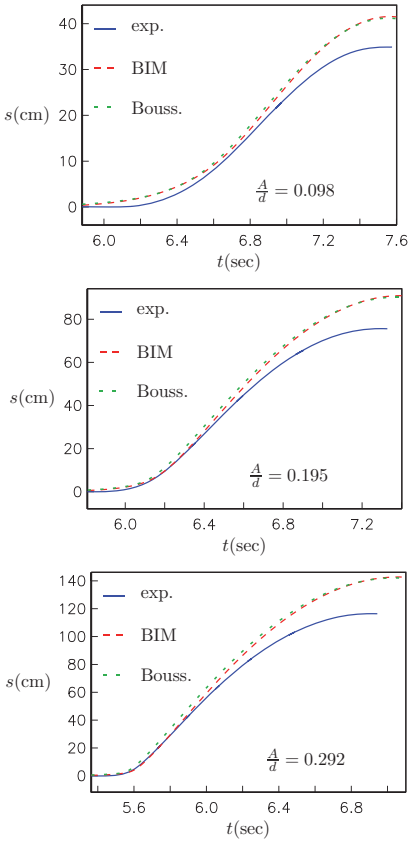

FIG. 6. The shoreline excursion as function of time. The runup height is then $s(t)\sin\theta$, where θ is the beach inclination.

For $\theta = 10^\circ$ Li and Raichlen[11] compared the experiments of Hall and Watts[7] to hydrostatic nonlinear simulations. In an intermediate amplitude range ($A/d \sim 0.1$–0.2) their numerical values over-predicted the runup. However, the relative deviation did not increase for higher amplitudes, in contrast to what we observed for our BIM and Boussinesq models. One reason is, presumably, that breaking in the hydrostatic approximation occurs already for A/d slightly above 0.1 according to (2). Hence, for the higher amplitudes there was a noticeable unphysical breaking in the simulations of Li and Raichlen[11] which affected the runup and reduced the deviation from the experiments.

Measurements are often focused on the maximum runup height. However, in the present investigation also the time history of the shoreline motion has been measured by edge detection applied to video recordings from above, as explained in Sec. II A. The horizontal location of the shoreline is then found as function of time and compared to the corresponding computed shoreline positions, from the BIM and the Boussinesq models, in Figure 6. For the lowest amplitude $A/d = 0.0977$ the experimental inundation lags significantly behind in the early stages, then nearly catches up with the theory and then steadily falls behind again until maximum runup. The higher amplitudes yield similar evolution of the discrepancies, except that the early delay in the experiments are reduced in relative size and duration. Naturally, the initial inhibition of the inundation is due to capillary effects. The shoreline remains at rest until the contact angle surpasses the advancing angle. An image of the

FIG. 7. Image showing part of the shoreline before start of runup, with water to the right. The front of the wave has reached the shoreline, but it has not yet been set it into motion.

shoreline before it is mobilized is shown in Figure 7. This induces extra steepness of the wave front which then causes larger acceleration that to some extent counterbalances the delay relative to the simulations. As expected, the relative importance of this effect is smaller for the higher amplitudes for which the critical contact angle is reached sooner and for a smaller front height to amplitude ratio.

Even though the detailed characteristics of the contact angle dynamics during runup is not unraveled, it seems likely that the eventual deviation between theory and experiments is also due to viscous effects. In fact, our results will indicate that viscous effects are important and may well be the major reason for the discrepancy. In particular, in view of the thin swash tongues in Figure 2 bottom boundary layers are likely to be much more important on the beach than in a depth of 20 cm say, where surface film effects presumably produce more damping than boundary layers.[3,4] Hence, further issues concerning the contact line dynamics and capillary effects are left for future work and the remainder of this article is devoted to bottom boundary layers.

IV. BOUNDARY LAYERS

A. The computed and observed boundary layers

The problem given by (4) through (6), with the outer flow taken from the BIM solution, is solved numerically. For times somewhat before maximum runup, velocity profiles in the swash zone are displayed in the two upper panels of Figure 8. The surface appears as a steep, almost straight line due to the aspect ratio. The profiles are drawn at those s-positions where the zero velocity lines normal to the s-axis are indicated. Only the wetted parts, which are below the intersections of the free surface and the zero velocity lines, have significance. At the surface the velocity should be very close to the outer value. Otherwise the boundary layer would extend the flow depth and the concept of outer and inner flow would be wrong. This is the case in the vicinity of the moving shoreline only, where the flow presumably is also affected by the contact point dynamics which is not included in our description. We observe that withdrawal first occur in the boundary layer. Moreover, we observe that the difference between linear and nonlinear boundary layer theory is largest around the reversal of the outer flow. Close to the moving shoreline nonlinear theory yields a markedly thicker boundary layer and a milder shear. The lower panel of Figure 8 corresponds to a later stage where the fluid is retreating everywhere in the swash zone. It is noteworthy that the effect of the nonlinearity in the boundary layer has nearly vanished.

Computed and measured boundary layer profiles for a position $s = 7$ cm (see Figure 2) are compared in Figure 9. There are marked delays of approximately 0.05 s and 0.02 s, for A/d equal to 0.0977 and 0.292, respectively, in the measured free flow velocity as compared to theory. When these delays are adjusted the profiles agree very well, in particular for $A/d = 0.292$. For the first part of the evolution there is a further delay of the experimental outer flow, presumably linked to the deviation in the shoreline motion shown in Figure 6. We also emphasize that the first phase of the evolution of the boundary layer, after the passage of the moving shoreline, is not accurately described by the boundary layer theory. The delay of 0.02 s for $A/d = 0.292$ may be comparable in magnitude, but is still somewhat large in comparison to a sum of all errors in wave travel time pointed out in the

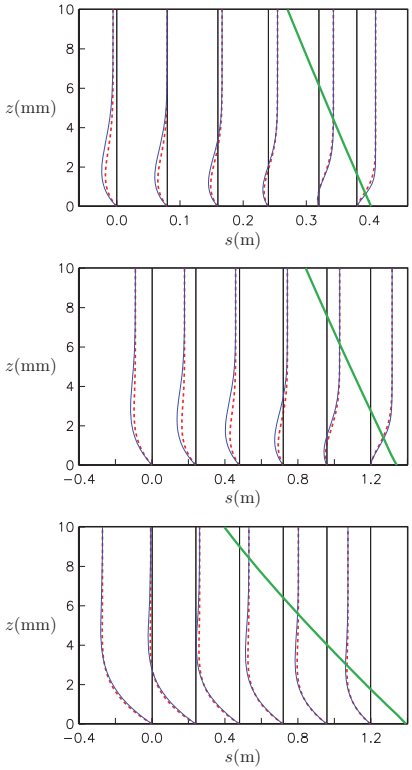

FIG. 8. Boundary layers in the runup, with outer flow from full potential theory. The lines normal to the s axis show profile locations, while nonlinear and linear profiles are dashed and solid, respectively. Also the free surface is depicted as a bold solid line. Upper panel: $A/d = 0.0985$, $t = 7.40$ s. 1 m on the s-axis corresponds to 5.84 m/s. Lower panels: $A/d = 0.295$, 1 m on the s-axis corresponds to 3.89 m/s. The two lower panels correspond to $t = 6.70$ s and $t = 7.30$ s, respectively.

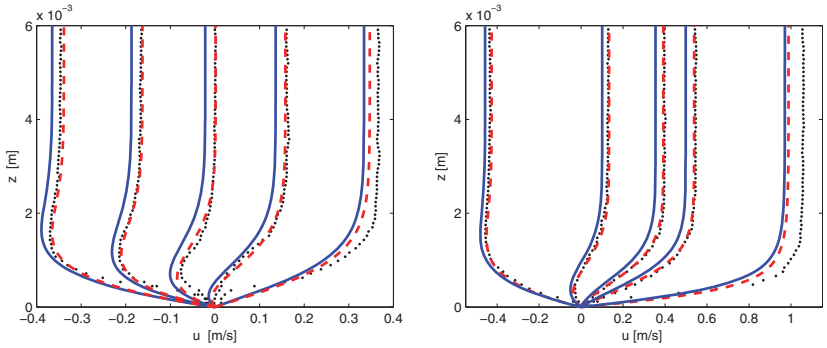

FIG. 9. Measured (dots) and simulated (fully drawn lines) velocity profiles in the boundary layer. Dashes correspond to time simulated profiles with time shifts 0.05 s and 0.02 s, respectively, in the left and right panels. The measurement is made 7 cm in-land and the PIV data are averaged over a distance of approximately 0.5 cm along the beach. Left panel: $A/d = 0.0977$ for times 6.90 s, 7.20 s, 7.40 s, 7.60 s, and 7.80 s. Right panel: $A/d = 0.292$ for times 5.70 s, 6.00 s, 6.10 s, 6.30 s, and 6.80 s.

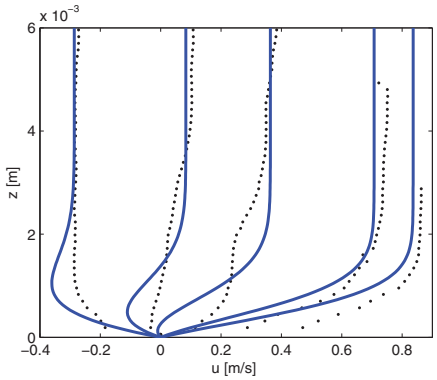

FIG. 10. Measured (dots) and simulated (BIM, fully drawn lines) velocity profiles in the boundary layer in the upper field of view for $A/d = 0.292$ and times 6.34 s, 6.40 s, 6.58 s, 6.75 s, and 7.00 s.

Secs. II A and II B. However, the delay of 0.05 s for $A/d = 0.0977$ is clearly beyond the identified errors and is still unexplained. It is noteworthy that no sign of separation or eddy formation is apparent in these profiles. Moreover, the observed agreement shows that the boundary layer theory becomes valid some distance from the moving shoreline, even though it is not applicable at the shoreline itself. The results for $A/d = 0.195$ (not shown) are similar to those of $A/d = 0.292$.

For the amplitudes $A/d = 0.388$ and $A/d = 0.481$ we have not compared profiles with theory. The lowest of these two amplitudes gives laminar boundary layers. On the other hand, the largest display signs of instability, without strict repeatability, when PIV is applied in the middle of the tank, but not when PIV is applied closer to the side-walls (see Sec. II A for transverse variation of beach geometry). Hence, $A/d = 0.481$ may presumably be close to the transitional regime in the lower part of the runup.

The higher onshore field of view (see Figure 2) is reached only by the amplitude $A/d = 0.292$ and higher. Close to the beach, in particular, the measurements are of lower quality here than in the lower field of view, mainly due to the poorer particle density. In the video recording there are clear signs of instabilities in the boundary layer. For 3 out of 4 repetitions the instabilities occur after $t = 6.4$ s, while one run also displays irregularities immediately after the arrival of the fluid. The reason for this is not known, but since we are in the transitional regime small imperfections in the reproduction of the individual experiments may lead to marked deviations. As shown in Figure 10 for one of the three similar runs there is a fair qualitative agreement between theory and experiments for $t = 6.34$ s, save for the 1 mm closest to the beach, then the profiles consistently deviates. It is difficult to pinpoint the transition time accurately, but it appears to be close to $t = 6.40$ s. It is noteworthy that the instability occurs around the time the theoretical profiles display an inflection point which allow possible instability according to the famous criteria of Rayleigh and Fjørtoft for stationary inviscid flow. However, also the profiles in lower FOV, depicted in Figure 9, display corresponding inflection points. Inflection points are also present in profiles for the retarding part of the flow induced by a solitary wave on constant depth, without causing instabilities for the lower Reynold numbers.[38,40] Hence, the instability indicated in Figure 10 cannot be linked to the presence of the inflection point alone.

The transition around $t = 6.40$ s is confirmed by graphs of averaged (30 subsequent velocities, corresponding to a duration of 0.01 s) instantaneous streamlines based on the PIV velocity fields. For $t < 6.4$ s there are no signs of irregularities, then the streamlines starts to undulate. Undulations are seen to develop within the field of view and are also seen to be transported in through its upstream boundary. At $t = 6.7$ s, which is 0.1 s before the outer flow is reversed, eddies are formed within the FOV and transported gently outwards. After reversion eddies and undulations disappear from the

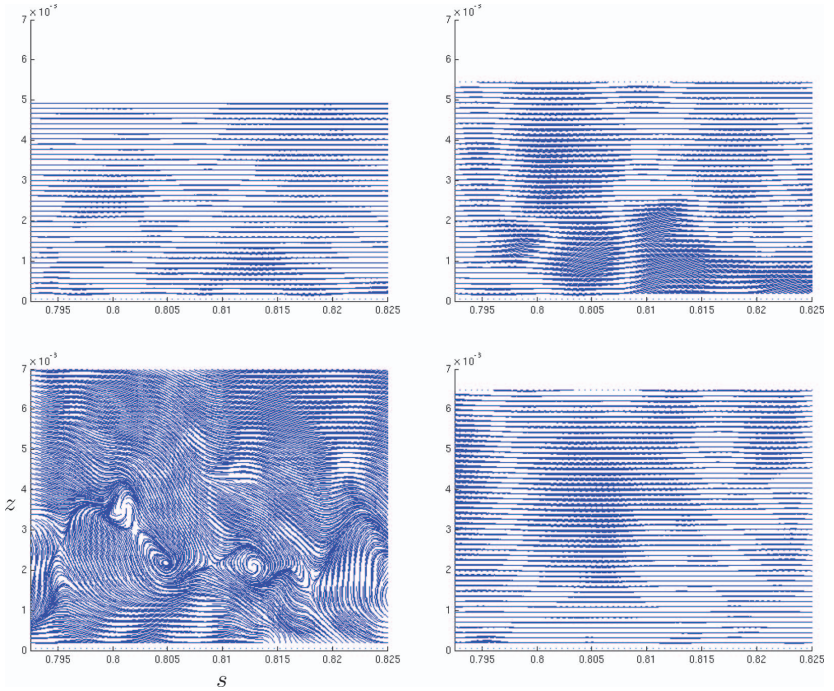

FIG. 11. Instantaneous streamlines based on PIV velocities approximately 0.8 m from the equilibrium shoreline. Upper left, upper right, lower left, and lower right panels correspond to $t = 6.40$ s, $t = 6.43$ s, $t = 6.75$ s, and $t = 7.11$ s, respectively. The units on the s and z axes are m and mm, respectively.

boundary layer and the streamline pattern again consists of lines parallel to the beach. One stable pattern during runup, one slightly wavy pattern, one unstable pattern close to flow reversal, and one pattern during the down-rush are shown in Figure 11. The higher amplitudes display similar instabilities in the upper field of view (results not shown).

B. Analytic boundary layer solutions

According to the experiments the boundary layer for the lowest amplitude remains laminar. Moreover, the numerical solutions indicate that this case is described reasonably well with linear theory. In this situation, approximate analytic solutions can be found. Such solutions are very useful since they can readily be used to display main features of the boundary layer flow.

To obtain a closed form solution an idealized model example is considered. The example is inspired by the thin-swash limit described in several references,[12,53,54] but is further simplified in the sense that the outer flow is a uniform plug flow retarded by gravity (see Figure 12). In this case the outer flow is a linear function in time and given as

$$U(x, 0, t) = U_0 - g \sin\theta t. \tag{7}$$

The solution for u, defined for $0 < s < U_0 t - \frac{1}{2} g t^2$, reads (see Subsection 2 of the Appendix)

$$u(s, z, t) = \frac{U_0 \zeta^2}{2} + \left[U - \frac{U_0 \zeta^2}{2} \right] \operatorname{erf}\left(\frac{\zeta}{2\sqrt{T}} \right) - U_0 \zeta \sqrt{\left(\frac{T}{\pi} \right)} \exp\left(-\frac{\zeta^2}{4T} \right), \tag{8}$$

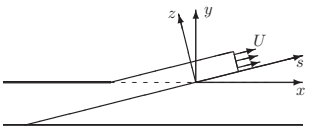

FIG. 12. A uniform plug retarded by gravity. The shape of the fluid body is irrelevant as long as the boundary layer is thinner than the flow depth.

where $T = g\sin\theta U_0^{-1}t - 1 + \sqrt{1 - 2sg\sin\theta U_0^{-2}}$ and $\zeta = \sqrt{g\sin\theta/\nu U_0}z$. The former is the time elapsed since the fluid reached position s, non-dimensionalized. For the normal velocity we obtain

$$w(s,z,t) = -\sqrt{\frac{\nu g\sin\theta}{\pi U_0 T}}\left[1 - \exp\left(-\frac{\zeta^2}{4T}\right)\right]. \tag{9}$$

We observe that there is an entrainment velocity at the outer edge of the boundary layer. A corresponding entrainment is observed in the numerical boundary layer solutions discussed subsequently.

Velocity profiles based on the solutions given above are shown in Figure 13. The graphs are given in physical dimensions using $U_0 = 1$ m/s and $\theta = 10^\circ$ giving a total runup-time of approximately 0.587 s and a total runup-length of approximately 0.294 m, the working fluid being water. We observe that the flow in the boundary layer reverses before the outer flow and thus starts to drain the runup wave. The draining sinks fluid from the outer region into the boundary layer giving the entrainment velocity displayed in Figure 14. Such draining effects on the outer flow are expected to cause reduced runup heights, particularly for thin, wedge shaped wave fronts (see Figure 2).

C. Estimation of reduced runup height due to the boundary layer

To relate the boundary layer quantitatively to a reduction in the runup height the feedback from the boundary layer on the outer flow must be assessed. One strategy is to incorporate a term representing volume flux loss in the boundary layer (see below) in an depth integrated continuity equation, as is done in Liu and Orfila[55] for a linear boundary layer in finite depth. However, herein we need to address also nonlinear boundary layers and, more significantly, the combination of an incorporated boundary layer and a moving shoreline is far from straightforward. At present there is neither any theory nor any observation describing the behaviour of such a combination. Instead we

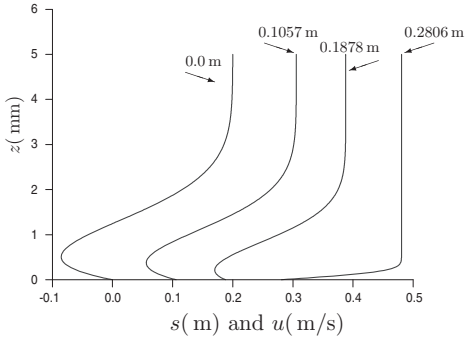

FIG. 13. Velocity profiles at $t = 0.4696$ s across the viscous boundary layer at various s-positions (i.e., τ_ξ values) along the beach as indicated on the abscissa. The runup-plug enters the beach with velocity $U_0 = 1$ m/s and the total runup-time is 0.5870s in this case, giving the runup-length 0.2935 m. It is remarked that the profiles are shifted to their s locations and that the velocity is zero at $z = 0$ for all profiles.

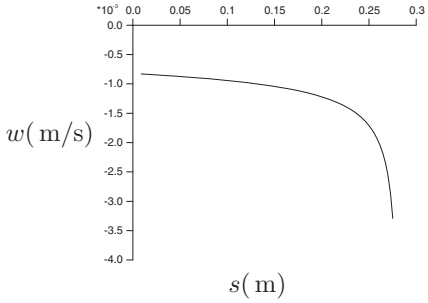

FIG. 14. Entrainment velocity profile $w = \sqrt{\frac{\nu g \sin\theta}{U_0}}\, w_0^{(i)}(\zeta = 5, \tau = 0.8; \tau_\xi(s))$ along the outer edge of the viscous boundary layer.

will estimate the effect of the boundary layer on runup through integrated effects on a finite volume adjacent to the moving shoreline. The boundary layer causes a volume transport deficiency given as

$$\Delta q = \int_0^\infty (U - u) dz.$$

If the boundary layer had been stationary $\Delta q/U$ would equal the displacement thickness.

A crude estimate of the reduction of runup height for $A/d = 0.098$ is obtained using the solution (8). We regard a front section, with a length l being much less than the total inundation length, of a slab. The loss (caused by viscosity) of fluid volume (per unit width) transported into this section during runup is given by

$$Q_a = \int_{t=T_0}^{t_{top}} \Delta q(s_f(t) - l, t) dt, \tag{10}$$

where s_f is the instantaneous position of the slab front, that passes position $s = 0$ (equilibrium level) at time $t = 0$, position $s = l$ at $t = T_0$, and is in the top position at $t = t_{top}$. The volume (per unit width) Q_w of a fluid wedge of length l is

$$Q_w = \frac{1}{2} l^2 \tan\psi, \tag{11}$$

where ψ is the wedge angle, which, according to outer numerical solution, is $\psi = 3.4^\circ$ (see the end of Sec. II B). l is iteratively adjusted until $Q_a \approx Q_w$, meaning that the final l is an estimate of the reduction of the inundation length due to the viscous boundary layer. Setting $U_0 = 1$ m/s, we get $l \approx 5.7$ cm (approximately as observed, see Table II), and with $U_0 = 1.2$ m/s, we get $l \approx 6.9$ cm. The initial velocity $U_0 = 1.0$ m/s gives a slab runup length ≈ 0.29 m, and with $U_0 = 1.2$ m/s, we get a slab runup length of 0.42 m. The last one is approximately equal to what the numerical inviscid calculations give, but an inundation reduction of 6.9 cm is a little too large (see Table II). The velocity profiles displayed in Figure 8, indicate that this overestimation might be attributed to the linearization of the boundary layer equations. A related, but slightly modified, procedure is applied to the numerical solutions below.

We consider a fluid wedge corresponding to the Lagrangian coordinate interval $b \le a \le 0$. This means that this fluid volume initially ($t = 0$) stretches from a distance b, off shore, to the shoreline. Such a wedge is moved onshore and deformed during runup as depicted in Figure 15. At maximum runup the lower end of wedge in the potential flow solutions corresponds to the observed maximum runup. For this volume the normalized accumulated volume loss becomes

$$V_d = \frac{\int_0^t \Delta q(x(b, t), t) dt}{\frac{1}{2} \tan\theta b^2}.$$

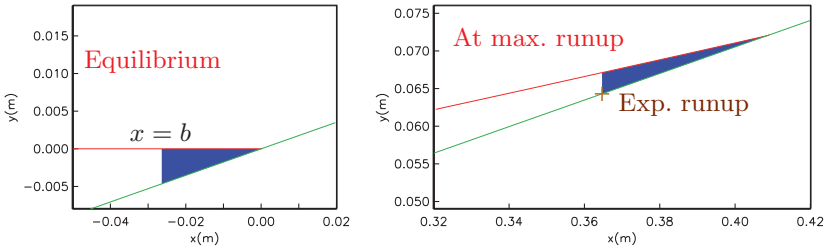

FIG. 15. The wedge-shaped fluid body that surpasses observed inundation. Left panel shows the volume at equilibrium, while the right panel shows the volume at the time, according to the Boussinesq model, at maximum runup. The experimental position for maximum inundation is marked by + in the right panel. The case $A/d = 0.098$ has been used for illustration.

The denominator corresponds to the volume of the wedge. If V_d becomes comparable to unity during runup it is indicated that the reduced runup heights in the experiments may be due to viscous effects. The computation of V_d does not take into account the feedback from the boundary layer to the outer flow. In the later stages of runup, in particular, this will be an significant source of error. Presumably, our V_d overestimates the volume transport losses in relation to values from experiments or fully viscid solutions. Hence, only the order of magnitude of V_d should be considered.

Corresponding considerations based on integrated drag and dissipation have been made and are found to be consistent with the volume loss in relation to the reduced runup height. However, while V_d is based on the computation of the boundary value properties only at a finite distance from the moving shoreline, integrated dissipation or drag will comprise substantial contributions from the very vicinity of the shoreline, where the boundary layer theory is incorrect.

In Figure 16 the integrated volume transport defects have been depicted. For all amplitudes V_d surpasses unity well before the maximum runup is reached in the simulation.

The integrated effects of the boundary layer are estimates only, but their orders of magnitude are consistent with the deviations between theory and experiments. This indicates that laminar viscous effects give a main, and maybe dominant, contribution to this deviation.

V. DISCUSSION

Runup heights from recently performed experiments are substantially smaller than predictions from numerical models based on inviscid theory. Comparison with laboratory investigations from the literature shows that this feature is typical for standard wave tank experiments with depths around 0.2 m. Since also different theoretical models are employed, with similar results, it then follows that important physics is not retained in the models. An investigation of high speed video images rules out the possibility of unrecognized wave breaking, but shows the presence of boundary layers at

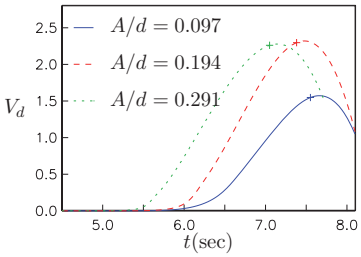

FIG. 16. Normalized volume transport defect computed from simulated velocity profiles in the boundary layer.

the beach. For small amplitudes the boundary layers are laminar, such as those found under solitary waves on constant depth by Liu *et al.*[38] In analogy with their observation of a reverse boundary layer flow in the retardation phase, we find that the first fluid withdrawal on the beach occurs in the boundary layer. For higher amplitudes instability is observed in the boundary layers for Reynolds numbers of the same order as the transitional numbers reported for solitary waves in constant depth.[40] We do not have a full coverage of the swash zone by video and PIV measurements, but the results indicate that instabilities occur more readily up-beach than close to the equilibrium shoreline and that the first part of the evolution of the boundary layer is laminar for all investigated waves and locations.

The early reversal of the flow in the boundary layers is retrieved in idealized and numerical boundary layer solutions. For laminar boundary layers good agreement is also observed between measured and computed velocity profiles. Moreover, the integrated mass flux reduction caused by the boundary layers is quantitatively reconcilable with the difference in runup height between models and experiments. The other relevant effects, surface tension and contact line dynamics, have been observed only indirectly through the initial inhibition of the inundation. We may thus not present a conclusion as to which effects are the dominant ones. Still, our findings suggest that laminar bed friction is important in the runup experiments and may be a main reason for the over-prediction of runup by inviscid models.

Presumably, surface tension and boundary layer effects cause small scale experiments to be scale dependent in a manner that is quite different from large scale cases with turbulence. This reduces the value of detailed comparison of experiments with full scale tsunamis, or models for such. In particular, any notion that a tsunami model should be able to reproduce a simple experiment very accurately to have good prospects for the more demanding real applications is wrong. Instead comparisons must be taken critically, also when they are promising. For instance, none of the standard shallow water runup models comprise viscous boundary layers. However, they do possess other features that may reduce the runup height, such as premature/unphysical breaking, numerical damping, or a quadratic sea-bed friction of the Manning type. In short, most features that make models more stable or rugged tend to reduce the runup heights. Good agreement with experiments may then be coincidental and is no certain indication on good model performance in general. Moreover, tuning of model properties to match small scale experiments is not a sound strategy. Specifically, adjustment of the coefficient in a Manning friction to reproduce experimental runup heights obtained in standard wave tanks is inappropriate since the Manning friction is a quadratic drag inferred from turbulent channel flows. The frictions in action in the model and the experiments may thus have different natures and scaling properties.

In full scale even a non-breaking wave presumably yields turbulent swash flow with different properties from the one at laboratory scale. Moreover, even at laboratory scale a breaking wave will produce a turbulent runup. Hence, the difference between breaking and non-breaking runup regimes may be more pronounced in experiments than in full scale. From this point of view, runup on inclined planes is far from exhausted as a research field. New experiments, on different scales, covering a wide range of slope angles and amplitudes and with a more detailed observation of the shoreline and evolution of the surface and velocity fields should be performed.

ACKNOWLEDGMENTS

The assistance by Arve Kvalheim and Svein Vesterby at the Hydrodynamics Laboratory is gratefully acknowledged. This work is supported by the Norwegian Research Council under the project 205184/F20.

APPENDIX: BOUNDARY LAYER FLOW APPROXIMATIONS AND SOLUTIONS

1. Dimensionless variables and linearization

The boundary layer thickness δ_{bl}, is tacitly assumed to follow the classical relation $\delta_{bl} = \sqrt{\nu t_{sc}}$, introducing U_0 as the characteristic value of u we find $t_{sc} = U_0/g \sin\theta$ and $s_{sc} = U_0^2/g \sin\theta$, where

s_{sc} is the estimated runup-length. The continuity equation is used to estimate a characteristic value w_{sc} for w in the boundary layer, giving $w_{sc} = \frac{U_0}{s_{sc}}\delta_{bl}$. Dimensionless variables are defined then as follows:

$$\tau = \frac{t}{t_{sc}},\ \xi = \frac{s}{s_{sc}},\ \zeta = \frac{z}{\delta_{bl}},\ u^{(o)} = \frac{U}{u_{sc}},\ u^{(i)} = \frac{u}{u_{sc}} - u^{(o)},\ w^{(i)} = \frac{w}{w_{sc}}, \tag{A1}$$

where U and $u^{(o)}$, the non-dimensional outer flow, are evaluated at the beach. The inner along-shore component is subtracted the outer flow, to render $u^{(i)}$ as the principal unknown. This is done to move the inhomogeneity from the momentum equation (see Eq. (4)) to the boundary condition at the beach.

When the definitions in (A1) are inserted into the equations of Sec. II C and nonlinearities are omitted we obtain

$$\frac{\partial u^{(i)}}{\partial \tau} = \frac{\partial^2 u^{(i)}}{\partial \zeta^2}, \tag{A2}$$

subject to

$$u^{(i)}(\xi, 0, \tau) = -u^{(o)}(\xi, \tau), \quad u^{(i)}(\xi, \infty, \tau) = 0. \tag{A3}$$

The continuity equation remains in the form (5) and provides an explicit expression for $w^{(i)}$ in the linear case. Two-point boundary value problems such as (A2) and (A3) are discussed in many textbooks; see, for example, Chap. 7 in Mei.[56] The solution of Eq. (A2) subject to (A3) can most readily be obtained by following Liu and Orfila.[55] To do so, a local time $\tau\prime$ related to the global time τ by

$$\tau' = \tau - \tau_\xi \tag{A4}$$

is introduced. By definition, $\tau = \tau_\xi$ at the instant the front of a runup wave passes the position ξ, and at that very moment we assume that a viscous boundary layer will start to develop at ξ. We then get, using Eq. (2.15) in Liu and Orfila,[55]

$$u^{(i)}(\xi, \zeta, \tau; \tau_\xi) = -\frac{\zeta}{2\sqrt{\pi}} \int_0^{\tau - \tau_\xi} \frac{u^{(o)}(\xi, \tau_\xi + \tau')}{(\tau - \tau_\xi - \tau')^{3/2}} e^{-\zeta^2/4(\tau - \tau_\xi - \tau')} d\tau', \tag{A5}$$

where τ_ξ parameterizes the inherent ξ-dependence in the boundary layer flow, different from the ξ-dependence imposed by matching with the outer flow. In our application the outer flow is supposed to be given as

$$u^{(o)}(\xi, \tau) = 1 + a(\xi)\,\tau + b(\xi)\,\tau^2 + c(\xi)\,\tau^3 + d(\xi)\,\tau^4 + f(\xi)\,\tau^5 + \cdots, \tag{A6}$$

where we put $\tau = 0$ at the instant when the shoreline passes the reference position $\xi = 0$. Using (A6) in (A5) and adding the outer flow $u^{(o)}$ we find an expression for the total along-shore velocity

$$\begin{aligned}
u_t^{(i)} = {} & [1 + a\tau + b\tau^2 + c\tau^3 + d\,\tau^4 + f\,\tau^5]\,\mathrm{erf}\left(\frac{\zeta}{2\sqrt{\tau - \tau_\xi}}\right) \\
& - \frac{1}{30240}[15120\,a\zeta^2 + b\,(30240\,\zeta^2\tau + 2520\,\zeta^4) + c\,(45360\,\zeta^2\,\tau^2 + 7560\,\zeta^4\tau + 252\,\zeta^6) \\
& + d\,(60480\,\zeta^2\,\tau^3 + 15120\,\zeta^4\,\tau^2 + 1008\,\zeta^6\,\tau + 18\,\zeta^8) \\
& + f\,(75600\,\zeta^2\,\tau^4 + 25200\,\zeta^4\,\tau^3 + 2520\,\zeta^6\,\tau^2 + 90\,\zeta^8\,\tau + \zeta^{10})]\left[1 - \mathrm{erf}\left(\frac{\zeta}{2\sqrt{\tau - \tau_\xi}}\right)\right] \\
& + \frac{1}{30240\sqrt{\pi}}\{30240\,a\zeta + b[\zeta\,(50400\,\tau + 10080\,\tau_\xi) + 5040\,\zeta^3] \\
& + c[\zeta\,(66528\,\tau^2 + 18144\,\tau\,\tau_\xi + 6048\,{\tau_\xi}^2) + \zeta^3\,(14112\,\tau + 1008\,\tau_\xi) + 504\,\zeta^5] \\
& + d[\zeta(80352\,\tau^3 + 25056\,\tau^2\,\tau_\xi + 11232\,\tau\,{\tau_\xi}^2 + 4320\,{\tau_\xi}^3) \\
& + \zeta^3(26640\,\tau^2 + 432\,{\tau_\xi}^2 + 3168\,\tau\,\tau_\xi) + \zeta^5(1944\,\tau + 72\,\tau_\xi) + 36\,\zeta^7]
\end{aligned}$$

$$+ f[\zeta\,(92640\,\tau^4 + 31200\,\tau^3\tau_\xi + 15840\,\tau^2\,{\tau_\xi}^2 + 8160\,\tau\,{\tau_\xi}^3 + 3360\,{\tau_\xi}^4)$$
$$+ \zeta^3(42240\,\tau^3 + 6480\,\tau^2\tau_\xi + 1440\,\tau\,{\tau_\xi}^2 + 240\,{\tau_\xi}^3)$$
$$+ \zeta^5(4704\,\tau^2 + 312\,\tau\,\tau_\xi + 24\,{\tau_\xi}^2) + \zeta^7(176\,\tau + 4\,\tau_\xi) + 2\,\zeta^9]\}\sqrt{\tau - \tau_\xi}\,e^{-\zeta^2/4(\tau-\tau_\xi)}, \quad \text{(A7)}$$

where $\tau > \tau_\xi$. Maple is used to manage the mathematical manipulations necessary to obtain (A7) where some care has to be exercised when evaluating the boundary values of the integrals. An arbitrary position ξ in the runup, say $\xi(\tau_\xi)$, can be related to the Eulerian field (A6) approximately by series expansions and time integration. Such a relation is necessary when obtaining $w^{(i)}$ from the continuity equation.

2. An idealized model for boundary layers during runup

To gain some insight into the evolution of the viscous boundary layers on the beach, we analyze a simple plug flow model that allows for closed form solutions of the boundary layer equations (see Sec. IV B). We ignore the stretching of the runup tongue, implying that a slab of water is moving uniformly on the beach while being retarded by gravity through the pressure from the beach. The outer flow velocity evaluated at the beach in this idealized model is

$$u^{(o)} = 1 - \tau = -\tau_\xi - \tau', \quad \text{(A8)}$$

giving an arbitrary position ξ of the fluid plug as

$$\xi = \tau_\xi - \frac{1}{2}\tau_\xi^2 \quad \text{(A9)}$$

or

$$\tau_\xi = 1 - \sqrt{1 - 2\xi}. \quad \text{(A10)}$$

The outer flow (A8) introduced here, corresponds to putting $a(\xi) = -1$ and $b(\xi) = c(\xi) = d(\xi) = f(\xi) = 0$ in (A6) and (A7) giving the solution expressed in (8) and (9).

The significance of nonlinearities can be measured as the ratio, N_L, between the convective term in (4) and a dominant term, namely the along-shore acceleration due to gravity ($g\sin\theta$ with dimensions, unity without dimensions). For $U_0 = 1$ m/s, which is higher than the maximum velocities for the lower solitary waves investigated herein, we obtain ratios as shown in Figures 17 and 18 below. The figures indicate that nonlinearity is rather weak in the domain displayed, except for the front of the runup wave where we expect that a break-down of the boundary layer equations will occur. This is consistent with the numerical results in Figure 8 for $A/d \approx 0.1$. Hence, it is likely that the linearized solution carries the main features of the boundary layer flow associated with the runup of small amplitude waves.

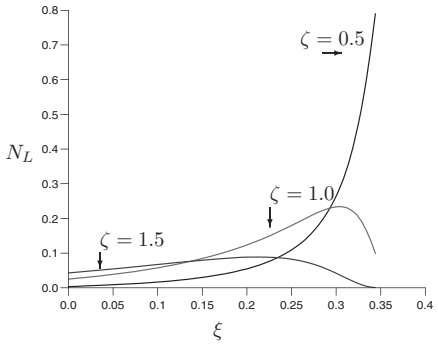

FIG. 17. The ratio N_L for $\tau = 0.5$ at various locations in the boundary layer.

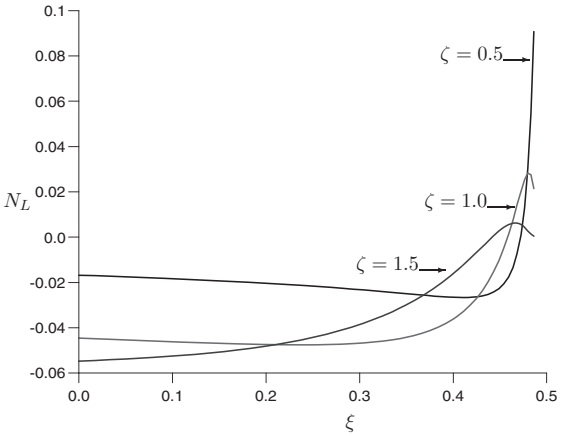

FIG. 18. The ratio N_L for $\tau = 0.9$ at various locations in the boundary layer is displayed in the figure.

[1] H. Yeh, C. E. Synolakis, and P. L.-F. Liu, *Long-wave Runup Models* (World Scientific, Singapore, 1996).
[2] *Advanced Numerical Models for Simulating Tsunami Waves and Runup*, Advances in Coastal and Ocean Engineering Vol. 10, edited by P. L.-F. Liu, H. Yeh, and C. E. Synolakis (World Scientific, Singapore, 2008).
[3] N. Shuto, "Transformation of nonlinear long waves," Coastal Eng. Proc. **15**, 423–440 (1976). (available at http://journals.tdl.org/ICCE1/article/view/3072).
[4] J. W. Miles, "Solitary waves," Annu. Rev. Fluid Mech. **12**, 11–43 (1980).
[5] P. A. Madsen, D. R. Fuhrman, and H. A. Schäffer, "On the solitary wave paradigm for tsunamis," J. Geophys. Res. **113**, C12012, doi:10.1029/2008JC004932 (2008).
[6] R. E. Meyer and A. D. Taylor, "Run-up on beaches," in *Waves on Beaches and Resulting Sediment Transport* (Publication of the Mathematics Research Center, University of Wisconsin, 1972), pp. 95–122.
[7] J. V. Hall and J. W. Watts, "Laboratory investigation of the vertical rise of solitary waves on impermeable slopes," Tech. Memo. 33 (Beach Erosion Board, U.S. Army Corps of Engineers, 1953).
[8] C. E. Synolakis, "The run-up of solitary waves," J. Fluid Mech. **185**, 523–545 (1987).
[9] I. A. Svendsen and S. T. Grilli, "Nonlinear waves on steep slopes," J. Coastal Res. **7**(Special Issue), 185–202 (1990).
[10] Y. Li and F. Raichlen, "Solitary wave runup on plane slopes," J. Waterway, Port, Coastal, Ocean Eng. **127**, 33–44 (2001).
[11] Y. Li and F. Raichlen, "Non-breaking and breaking solitary wave run-up," J. Fluid Mech. **456**, 295–318 (2002).
[12] A. Jensen, G. Pedersen, and D. J. Wood, "An experimental study of wave run-up at a steep beach," J. Fluid. Mech. **486**, 161–188 (2003).
[13] A. Jensen, S. Mayer, and G. Pedersen, "Experiments and computation of onshore breaking solitary waves," Meas. Sci. Technol. **16**, 1913–1920 (2005).
[14] M. J. Briggs, C. E. Synolakis, G. S. Harkins, and D. R. Green, "Laboratory experiments of tsunami runup on a circular island," Pure Appl. Geophys. **144**, 569–593 (1995).
[15] G. Sælevik, "Particle image velocimetry applied to complex flows in a wave tank," Ph.D. dissertation (University of Oslo, 2009).
[16] T. O'Donoghue, D. Pokrajac, and L. Hondebrink, "Laboratory and numerical study of dambreak-generated swash on impermeable slopes," Coastal Eng. **57**, 513–530 (2010).
[17] I. M. Sou, E. A. Cowen, and P. L.-F. Liu, "Evolution of the turbulence structure in the surf and swash zones," J. Fluid Mech. **644**, 193–216 (2010).
[18] G. F. Carrier and H. P. Greenspan, "Water waves of finite amplitude on a sloping beach," J. Fluid Mech. **4**, 97–109 (1958).
[19] V. V. Titov and C. E. Synolakis, "Numerical modeling of tidal wave runup," J. Waterway, Port, Coastal, Ocean Eng. **124**, 157–171 (1998).
[20] Pacific Marine Environmental Laboratory, 7600 Sand Point Way NE Seattle, "Tsunami Research Program" (2005), as of December 2012, available at http://www.pmel.noaa.gov/tsunami/research.html.
[21] F. Imamura, "Review of tsunami simulation with a finite difference method," in *Long-wave Runup Models*, edited by H. Yeh, C. E. Synolakis, and P. L.-F. Liu (World Scientific, Singapore, 1996), pp. 25–42.
[22] J. T. Kirby, G. Wei, Q. Chen, A. B. Kennedy, and R. A. Dalrymple, "Fully nonlinear Boussinesq wave model documentation and user's manual," Research Report CACR-98-06 (Center for Applied Coastal Research, Department of Civil Engineering, University of Delaware, Newark, DE 19716, 1998) as of December, 2012, available at http://chinacat.coastal.udel.edu/papers/cacr-98-06.ps.
[23] P. J. Lynett, T.-R. Wu, and P. L.-F. Liu, "Modeling wave runup with depth-integrated equations," Coastal Eng. **46**, 89–107 (2002).

[24] G. Pedersen, "Modeling run-up with depth integrated equation models," in *Advanced Numerical Models for Simulating Tsunami Waves and Runup*, Advances in Coastal and Ocean Engineering Vol. 10, edited by P. L.-F. Liu, H. Yeh, and C. E. Synolakis (World Scientific, Singapore, 2008), pp. 3–42.
[25] S. Grilli, I. Svendsen, and R. Subramanya, "Breaking criterion and characteristics for solitary waves on slopes," J. Waterway, Port, Coastal, Ocean Eng. **123**(3), 102–112 (1997).
[26] P. Lin, K.-A. Chang, and P. L.-F. Liu, "Runup and rundown of solitary waves on sloping beaches," J. Waterway, Port, Coastal, Ocean Eng. **125**(5), 247–255 (1999).
[27] S. Guignard, R. Marcer, V. Rey, C. Kharif, and P. Fraunié, "Solitary wave breaking on sloping beaches; 2-D two phase flow numerical simulation by SL-VOF method," Eur. J. Mech. B/Fluids **20**, 57–74 (2001).
[28] J. J. Monaghan and A. Kos, "Solitary waves on a Cretan beach," J. Waterway, Port, Coastal, Ocean Eng. **125**, 145–154 (1999).
[29] P. Lubin, "Simulation des grandes echelles du deferlement plongeant des vagues," Ph.D. dissertation (L'Université Bordeaux, 2004) (in English).
[30] G. Gisler, R. Weaver, and G. M, "Sage calculations of the tsunami threat from La Palma," Sci. Tsunami Hazards **24**, 288–301 (2006).
[31] Z. Wang, Q. Zou, and D. Reeve, "Simulation of spilling breaking waves using a two phase flow CFD model," Comput. Fluids **38**, 1995–2005 (2009).
[32] R. Bakhtyar, A. Razmi, D. Barry, A. Yeganeh-Bakhtiary, and Q.-P. Zou, "Airwater two-phase flow modeling of turbulent surf and swash zone wave motions," Adv. Water Resour. **33**, 1560–1574 (2010).
[33] G. Pedersen, "A Lagrangian model applied to runup problems" in *Advanced Numerical Models for Simulating Tsunami Waves and Runup*, Advances in Coastal and Ocean Engineering Vol. 10, edited by P. L.-F. Liu, H. Yeh, and C. E. Synolakis (World Scientific, Singapore, 2008), pp. 311–314.
[34] S. Carstensen, B. M. Sumer, and J. Fredsøe, "Coherent structures in wave boundary layers. Part 1. Oscillatory motion," J. Fluid Mech. **646**, 169–206 (2010).
[35] G. H. Keulegan, "Gradual damping of solitary waves," J. Res. Natl. Bur. Stand. **40**, 497–498 (1948).
[36] P. J. Diamessis and L. G. Redekopp, "Numerical investigation of solitary internal wave-induced global instability in shallow water benthic boundary layers," J. Phys. Oceanogr. **36**, 784–812 (2006).
[37] M. Carr and P. A. Davies, "The motion of an internal solitary wave of depression over a fixed bottom boundary in a shallow, two-layer fluid," Phys. Fluids **18**, 016601 (2006).
[38] P. L.-F. Liu, Y. S. Park, and E. A. Cowen, "Boundary layer flow and bed shear stress under a solitary wave," J. Fluid Mech. **574**, 449–463 (2007).
[39] G. Vittori and P. Blondeaux, "Turbulent boundary layer under a solitary wave," J. Fluid Mech. **615**, 433–443 (2008).
[40] B. M. Sumer, P. M. Jensen, L. B. Sørensen, J. Fredsøe, P. L.-F. Liu, and S. Carstensen, "Coherent structures in wave boundary layers. Part 2. Solitary motion," J. Fluid Mech. **646**, 207–231 (2010).
[41] B. N. J. Persson, O. Albohr, U. Tartaglino, A. I. Volokitin, and E. Tosatti, "On the nature of surface roughness with application to contact mechanics, sealing, rubber friction and adhesion," J. Phys.: Condens. Matter **17**, 82 (2005).
[42] EngineeringToolBox, as of December, 2012, available at http://www.engineeringtoolbox.com/surface-roughness-ventilation-ducts-d_209.html.
[43] F. M. White, *Viscous Fluid Flow*, Mechanical Engineering (McGraw-Hill, 2006).
[44] S. B. Dalziel, *DigiFlow User Guide*, Dalziel Research Partners, Histon, Cambridge, UK, as of December, 2012, available at http://www.dalzielresearch.com/digiflow, 2006.
[45] R. Theunissen, F. Scarano, and M. L. Riethmuller, "On improvement of PIV image interrogation near stationary interfaces," Exp. Fluids **45**, 557–572 (2008).
[46] E. K. Lindstrøm, "Run-up of solitary waves," M.S. thesis, University of Oslo, 2011.
[47] M. Cooker, D. Peregrine, C. Vidal, and J. Dold, "The interaction between a solitary wave and a submerged semicircular cylinder," J. Fluid Mech. **215**, 1–22 (1990).
[48] J. W. Dold, "An efficient surface-integral algorithm applied to unsteady gravity waves," J. Comput. Phys. **103**, 90–115 (1992).
[49] M. Tanaka, "The stability of solitary waves," Phys. Fluids **29**(3), 650–655 (1986).
[50] F. P. Bertolotti, T. Herbert, and P. R. Spalart, "Linear and nonlinear stability of the Blasius boundary layer," J. Fluid Mech. **242**, 441–474 (1992).
[51] M. Langsholt, "Experimental study of wave run-up," Cand. Real. thesis (University of Oslo, 1981).
[52] G. Pedersen and B. Gjevik, "Run-up of solitary waves," J. Fluid Mech. **135**, 283–299 (1983).
[53] S. Hibberd and D. H. Peregrine, "Surf and run-up on a beach: a uniform bore," J. Fluid Mech. **95**, 323–345 (1979).
[54] D. H. Peregrine and S. M. Williams, "Swash overtopping a truncated plane beach," J. Fluid Mech. **440**, 391–399 (2001).
[55] P. L.-F. Liu and A. Orfila, "Viscous effects on transient long-wave propagation," J. Fluid Mech. **520**, 83–92 (2004).
[56] C. C. Mei, *Mathematical Analysis in Engineering* (Cambridge University Press, Cambridge, 1997).

Part II

A note on instabilities in the boundary layer during runup of solitary waves on a plane slope

Dept. of Math. University of Oslo
Mechanics and Applied Mathematics no 01
ISSN 0809–4403 September 2014

A note on instabilities in the boundary layer during runup of solitary waves on a plane slope

Erika K. Lindstrøm, Joris C. G. Verschaeve, Geir K. Pedersen

September 15, 2014

1 Abstract

The present report is concerned with the evolution of boundary layers during runup of solitary waves on a beach in a wave tank of depth 0.2 m. It comprises both theory and high resolution PIV measurements of velocity profiles. A linear stability analysis of the boundary layer for solitary waves running up a sloping beach is performed by means of the Orr-Sommerfeld equation. Due to the increased retardation phase during runup, the amplification of disturbances in the boundary layer is increased as compared to that of solitary waves traveling on constant depth. On the basis of these results, we reexamine the experimental results by Pedersen *et al.* [11] and find some experimental evidence for Tollmien-Schlichting waves destabilizing the flow.

2 Introduction

Runup on waves on inclined planes, with apparent applications to tsunamis and coastal engineering, is a topic which has been studied in a series experimental and theoretical papers over the last 60 years, say. Any kind of review is beyond the scope of this report and we refer to the references given in the papers cited below. In [7, 8] runup on a broken beach was investigated, among other things. For reference also the standard experiment of runup on an inclined plane was revisited. Surprisingly, these experiments yielded much lower runup than theoretical inviscid models. The presence of a viscous boundary layer was apparent, but this was inadequately resolved in the measurements. A new set of experiments, with particular emphasis on shoreline tracking and measurement of viscous boundary layer for solitary waves incident on a beach was performed and published in Pedersen *et al* [11]. In some cases they found very good general agreement between their experimental and numerical velocity profiles in the boundary layer. They also unraveled a delay in the runup, most pronounced for small amplitudes, due to capillary effects. Moreover, the reduced runup heights from [7, 8], as compared to inviscid theories, were reproduced. In [11] this was linked to the viscous effects through integrated mass transport deficiencies and dissipation in the boundary layer, which points to a scale dependency of wave tank experiments of this kind. A survey of the experimental literature also suggested that this was observed before, although being little appreciated.

In some of the experiments reported by Pedersen et al. [11] they observed undulations in the steamline patterns of the boundary layers followed by the development of structures that may be vortex rollers. During withdrawal, when the flow again is accelerated, the boundary layers returned to a regular flow without signs of instabilities or transition. Since no previous analysis or investigation of boundary layers on beaches was available, the authors compared their findings to the related case of boundary layers

under solitary waves for which there is a small number of studies in the literature. In particular, the works by [12, 14, 15, 9] reported the boundary layer stability under solitary waves to be of parametric nature, meaning that the boundary layer turns unstable in an absolute sense beyond a critical Reynolds number. Instabilities did first occur in the retardation phase where an inflection point develops in the boundary layer profile. Since the flow during runup on a beach is a retarded one [11] suggested that it may have similar boundary layer properties and found irregularities for Reynolds numbers of similar magnitudes as [12, 14, 15, 9]

Another line of research was attempted by [2] who subjected the stability of boundary layers under solitons on constant depth to stability analysis by means of an Orr-Sommerfeld type equation. Later [13] has taken this line of approach much further and contested the concept of parametric instability with a critical Reynolds number. The latter reference found, on the basis of a linear stability analysis, that the boundary layer under a solitary wave is convectively unstable, meaning that the boundary layer acts like a broadband amplifier for incoming perturbations. They explained the observation of diverging critical Reynolds numbers found by [12, 14, 15, 9] by the fact that the level of noise in these experiments and direct numerical simulations was uncontrolled and therefore no repeatability of the flow transition could be expected.

The results [13] motivates us for a renewed investigation of the boundary layers during runup. Herein, we shall investigate the stability properties of the boundary layer under solitary waves running up a sloping beach numerically by means of linear stability. In particular we apply the Orr-Sommerfeld equation to the boundary layer profiles computed in [11]. New experiments have not yet been finalized, but the measurements of [11] will be re-processed and interpreted in light of the stability analysis. In particular we seek experimental evidence for the present theoretical results.

The present note is organized as follows. In section 3, a short description of the problem is presented. Following, we explain the basic equations of the present linear stability analysis in section 4. This section also contains the discussion on the theoretical results of the present note. We then turn to the reexamination of the experimental work by Pedersen *et al* [11] in section 5. Next to a short description of the experimental post-processing, the results of the reexamination are discussed in this section. The present note is concluded in section 6.

3 Description of the problem

The set up was defined in [11] and will only be summarized briefly here. A solitary waves with amplitude a is traveling from left to right with speed c in a basin with constant depth $d = 0.2\,\mathrm{m}$ which is then joined by a plane with inclination angle $\theta = 10^\circ$. In the experiments the wave is generated by a piston wave paddle, while it is introduced through initial conditions in the numerical wave models.

The amplitudes of the solitary waves vary between approximately $a/d \sim 0.1$ to $a/d \sim 0.5$. However, most emphasis is put on $a/d = 0.292$ for which we have best measurements. This is also the only amplitude subjected to stability analysis. As shown in the figure we have a coordinate system x, z aligned parallel and normal to the beach, respectively. For use in the boundary layer computations the x axis is construed to follow also the flat part of the bottom, still with z denoting the normal direction, which then is vertical. In addition we have a horizontal/vertical ξ, ζ system. The origin of both systems are located at the equilibrium shoreline. Some features of the setup are shown in figure 1. In the discussion of the stability theory we will use rescaled, non-dimensional, coordinates. Elsewhere units will generally be applied, or the scaling explicitly stated (such as $a/d \approx 0.3$).

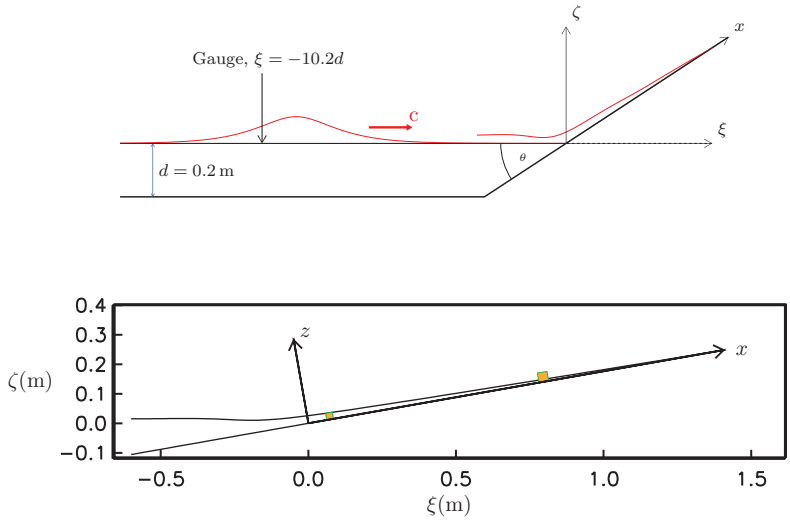

Figure 1: Sketch of problem. Upper panel: Side view of wave tank with the initial wave and the surface at maximum runup as obtained from an inviscid model for $a/d \sim 0.3$. The time series from the gauge is used to synchronize experiments and theory. Lower panel: the swash zone at maximum runup for $a/d \sim 0.3$ with true aspect ratio. The lower and upper rectangles are FOV 2 and 3, respectively. FOV 1 is located in mid-tank in about the same position as FOV 2.

At $\xi = -d/\tan\theta$, the plane beach is installed. When the solitary wave reaches this points it will start to produce a gentle reflection, which will mildly influence the properties of the boundary layers close to the start of the beach. During shoaling the front will steepen, yielding a shorter and stronger acceleration phase as compared to retardation phase. When the solitary wave reaches the shoreline, it will develop a thin swash tongue running up the beach(see lower panel of figure 1) . Gravity will decelerate and then reverse the flow. The flow is first reversed close to the $\xi = 0$ and finally at the moving shoreline when the maximum runup height is reached. The flow is then reversed everywhere reverse and the draw down phase starts. Figure 2 shows a time series of the free stream velocity U_{inviscid} of the boundary layer for the positions in figure 3. The typical free stream velocity of a solitary wave in the constant-depth part of the tank displays an acceleration phase followed by a retardation phase in a symmetrical fashion. In the lowest part of the swash zone a short acceleration phase is followed by a longer retardation which then is conceived as acceleration again as the flow is reversed. Further up the beach the initial acceleration phase is missing and the deceleration phase is even stronger. The larger velocities and stronger retardation during runup must be expected to increase the amplification of perturbations in the boundary layer, destabilizing the flow, as compared to the propagation on constant depth. This boundary layer was investigated by Pedersen *et al.* [11], who solved the boundary layer equations numerically, with outer flows taken from numerical solutions of inviscid wave models. In addition they performed PIV measurements of the boundary layer flow at selected positions as indicated in figure 1. As mentioned in the introduction, the theoretical and experimental profiles were agreeing well, except for some cases, where instabilities were observed to change the flow pattern. The investigation of the stability properties of the boundary layer flow is the focus of the present work, which can be considered a continuation of the work by Pedersen *et al.* [11]. We shall first perform some theoretical considerations, section 4, before turning to the reexamination of the PIV measurements at the locations

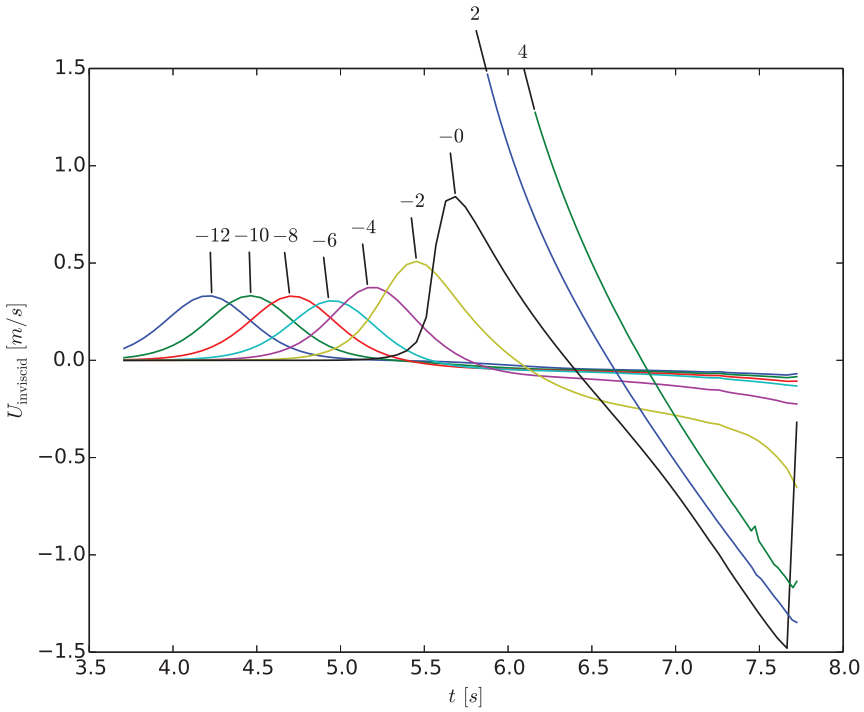

Figure 2: Free stream velocity for different values of ξ^*/d in finite depth and onshore.

in figure 1, cf. section 5.

4 Theory

4.1 Basic equations

In [11], the boundary layer flow under a solitary wave running up a sloping beach was solved numerically. We shall use this solution to perform a stability analysis by means of the Orr-Sommerfeld equation. The solution of the boundary layer equations in [11], leads to a velocity field

$$U_{\text{bl}}(x, y, t) \quad V_{\text{bl}}(x, y, t), \tag{1}$$

in the boundary layer, which is the subject of the present linear stability analysis.

The scaling of quantities in equation (1) is the following. The velocities in tangential and wall normal direction are scaled by the shallow water speed $\sqrt{gd}$. Time is scaled by $d/\sqrt{gd}$ and horizontal lengths are scaled by d. On the other hand, wall normal lengths are scaled by δ^*, where δ^* is a viscous length scale defined in [14, 15]:

$$\delta^* = \sqrt{\frac{2\nu d}{\sqrt{gd}}}. \tag{2}$$

The scale δ^* allows for a non-dimensional small parameter $\delta = \delta^*/d$, which equals for the present flow

depth:

$$\delta = 2.67 \cdot 10^{-3}. \tag{3}$$

The Reynolds number Re for a scaling based on δ^* and $\sqrt{gd}$ is given by:

$$\mathrm{Re} = \frac{2}{\delta}. \tag{4}$$

In equation (1) the components are tangential and normal to the bottom. Hence, for $x^* < -d/\sin\theta$, cf. figure 1, the tangential coordinate is given by ξ, whereas the normal coordinate is given by ζ. Thus, the coordinate system for the boundary layer analysis thus always follows the bottom of the wave tank. The flow defined by (1) is time dependent which necessitates some specification about the exact sense of instability in the present case, since traditionally instability is defined as the departure from one steady solution to another flow regime. The meaning of instability employed here is akin to the concept of spatial growth for a steady boundary layer [6]. For spatial growth, the boundary layer flow is characterized by slow horizontal change, whereas the perturbation displays a rapid variation in the horizontal direction. This concept of two scales, a slow scale for the base flow and a fast one for the perturbation, is in the present note applied to the temporal variation of the flow. The resulting formulation is equivalent to the one in [1]. Given a position x_0 along the beach, the boundary layer flow can be regarded as a succession of slowly varying profiles in z. The stream function ψ' of a Tollmien-Schlichting wave with wave number α can then be written as:

$$\psi' = \phi(y) \exp\{\mathrm{i}\alpha x - \omega t\}, \tag{5}$$

where ϕ is a shape function in wall normal direction. The imaginary part of the complex number ω gives us the frequency of the perturbation, whereas the real part stands for the growth rate of the perturbation. The Tollmien-Schlichting wave displays fast variation compared to the base flow. However, the quantities ϕ and ω are assumed to vary on the same scale as the base flow. The governing equation for ψ' is the celebrated Orr-Sommerfeld equation [3]:

$$\frac{1}{\mathrm{Re}} \left(D^2 - \alpha^2\right)^2 \phi - (\mathrm{i}\alpha U_{\mathrm{bl}} - \omega) \left(D^2 - \alpha^2\right) \phi + \mathrm{i}\alpha D^2 U_{\mathrm{bl}} \phi = 0, \tag{6}$$

where $D = d/dz$. In contrast to the traditional solution of (6), the flow field is not varied in x, but in t, that means, we fix a certain position x_0 and apply equation (6) on a series of profiles for t. Equation (6) is an eigenvalue problem for the eigenvalue ω and the eigenvector ϕ. The boundary layer flow becomes unstable, as soon as the real part of ω for any wave number α becomes positive. The region in the (t, α) plane for which the real part of ω vanishes is called the neutral curve. It separates the stable from the unstable region. In addition to the neutral curve, the total amplification of the Tollmien-Schlichting wave is of major interest, as it tells us by which factor the perturbation will grow during the passage of the solitary wave. The amplification A/A_0 is computed by the following formula:

$$\frac{A}{A_0} = \exp \int_{t_0}^{t} \mathrm{real}\,(\omega)\; dt. \tag{7}$$

Equation (6) is solved by means of a Chebyshev collocation method as in [13], with 130 nodes in y direction. The following section presents the results of the above Orr-Sommerfeld analysis applied to the boundary layer flow in [11].

4.2 Results

The Orr-Sommerfeld equation, equation (6), is solved for a number of positions along the boundary. In the following, we denote each position by its horizontal distance ξ from the origin. The value of the abscissa x on the beach is then obtained by

$$x = \frac{\xi}{\cos\theta}. \tag{8}$$

In figure 3, the neutral curves in the (t, α) for these positions are plotted. When the solitary wave is still propagating on constant depth (for $\xi < -1/\tan\theta \approx -5.67$), the shape of the neutral curve for early times is close to the one for a solitary wave traveling in an infinite basin of constant depth d [13]. The neutral curve starts behind the crest of the solitary wave, where the external flow is decelerating and the resulting external pressure gradient causes the flow in the boundary layer to reverse. However, for later times, the shape of the neutral curves differs from the one of a solitary wave in an infinite basin. The neutral curve reconnects and forms a closed curve much earlier in time. This is due to the reflection of the solitary wave on the beach, which leads to a wave (different in amplitude and shape) traveling the opposite direction, i.e. from right to left. This wave is again characterized by an initial acceleration phase, which stabilizes the flow and leads to an earlier closure of the neutral curve for positions further away from the beach.

For positions on the beach, we see a continuous evolution of the shape of the unstable region. Its extent in time decreases until the equilibrium shoreline $\xi = 0$, when its duration starts to increase again. The span in wave numbers α increases for increasing ξ. For later times the neutral curve develops a kind of bump for $\xi \geq 2$. Even if the neutral curves in the boundary layer of a solitary wave running up a sloping beach display some evolution when compared to the neutral curve for a solitary wave propagating on constant infinite depth, the most dramatic change is in the amplification of the perturbations. In figure 4 top, the amplification of the critical Tollmien-Schlichting waves is plotted for the positions defined in figure 3. Far from the beach, the amplification of the critical Tollmien-Schlichting wave corresponds basically to the one of a solitary wave traveling in an infinitely long basin. However as we approach the shoreline, the maximum amplification decreases, only to show a strong increase towards the end of the swash tongue. This indicates that the stability features in the boundary layer of the swash tongue differ significantly from those of the boundary layer under a solitary wave traveling on constant depth. Further evidence can be obtained by looking at the phase speed of the critical Tollmien-Schlichting wave, cf. figure 4 bottom. Since the Tollmien-Schlichting wave is advected by the flow in the boundary layer, its phase speed reflects qualitatively the boundary layer flow. Far from the beach, we observe first an acceleration of the Tollmien-Schlichting wave before the wave decelerates and moves in opposite direction. This pattern is slowly varied when moving towards the beach with the acceleration phase becoming shorter. Further up the beach $\xi = 2, 4$, the acceleration phase is even completely missing and we only observe a deceleration phase in the beginning. For later times we observe a strong acceleration of the Tollmien-Schlichting wave down the beach. We remark that the very vicinity of the moving shoreline our solution is not correct. Firstly, the wave model from [11] do not include surface tension which will modify the dynamics of the shoreline (contact point). Secondly, the abrupt on-set of the outer flow when a given x position is inundated causes numerical large numerical errors locally.

5 Experimental work

In the present section we employ dimensional quantities, while omitting any stars.

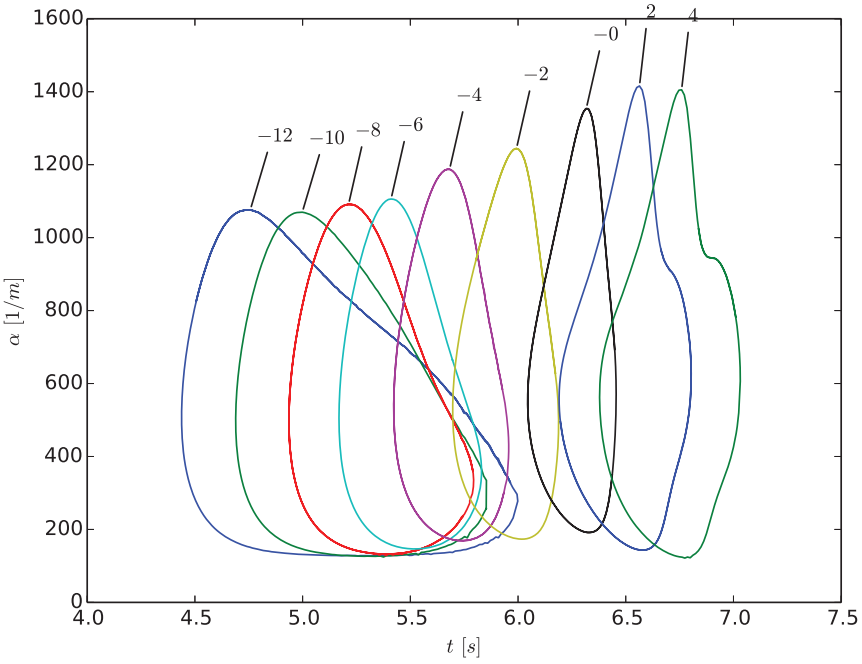

Figure 3: Neutral curves in the (t, α) plane for the boundary layer flow in [11]. The curves are computed for different values of ξ^*/d, which is annotated as a label to the respective curve in the figure.

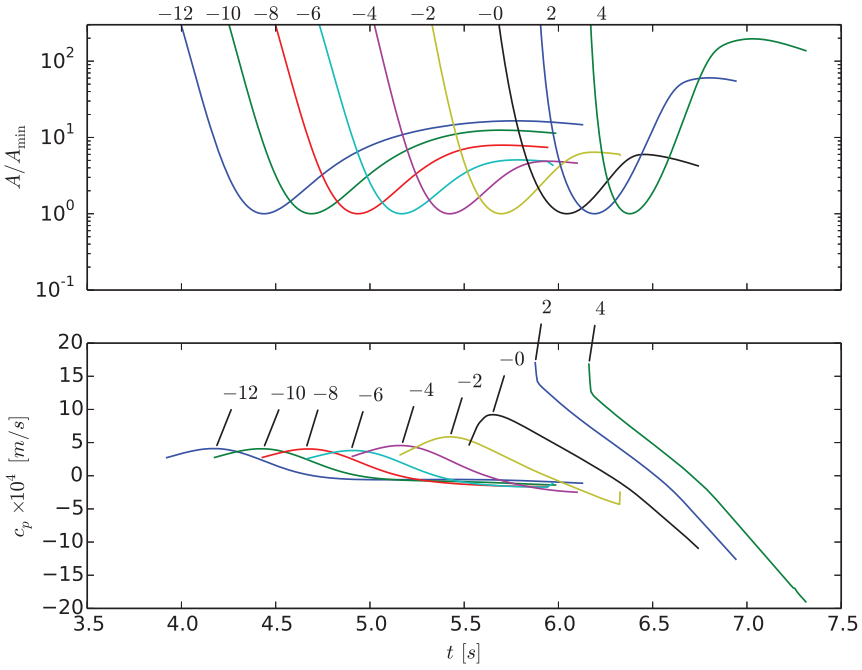

Figure 4: Top: Amplifications of the critical Tollmien-Schlichting waves in figure 3. Bottom: Phase speed of the critical Tollmien-Schlichting waves. Curves are marked with $\xi^\star/d$.

5.1 Experimental setup and instrumentation

Experiments were performed in a wavetank with length 25 m, width 0.51 m and depth 1 m. Both the walls and the bottom is made of glass, suitable for optical measuring techniques. A plane beach of 10° inclination was installed with the undisturbed shoreline located 7.1 m from the wave paddle. The incident solitary waves were generated by a piston type wave paddle by a modified "Goring's method", which is explained in [5]. The generated waves had the amplitudes $a/d = 0.0977, 0.195, 0.292, 0.388, 0.481$. A non-intrusive acoustic wave gauge (Banner U-Gage S 18U) was employed to measure the incident waves at a distance of 2.045 m from the equilibrium shoreline. This gauge was also used to monitor the equilibrium depth.

A PIV (particle image velocimetry) system was used to measure the velocity fields at the beach. Three field of views (FOV) were employed in in the work by PAL, one FOV was placed in the middle of the tank (25 cm from the side wall), 8 cm from the shoreline and with a window size of 5.6 cm × 5.6 cm. Two of them were located 5 cm from the side wall closest to the camera, placed 7.5 cm and 81 cm from the equilibrium shoreline position. These had window size of 2.3 cm × 2.3 cm and 3.3 cm × 3.3 cm respectively. The camera was aligned parallel to the beach, with resolution of 1024 × 1024 pixels and 2000-5000 frames per second. Wave gauges and PIV system was synchronized with the wave paddle, with $t = 0$ as the start of the paddle motion. A more detailed description of the experimental setup and instrumentation are found in [11].

5.2 Post-processing

The main purpose of the investigation in 2013 was to determine the cause of reduced runup heights in experiments compared to numerical models. Irregularities in the flow were detected in the upper FOV as well as in the lower FOV located in the middle of the wave tank. The main focus in the present work is to reanalyze the fluctuations in the flow in the upper FOV. Here, we apply a different kind of filtering to reveal some more details regarding these irregularities. Our main attention is given to the case $a/d = 0.292$. and especially the second of the three runs (Run 2). There is no strict repeatability considering amplitudes and time range of the detected irregularities and Run 2 displays the most distinct and regular oscillations in the flow pattern. Run 2 is also the one with the best seeding and, hence, the most accurate measurements. However, the difference in the measurement quality is probably not the sole reason for the differences between the experiments. For Run 1 and Run 3 the oscillations lasted for a shorter time, in addition to being less distinct. Both spatial and temporal resolution is considered for Run 2 while only spatial resolution is applied for Run 1 and Run 3.

To reduce noise, the data is averaged over 0.003 s in time and 0.02 mm in x. We note that the averaging period is smaller than in [11], where 0.01 s was applied. Figure 5 shows the filtered data where the fluctuations are visible. In order to extract perturbations from velocities, the horizontal velocity component is separated into a base flow, which is approximated as a linear function $u_0 + u_1 x$, and perturbations u_p:

$$u = u_0 + u_1 x + u_p \tag{9}$$

In order to verify the linear approximation of the base flow, it is compared with theoretical computations at the same position and time regime for nonlinear boundary layers which display a L2 norm of residuals in order of 10^{-5} m/s for spatial resolution and 10^{-3} m/s for temporal resolution. Figure 6 shows the original data, u, and the perturbations, u_p, from run 2 at $z = 1.9$ mm for $t = 6.43$ s in spatial resolution and $x = 0.807$ m for temporal resolution.

In addition the seeding in Run 1 and Run 3 were less dense than for Run 2, which resulted in reduced quality of the processed data due to lack of valid velocity vectors.

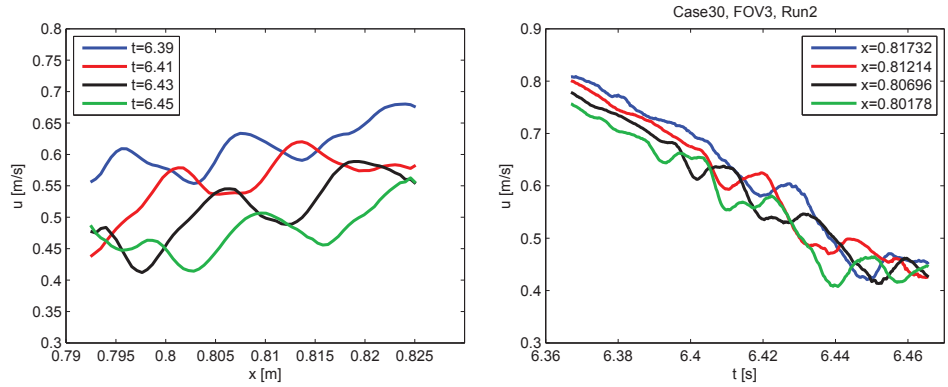

Figure 5: Detected irregularities in space (left) and time (right). $a/d = 0.292$ Run 2.

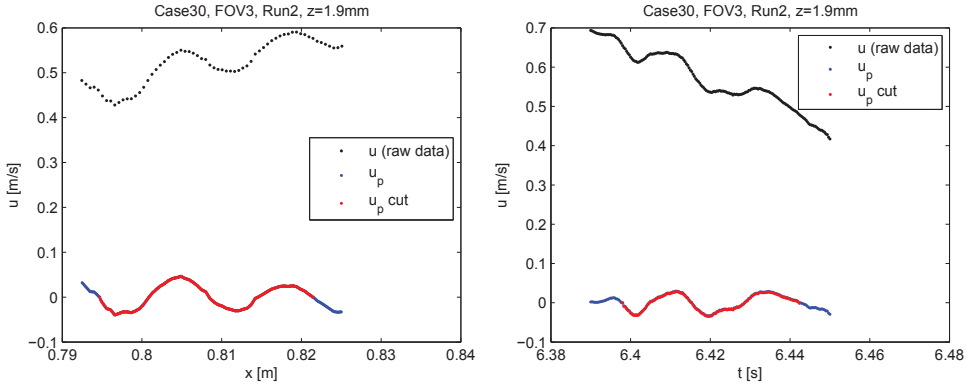

Figure 6: Horizontal velocity component u, perturbations, u_p, and selected sequence for the Fourier transformation, $u_p cut$. Data from $z = 1.9\,\text{mm}$. Left: Spatial resolution, $t = 6.43\,\text{s}$. Right: Temporal resolution, $x = 0.807\,\text{m}$. $a/d = 0.292$ Run2.

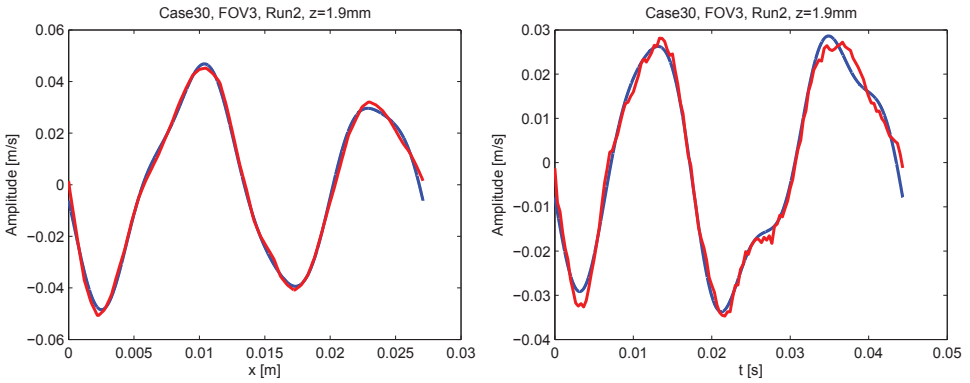

Figure 7: Perturbations plotted in red and Fourier approximation of the signal plotted in blue at $z = 1.9\,\text{mm}$. Left: Spatial resolution, $t = 6.43\,\text{s}$. Left: Temporal resolution, $x = 0.807\,\text{m}$. $a/d = 0.292$ Run 2.

Once the perturbations are extracted from the data, the first and last zero-crossings of the perturbations within the FOV are found and Fourier transformation is applied within the interval confined by the zero crossings. Thus, the chosen domain will determine the wavelengths in the Fourier transformation. This method is crude, and one must keep in mind that the length of the chosen sequence will vary in time or space for spatial or temporal resolution respectively. As a consequence of this is that the components of the Fourier transformation will also vary. Figure 7 shows the selected sequence, denoted u_{cut}, and the first five terms of the corresponding Fourier transformation for run 2 at $t = 6.43\,\text{s}$ and $x = 0.807\,\text{m}$.

Amplitudes of the Fourier components are normalized with the outer velocity of the flow. The outer flow is extracted from the PIV data at $z = 6.5\,\text{mm}$. There are drop outs in the outer flow, caused by poor seeding. Due to this, the outer flow velocity is taken as the median (mean of the middle two numbers in sorted order) over the chosen sequence for each time frame in spatial resolution and for each x-position in temporal resolution. For spatial resolution, the outer flow vary slightly within the FOV for each time frame, with maximum variation of 3%. Variation of the outer flow in temporal resolution is larger, with a maximum of 25%.

When possible, wavelengths or periods of the oscillations are found from visual inspection (no mathematical interpolation involved) of all the zero crossings of the perturbations within the FOV or time range considered. The method is to extract the distance between zero crossings covering one wavelength, for all wavelengths within the chosen sequence. The final estimate for the wavelength is then the average of all distances found within the sequence. This method is even more crude and are used for comparison to the Fourier transformation.

5.3 Experimental observations

5.3.1 Results of $a/d = 0.292$, Run 2

Figure 9-11 shows streamlines at different stages of the flow during run up and draw down, while figure 12 shows the corresponding horizontal velocity component, u, at $z = 1.9\,\text{mm}$. No irregularities are noticeable in the early stage of the run up, then small fluctuations occur which develop to what might be related to Tollmien Schlichting waves. These waves are regular for a very short time before the oscillations become more irregular, followed by formation of vortices in the boundary layer which seems to be transported outwards. Irregularities are not visible during draw back. The most regular oscillations

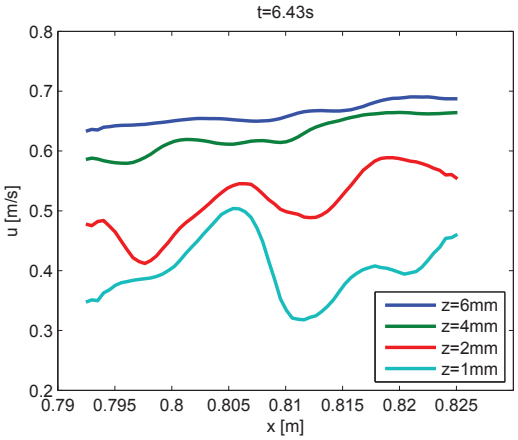

Figure 8: $a/d = 0.292$ Run 2. Horizontal velocity u for $z = 1, 2, 4$ and 6 mm at $t = 6.43$ s

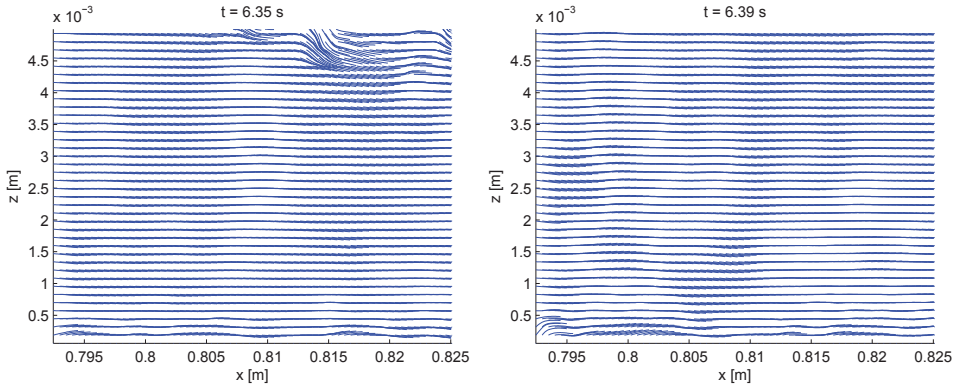

Figure 9: Streamlines extracted from $a/d = 0.292$ Run 2. Left image, $t = 6.35$ s, shows the early stage of run up with no sign of fluctuations, the irregularities in the upper right is caused by lack of seeding. Right image, $t = 6.39$ s shows the streamlines when fluctuations occur.

are detected in run 2 at $z = 1.9$ mm, as seen in figure 8 where the horizontal velocity component of the flow for $z = 1, 2, 4$ and 6 mm is shown.

Figure 13 shows wave numbers k_i, $i = 0, 1, 2, 3, 4$, together with corresponding amplitudes for $t = 6.37$, 6.41, 6.43 and 6.46 s. The amplitudes are normalized with the outer flow which is extracted from the PIV data. Inspection of amplitudes of the Fourier components reveals that k_1 is the dominant component of the perturbations. Temporal evolution of amplitudes for k_1-k_4 are shown in figure 14.

A phase of strong growth in A_1 is evident for t between $t = 6.38$ s and $t = 6.43$, say. Since we do not have any knowledge of "initial amplitudes" in the experiments the amplitudes themselves cannot be related to theory, but times and relative growth rates, $A^{-1}\mathrm{d}A/\mathrm{d}t$, can be compared. It is remarkable that for the given position the theory (figure 4, $\xi/d = 4$) predicts $t_c = 6.38$ s (critical time of instability when A starts to grow). However, while the growth in the experiment takes place in the range 6.38 s − 6.43 s, with a relative growth rate of 80 s^{-1} in the first part of this range, the growth in the theory lasts until $t = 6.9$ s, with a maximum relative growth rate of 15.7 s^{-1} at $t = 6.66$ s. Naturally, the estimates of the growth rates

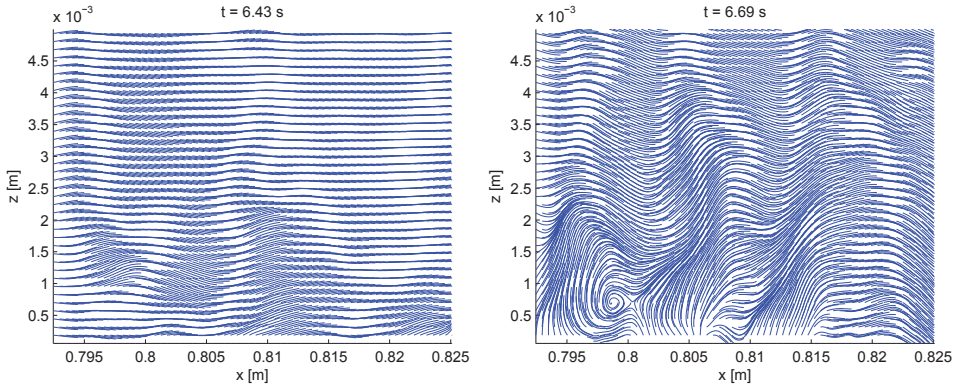

Figure 10: Streamlines extracted from $a/d = 0.292$ Run 2. Left image, $t = 6.43\,\mathrm{s}$, shows the streamlines when the Tollmien Schlichting waves appear in the flow. Right image, $t = 6.69\,\mathrm{s}$ shows the first generated vortex.

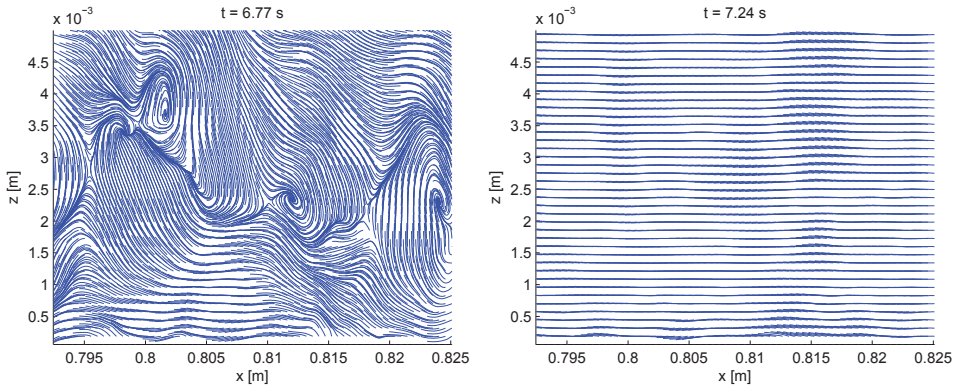

Figure 11: Streamlines extracted from $a/d = 0.292$ Run 2. Left image, $t = 6.77\,\mathrm{s}$, Vortices are transported outwards. Right image, $t = 7.24\,\mathrm{s}$ no sign of irregularities during draw back.

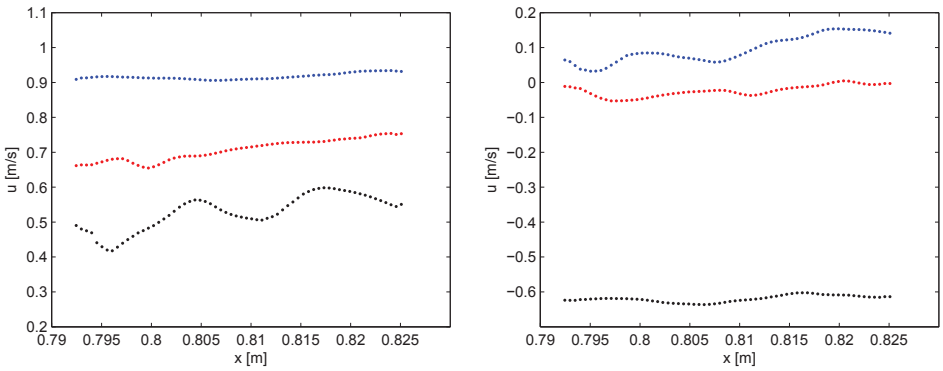

Figure 12: Velocities extracted from $a/d = 0.292$ Run 2. Left image: horizontal velocity component u, $t = 6.31\,\mathrm{s}$, $t = 6.39\,\mathrm{s}$ and $t = 6.43\,\mathrm{s}$ in blue, red and black. Right image: $t = 6.69\,\mathrm{s}$, $t = 6.77\,\mathrm{s}$ and $t = 7.24\,\mathrm{s}$ in blue, red and black.

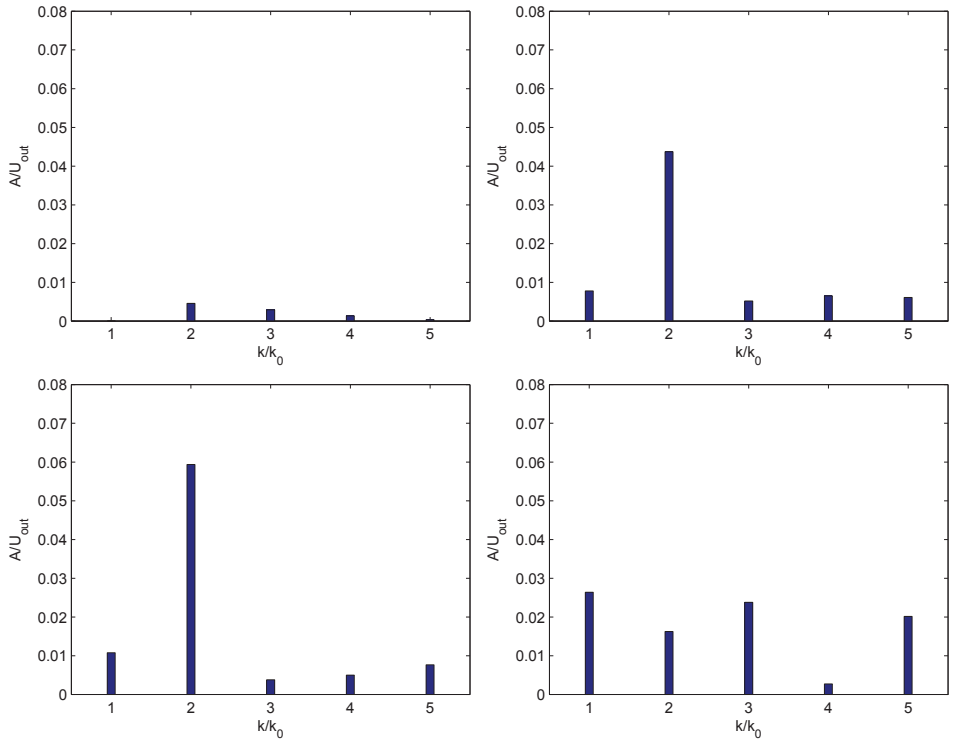

Figure 13: $a/d = 0.292$ Run 2. Wave numbers k_i, $i = 0 : 4$ with increasing k from left to right and corresponding amplitudes of the perturbations at $t = 6.37\,\mathrm{s}$ upper left, $t = 6.39\,\mathrm{s}$ upper right, $t = 6.43\,\mathrm{s}$ lower left, $t = 6.46\,\mathrm{s}$ lower right.

in the experiments are inaccurate. According to figure 10 in [10] there may also be significant differences in the base flows (boundary layer profiles before instability becomes noticeable) between experiments and theory. A difference must be assumed since the experimental and theoretical/inviscid runup height differs by 20% and FOV 2 is close to the shoreline (see figure 1). Still, the differences concerning growth rate are so substantial that we cannot rule out the possibility that the rapid experimental transition around $t = 6.40\,\mathrm{s}$ may be a secondary instability and that the first linear instability is lost in the measurements. According to [4] a secondary instability may be expected when the magnitude of undulations reaches, say, 1% of that of the base flow, while we measure the strong growth rates when the amplitudes are between 1% and 5% of the base flow.

Wavelengths, λ_1-λ_4, are shown in figure 15. Eddies that are formed in the later stage are shown in figure 16. The average distance measured between two consecutive eddies, shown in the figure, is $5 \times 10^{-3}\,\mathrm{m}$. Wavelengths, λ_1, are given in table 1 together with amplitudes of the perturbations, outer velocities and wavelengths, λ_{viz}, that are found by purely visual inspection. Wavelengths λ_1 vary between 1.01 cm and 1.57 cm, while the critical wave number extracted from the theoretical neutral curve corresponds to a wavelength of 1.05 cm. Hence, the length of first unstable mode in the analysis is clearly of the same order as the lengths observed in the experiment. Results from the temporal resolution are given in table 2, where periods T_1 are listed together with amplitudes of the perturbations, outer velocity and periods T_{viz} that are found by visual inspection.

Time	k_0 $[m^{-1}]$	λ_1 $[m]$	λ_{viz} $[m]$	u_{out} $[m/s]$	A_1/u_{out}
6.37 s	2.40×10^2	1.31×10^{-2}	-	7.94×10^{-1}	0.46×10^{-2}
6.38 s	2.12×10^2	1.49×10^{-2}	-	7.74×10^{-1}	0.28×10^{-2}
6.39 s	3.10×10^2	1.01×10^{-2}	-	7.48×10^{-1}	0.80×10^{-2}
6.40 s	2.13×10^2	1.47×10^{-2}	-	7.23×10^{-1}	1.94×10^{-2}
6.41 s	2.59×10^2	1.21×10^{-2}	1.2×10^{-2}	6.92×10^{-1}	4.37×10^{-2}
6.42 s	2.12×10^2	1.49×10^{-2}	1.2×10^{-2}	6.72×10^{-1}	4.25×10^{-2}
6.43 s	2.32×10^2	1.36×10^{-2}	1.4×10^{-2}	6.62×10^{-1}	5.94×10^{-2}
6.44 s	2.01×10^2	1.57×10^{-2}	1.4×10^{-2}	6.35×10^{-1}	4.63×10^{-2}
6.45 s	2.33×10^2	1.36×10^{-2}	-	6.19×10^{-1}	2.55×10^{-2}
6.46 s	2.05×10^2	1.54×10^{-2}	-	6.02×10^{-1}	1.63×10^{-2}

Table 1: $a/d = 0.292$ Run 2. Wave numbers k_0 and wavelengths λ_1 extracted from Fourier transformation, wavelengths λ_{viz} extracted manually from the figures, outer velocity u_{out} and amplitude A_1/u_{out}

x $[m]$	ω_0 $[rad/s]$	T_1 $[s]$	T_{viz} $[s]$	u_{out} $[m/s]$	A_1/u_{out}
0.800	1.30×10^2	2.42×10^{-2}	-	6.71×10^{-1}	5.1×10^{-2}
0.802	1.30×10^2	2.42×10^{-2}	-	6.62×10^{-1}	5.1×10^{-2}
0.803	1.30×10^2	2.42×10^{-2}	3.0×10^{-2}	6.56×10^{-1}	4.93×10^{-2}
0.805	1.06×10^2	2.95×10^{-2}	2.4×10^{-2}	6.74×10^{-1}	2.98×10^{-2}
0.807	1.42×10^2	2.22×10^{-2}	2.6×10^{-2}	6.79×10^{-1}	3.77×10^{-2}
0.815	1.30×10^2	2.42×10^{-2}	2.6×10^{-2}	6.95×10^{-1}	3.52×10^{-2}
0.816	1.23×10^2	2.55×10^{-2}	2.8×10^{-2}	6.99×10^{-1}	3.40×10^{-2}

Table 2: $a/d = 0.292$ Run 2. Angular frequencies ω_0 and periods T_1 extracted from Fourier transformation, periods, T_{viz} extracted manually from the figures, outer velocity u_{out} and amplitude A_1/u_{out}

5.3.2 Brief overview of $a/d = 0.292$, Run 1 and Run 3

Results from the spatial resolution is extracted from the data for Run 1 and Run 3 and given in tables 3 and 4. Amplitudes of the perturbations are markedly smaller in Run 1 compared to Run 2, while for Run 3 the amplitudes are comparable to those of Run 2. One should also notice that the time range for the oscillations are shorter in Run 1 and Run 3 compared to Run 2.

Time	k_0 $[m^{-1}]$	λ_1 $[m]$	λ_{viz} $[m]$	u_{out} $[m/s]$	A_1/u_{out}
6.41 s	2.77×10^2	1.14×10^{-2}	-	6.93×10^{-1}	1.08×10^{-2}
6.42 s	3.53×10^2	0.89×10^{-2}	1.5×10^{-2}	6.90×10^{-1}	0.59×10^{-2}
6.43 s	2.34×10^2	1.34×10^{-2}	-	6.62×10^{-1}	2.76×10^{-2}
6.44 s	2.69×10^2	1.17×10^{-2}	1.2×10^{-2}	6.59×10^{-1}	2.24×10^{-2}
6.45 s	2.29×10^2	1.38×10^{-2}	1.2×10^{-2}	6.38×10^{-1}	2.31×10^{-2}
6.46 s	2.24×10^2	1.41×10^{-2}	1.2×10^{-2}	6.17×10^{-1}	1.17×10^{-2}

Table 3: $a/d = 0.292$ Run 1. Wave numbers k_0 and wavelengths λ_1 extracted from Fourier transformation, wavelengths λ_{viz} extracted manually from the figures, outer velocity u_{out} and amplitude A_1/u_{out}

5.3.3 Irregularities of $a/d = 388$ and $a/d = 0.481$

The largest waves with $a/d \sim 0.4$ and 0.5 were unstable during runup in the upper FOV. Attempts to find structures akin to Tollmien Schlichting waves have been made. Unfortunately, they failed due to poor seeding in the start of the runup tongue causing loss of velocity vectors in the early stage of the runup.

Fluctuations, but without good repeatability, were also detected for $a/d \sim 0.5$ in the FOV located close to equilibrium in the middle of the tank. The flow turned unstable in one out of four experiments. Video recordings revealed that the beach experienced a depression (up to 1 mm) during runup due to the load of the swash flow. However, at present it is not clear how this may cause pronounced transverse

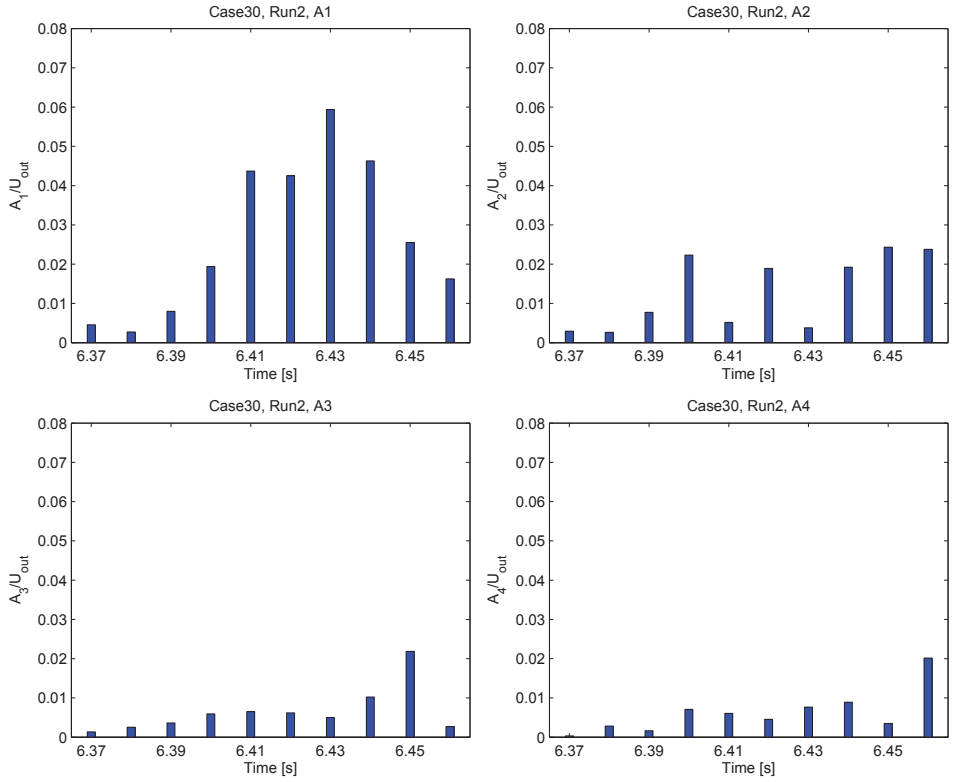

Figure 14: $a/d \sim 0.3$ Run 2. Growth in amplitude for k_1 (upper left), k_2 (upper right), k_3 (lower left), k_4 (lower right), $t = 6.37 - 6.46\,\mathrm{s}$.

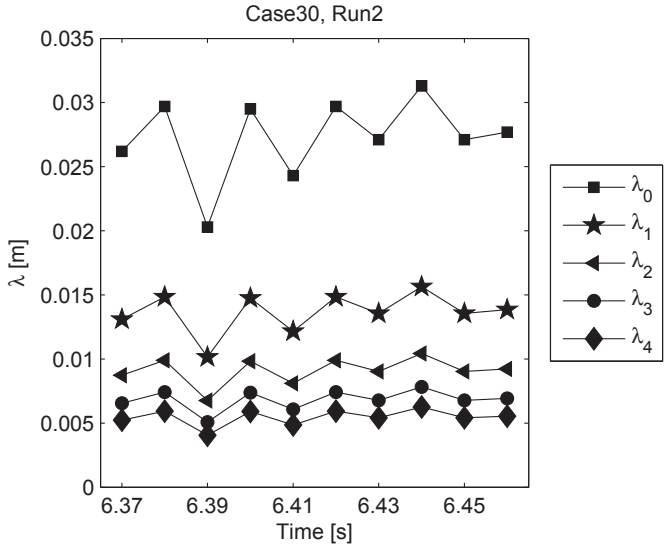

Figure 15: $a/d \sim 0.3$ Run 2. Wavelengths

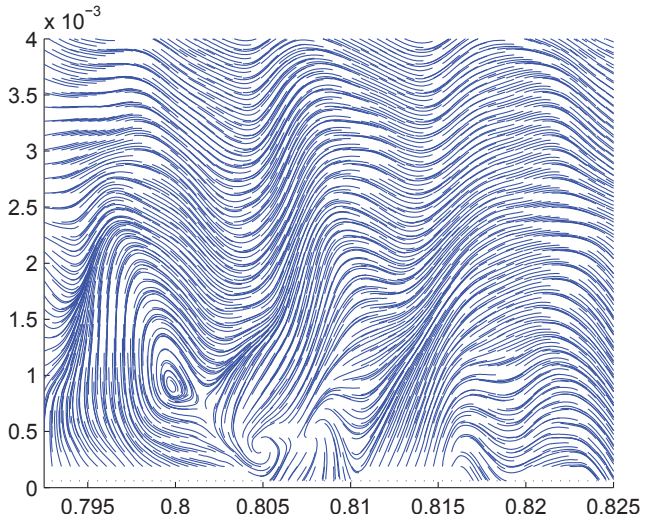

Figure 16: $a/d = 0.292$ Run 2. Streamlines with eddies at $t = 6.70\,\mathrm{s}$

Time	k_0 $[m^{-1}]$	λ_1 $[m]$	λ_{viz} $[m]$	u_{out} $[m/s]$	A_1/u_{out}
6.37 s	2.54×10^2	1.24×10^{-2}	1.2×10^{-2}	7.76×10^{-1}	2.90×10^{-2}
6.38 s	2.44×10^2	1.29×10^{-2}	1.5×10^{-2}	7.60×10^{-1}	4.69×10^{-2}
6.39 s	2.30×10^2	1.37×10^{-2}	1.2×10^{-2}	7.31×10^{-1}	4.41×10^{-2}
6.40 s	2.13×10^2	1.47×10^{-2}	1.2×10^{-2}	7.13×10^{-1}	4.30×10^{-2}
6.41 s	2.35×10^2	1.34×10^{-2}	1.3×10^{-2}	7.06×10^{-1}	4.30×10^{-2}
6.42 s	2.54×10^2	1.24×10^{-2}	-	6.92×10^{-1}	3.23×10^{-2}

Table 4: $a/d = 0.292$ Run 3. Wave numbers k_0 and wavelengths λ_1 extracted from Fourier transformation, wavelengths λ_{viz} extracted manually from the figures, outer velocity u_{out} and amplitude A_1/u_{out}

variation in the evolution of the boundary layers. In any case, the largest wave may be close to the transitional regime also in the start of the runup.

6 Remarks

[13] suggested that local instability is always to be expected in the decelerated parts of bottom boundary layers in transient or oscillatory flow. This is supported by the present theoretical investigation of instability in swash zone boundary layers. A crucial quantity from linear stability analysis for a flow of this type is the total amplification during the span of the unstable period. For a solitary wave in constant depth of 0.2 m this amplification is modest. It then decreases during shoaling while it is strongly increased, well beyond that in constant depth, in the swash zone, where we have large velocities and decelerations. Hence, in a runup experiment transition in the boundary layer are most likely to appear onshore.

It is to be expected that small scale features, such as undulatory behaviour in a boundary layer is, difficult to detect experimentally. From the experiments in [11] we could identify only one FOV in a single experiment with velocity measurement of sufficient quality for revelation of distinct flow patterns resembling Tollmien Schlichting waves. It is encouraging that for this experiment we found very good agreement for the time of appearance of instabilities and that the dominant length of the experimental undulations are close to the length of the critical Tollmien Schlichting waves. However, the realtive

growth rate of the observed waves cannot be reconciled with theoretical growth rates. Other repetitions of the same experiment suffered from poorer seeding leading to a lower quality in the measurements. Still, this is unlikely as a single explanation for the lack of reproducibility. Even though, irregular flow was observed in these repetitions as well, there were substantial differences in both amplitudes and the duration of the oscillations. According to [13] poor repeatability may be expected in such a case due to the nature of the instability and the absence of a controlled perturbation of the flow. To produce firm experimental evidence of the boundary layer instabilities in swash flow on this scale one would probably have to make a vast number of repetitions with well controlled sources of noise of different magnitudes. Moreover, according to, for instance, [4], a secondary instability may be expected when the magnitude of undulations reaches, say, 1% of that of the base flow. In our good experiment they reach 3-5% before vortex formation is observed and it is possible that the observed growth may be associated with the secondary rather than primary, linear instability. Methods like the PIV often have a noise level of order 1%, which makes direct observation of the first linear stage of the instability difficult in the first place.

References

[1] Paolo Blondeaux, Jan Pralits, and Giovanna Vittori. Transition to turbulence at the bottom of a solitary wave. *Journal of Fluid Mechanics*, 709:396–407, 2012.

[2] Paolo Blondeaux and Giovanna Vittori. Rans modelling of the turbulent boundary layer under a solitary wave. *Coastal Engineering*, 60:1–10, 2012.

[3] P. G. Drazin and W. H. Reid. *Hydrodynamic Stability*. Cambridge University Press, 1981.

[4] Thorwald Herbert. Secondary instability of boundary layers. *Annual Review of Fluid Mechanics*, 20:487–526, 1988.

[5] A. Jensen, G. Pedersen, and D. J. Wood. An experimental study of wave run-up at a steep beach. *J. Fluid. Mech.*, 486:161–188, 2003.

[6] R. Jordinson. The flat plate boundary layer. part 1. numerical integration of the Orr-Sommerfeld equation. *Journal of Fluid Mechanics*, 43:801–811, 1970.

[7] G. Sælevik. xxx, 2008. PhD thesis, University of Oslo.

[8] G. Sælevik, A. Jensen, and G. Pedersen. Runup of solitary waves on a straight and a composite beach. *Coastal Engineering*, 77, 2013.

[9] Celalettin E. Ozdemir, Tian-Jian Hsu, and S. Balachandar. Direct numerical simulations of instability and boundary layer turbulence under a solitay wave. *Journal of Fluid Mechanics*, 731:545–578, 2013.

[10] G. K. Pedersen, E. Lindstrøm, A. F. Bertelsen, A. Jensen, D. Laskovski, and G. Sælevik. Runup and boundary layers on sloping beaches. *Physics of Fluids*, 25:pp. 23, 2013. doi: 10.1063/1.4773327.

[11] Geir K. Pedersen, Erika Lindstrøm, Arnold F. Bertelsen, Atle Jensen, Daniela Laskovski, and G. Sælevik. Runup and boundary layers on sloping beaches. *Physics of Fluids*, 25:pp. 23, 2013.

[12] B. Mutlu Sumer, Palle M. Jensen, Lone B. Sørensen, Jørgen Fredsøe, Philip L.-F. Liu, and Stefan Carstensen. Coherent structures in wave boundary layers. part 2. solitary motion. *Journal of Fluid Mechanics*, 646:207–231, 2010.

[13] Joris C. G. Verschaeve and Geir K. Pedersen. Linear stability of boundary layers under solitary waves. *Journal of Fluid Mechanics*, under review.

[14] Giovanna Vittori and Paolo Blondeaux. Turbulent boundary layer under a solitary wave. *Journal of Fluid Mechanics*, 615:433–443, 2008.

[15] Giovanna Vittori and Paolo Blondeaux. Characteristics of the boundary layer at the bottom of a solitary wave. *Coastal Engineering*, 58:206–213, 2011.

Part III

Experiments on slide generated waves in a 1:500 scale model

Appendix A

Filter applied for the ultrasonic wave gauges

In 2012 a new set of ultra sonic gauges (Banner U-Gage S18U) were bought at the hydrodynamic laboratory, University of Oslo. These gauges displayed more noise in the signals than the older ones, even though the the only difference between the newer gauges and the old ones were the production year. A great amount of work were performed in investigating the reason for the reduced quality. Both technical staff at the producer and the laboratory engineer at the University of Oslo looked in to this. The reason for decreased quality of the signal were not found and the data was still within the specification (Banner-Engineering, 2013), even though the quality was dramatically reduced.

Therefor, development of a proper filter for the detected noise started. The first step was to determine where the actual signal was hidden in the noise. The noise was regular, and the true value was always located at minimum values of the collected data while the noise was located approximately 0.6 mm or 1.2 mm above. Low pass filters were not suitable for this particular noise pattern, with the result of a a filtered signal located in between the actual data and the noise. Different approaches in developing a suitable filter were done and the final version were written in MatLab by Dr. Odin Gramstad. This filter removes sharp peaks exceeding the smallest of two neighboring points where a threshold value determine whether the detected peak is considered to be noise. The removed values are then replaced by interpolating the nearest points with cubic interpolation. In figure 17 the raw data from an experiment containing a large amount of noise and the result from the applied filter is demonstrated.

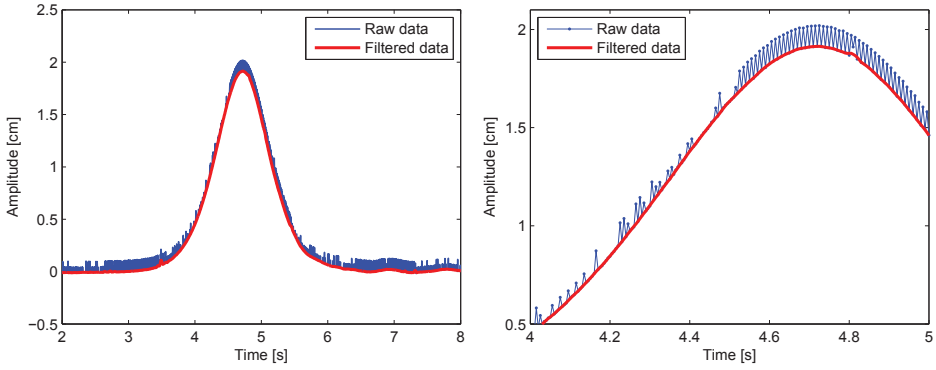

Figure 17: Illustration of the detected noise and effect of the applied filter. Left: Collected and processed data for a solitary wave. Right: Zoom of the crest, spikes are visible and the filter detect the correct signal.